Development of a Drift Chamber for Drift Velocity Monitoring in the CMS Barrel Muon System

von

Georg Altenhöfer

Diplomarbeit in Physik

vorgelegt der

Fakultät für Mathematik, Informatik und Naturwissenschaften
der Rheinisch-Westfälischen Technischen Hochschule Aachen

im Mai 2006

angefertigt im

III. Physikalischen Institut A
Prof. Dr. Thomas Hebbeker

Abstract

In this thesis, the development and construction of a gas quality test chamber for the CMS barrel muon system is described. This device is a small drift chamber, monitoring the key parameter of the gas: the electron drift velocity v_d. The aim is to detect changes in the drift velocity with a resolution of 0.1% to guarantee a stable time to position relation in the muon system.

Systematic computer simulations have been performed to optimise the drift field in the chamber. For the construction of a prototype, the main task - apart from reaching the needed precision - is to achieve the necessary field strength to be able to generate drift fields of more than 2 kV/cm as they are present in the CMS muon barrel drift tubes. First measurements with the prototype chamber are presented.

The field simulations predict a field inhomogeneity of 0.1% in the sensitive area of the chamber. With a maximum cathode voltage of 15 kV, a drift field of 2.27 kV/cm can be reached. The statistical error (which is the relevant error for the detection of changes) of a first long term measurement ($\sim$ 10 h, 800 000 events) of v_d is below 0.01% for a mean drift velocity of $v_d = 55.6\,\mu$m/ns at $E = 1850$ V/cm. These values agree very well with the expectations.

Within a measuring time of a few minutes the statistical error is already below 0.1%.

Zusammenfassung

Gegenstand dieser Diplomarbeit ist die Entwicklung und Konstruktion einer Gasqualitäts-Testkammer für das CMS Barrel Myon System. Es handelt sich dabei um eine kleine Driftkammer, die den Schlüsselparameter des Gases für die Rekonstruktion der Teilchenspuren überwacht: die Driftgeschwindigkeit v_d der Elektronen. Ziel ist es, Schwankungen der Driftgeschwindigkeit möglichst genau zu erfassen, um eine stabile Orts-Driftzeit-Beziehung im Myon-System zu garantieren.

Zur Optimierung des Driftfeldes in der Kammer werden systematische Computersimulationen durchgeführt. Bei der Konstruktion ist neben dem Erreichen der nötigen Präzision die Hochspannungsfestigkeit ein wichtiger Punkt, da in der Testkammer ein mit dem Myon-System vergleichbares Driftfeld von über 2 kV/cm erreicht werden soll. Schließlich werden noch die ersten Testergebnisse mit einem Prototyp der Kammer vorgestellt.

Durch die Simulationen des elektrischen Feldes konnte eine Homogenität von $\Delta E/E = 0,1\%$ im sensitiven Bereich der Kammer erreicht werden. Bei einer maximalen Kathodenspannung von 15 kV wird ein Driftfeld von 2,27 kV/cm erzeugt. Der für die Erfassung von Veränderungen wichtige statistische Fehler lag bei einer ersten Langzeitmessung (ca. 10 Stunden und 800 000 Ereignisse) bei 0,01%. Die gemessene mittlere Driftgeschwindigkeit von $v_d = 55,6\,\mu$m/ns bei 1850 V/cm entspricht vollkommen den Erwartungen.

Die gewünschte Auflösung von $0,1\%$ kann schon bei einer Messzeit von einigen Minuten erreicht werden.

Contents

Chapter 1

Introduction

For thousands of years mankind has been interested in the question about the constitution of matter. 2 600 years ago, Greek philosophers were searching for the *primary matter*, the substance everything consists of. *Atoms*[1], first introduced by Demokrit (500 BC), were meant to be very small massive particles differing in size and shape. Experimental evidence for the existence of atoms was first found in the 19th century, when John Dalton discovered that chemical reactions of different elements take place only with defined mass ratios. He concluded, that the atoms are able to form *molecules*, but he still thought of atoms as indivisible particles. At the end of the 19th century, J.J. Thomson succeeded in separating negatively charged particles - *electrons* - from atoms, showing that atoms could be split in smaller constituents. Different models tried to describe how these different charges are linked to each other. In 1911, Ernest Rutherford proved, that atoms consist of a small positively charged nucleus and a negatively charged shell. The positive charge was attributed to the particles in the nucleus: the *protons*[2]. When it was found that the weight of most nuclei is greater than the sum of its protons a third building block for the atom was necessary: the electrically neutral *neutron*.

Today, this is still our picture of atoms, although the understanding of the way how electrons are arranged in the shell and how protons and neutrons are grouped in the nucleus has highly improved. But this is far from the end of the story: protons and neutrons are also not point-like but consist of smaller particles - the *quarks*. With our present knowledge we consider them as elementary particles i.e. point-like particles without a substructure.

The ambition of particle physics is to learn more about the elementary particles, their interactions and their probable composition of even smaller particles which have not been discovered yet. One way to do this are scattering experiments at high energies using particle colliders. For the detection of particles, large detectors like the CMS experiment[3](see chapter 3) are built. CMS is one of the experiments situated at the worlds largest particle physics laboratory CERN[4] near Geneva.

[1] greek: atomos = indivisible
[2] greek: proton = first
[3] Compact Muon Solenoid
[4] The European Organisation for Nuclear Research (foundation name: Conseil Européen pour la Recherche Nucleaire)

This thesis describes the development and construction of a device for monitoring the gas quality in one of the CMS (see section 4.3.1) subdetectors: the barrel muon detector. The concept of the monitoring device - a small drift chamber (see section 4.2) - originates from the L3 detector[5] and has been adapted to match the CMS needs. Systematic computer simulations have been performed (see chapter 6) to optimise the properties of the chamber. The construction of the chamber, built in cooperation with the mechanical and electronical workshops of the III. Physikalische Institut, is described in chapter 7. Results from the first measurements with the chamber are presented in chapter 8.

[5]Experiment at the Large Electron Positron Collider (LEP)

Chapter 2

The Standard Model of Particle Physics

2.1 The Components of Matter - The Fermions

Numerous experiments probing structures smaller than 10^{-18} m have demonstrated, that matter consists of 12 different elementary particles. They are called *fermions*[1] (Tab. 2.1) and can be divided into 6 *leptons*[2] and 6 *quarks* (plus their antiparticles). While the primer ones can be detected as free particles the quarks are confined within *hadrons*. Both leptons and hadrons can be grouped in three *families* or *generations* (Tab. 2.1). However, the surrounding ordinary matter consists only of particles from the first family: electrons, up- and down-quarks. While electrons exist as isolated particles, quarks form either a proton (up-up-down) or a neutron (up-down-down). Within an atom (Fig. 2.1), protons and neutrons together form the nucleus while the electrons represent the outer shell.

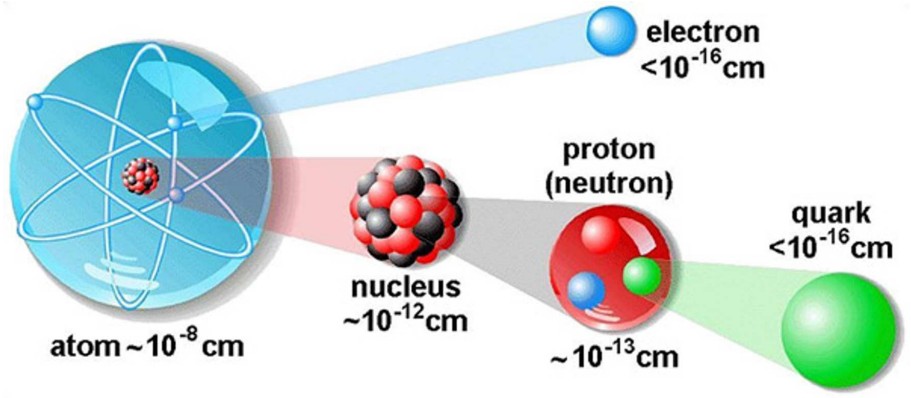

Figure 2.1: *The structure of an atom at different scales* [3].

Electrons have a negative electric charge of $-e = -1.6022 \cdot 10^{-19}$ C. This is the smallest possible charge for an isolated particle, called the elementary charge. The quarks have charges of $2/3\,e$ and $-1/3\,e$ (see also Tab. 2.1), but they do not exist isolated. Therefore the elementary charge is also the smallest observable charge fraction for hadrons which are

[1] Particles with half-integer spin, named after Enrico Fermi.
[2] from Greek *leptós*: small, light

Family	Flavour		Charges Electric	Colour	Mass [MeV]
Leptons					
I	Electron	e^-	$-e$	-	0.511
	Neutrino	ν_e	0	-	$< 3 \cdot 10^{-6}$
II	Muon	μ^-	$-e$	-	106
	Neutrino	ν_μ	0	-	< 0.19
III	Tauon	τ^-	$-e$	-	1777
	Neutrino	ν_τ	0	-	< 18.2
Quarks					
I	up	u	$2/3\,e$	rgb	≈ 5
	down	d	$-1/3\,e$	rgb	≈ 10
II	charm	c	$2/3\,e$	rgb	≈ 1300
	strange	s	$-1/3\,e$	rgb	≈ 200
III	top	t	$2/3\,e$	rgb	≈ 178000
	bottom	b	$-1/3\,e$	rgb	≈ 4300

Table 2.1: *List of the fundamental fermions [1, 2], their electric and colour charge as well as their mass. For the neutrinos the masses are upper thresholds from direct mass measurements. Observations of neutrino oscillations lead to the conclusion that at least two neutrino generations have non-zero masses.*

made of quarks. Protons for example have a charge of $+e$, while neutrons are electrically neutral. Every atom has the same number of electrons and protons, so that the atom in total is electrically neutral.

In addition to the electric charge, quarks have a *colour charge* (called "red", "blue" and "green"). To build a stable hadron, the sum of the colours of the involved quarks must be colourless ($red + blue + green = white$ or $red + antired = white$). A hadron is called *baryon* if it consists of three quarks while it is called a *meson* if it is built out of a quark and an antiquark.

The particles of the second and third family are copies of the particles of the first, differing only in their mass, their lifetime and their *lepton quantum number* which defines the particles family. A muon for example is just a heavier electron with a limited life time, while all other attributes are the same.

The most mysterious particles of the Standard Model are the neutrinos. Because they are electrically neutral, they participate only in *weak* and *gravitational interactions* (see below) and thus have a very small cross-section. This makes neutrinos nearly undetectable. For example at collider detectors, neutrinos can only be identified as missing energy. Despite the huge neutrino flux even huge experiments specially built for neutrino detection (e.g. Super-Kamiokande [4] with 50 000 t of water) can record only a few neutrino events per day.

With every particle *quantum numbers* are associated. Examples for additive quantum numbers are the lepton quantum number (+1 for the leptons, −1 for antileptons, 0 for quarks), the flavour quantum number (electron number, μ-number, τ-number) or the

charge. The sum of the quantum numbers must be conserved, i.e. they must be the same before and after an interaction.

To each particle of the Standard Model, there is an antiparticle. Particles and their corresponding antiparticles have the same mass and spin, but opposite (additive) quantum numbers and charges. The electron e^- has a charge of $-e$ and the lepton quantum number $+1$, while its antiparticle, the positron e^+, carries the charge $+e$ and has the lepton quantum number -1. Usually, antiparticles are denoted by a bar (electron neutrino ν_e and anti electron neutrino $\bar{\nu}_e$).

The following example shows the quantum number conservation for the decay of a muon into an electron e, an anti electron neutrino $\bar{\nu}_e$ and a muon neutrino ν_μ:

	μ^-	$\rightarrow$	e^-	$+$	$\bar{\nu}_e$	$+$	ν_μ
electron number:	0	=	$+1$		-1		0
muon number:	1	=	0		0		1

Another particle attribute is the spin - the intrinsic angular momentum. It is expressed in units of $\hbar$: fermions have spin 1/2 while bosons have integer spin.

2.2 The Four Fundamental Interactions

In classical physics, forces and interactions are mediated by *fields*, such as the electromagnetic field. On the elementary particle scale, the classical theory of electrodynamics fails to describe numerous phenomena so it was necessary to develop a new theory: the *quantum field theory of electrodynamics*. The Standard Model comprises such quantum field theories for three of the four known interactions. In field theories interactions are mediated by *gauge bosons* (Fig. 2.2) which are the quanta of the field. Whether a particle participates in a certain interaction depends on the question if the corresponding boson couples to this particle.

The boson of the **electromagnetic interaction** is the photon. Photons do not have a rest mass, therefore they travel with the fastest possible speed: the speed of light. The electromagnetic interaction has an infinite range: With increasing distance, the force decreases but never disappears. The photon couples to every electric charged particle but as it is electrically neutral, it cannot change the charge of a particle or couple to itself.

The **weak interaction** is mediated by the $W^\pm$ and Z^0-bosons. Carrying a so called *weak charge*, they can interact with each other. Furthermore, the electrically charged W-bosons couple also to photons. Due to the large rest masses of the $W^\pm$ and Z^0-bosons, the weak interaction has only a short range. The radioactive β-decay, for example, is governed by the weak interaction. Within the Standard Model, the electromagnetic and the weak interaction are unified to the *electroweak interaction*.

The **strong interaction** is an interaction that effects only quarks and *gluons*. The latter are the bosons of the strong interaction, which themselves carry a strong charge. Although one would presume 9 different gluons for 3 colours and 3 anticolours only 8 of them are realized in nature. This can be described mathematically with the underlying symmetry $SU(3)$ of the strong interaction. Each gluon carries a colour and an anticolour, so that

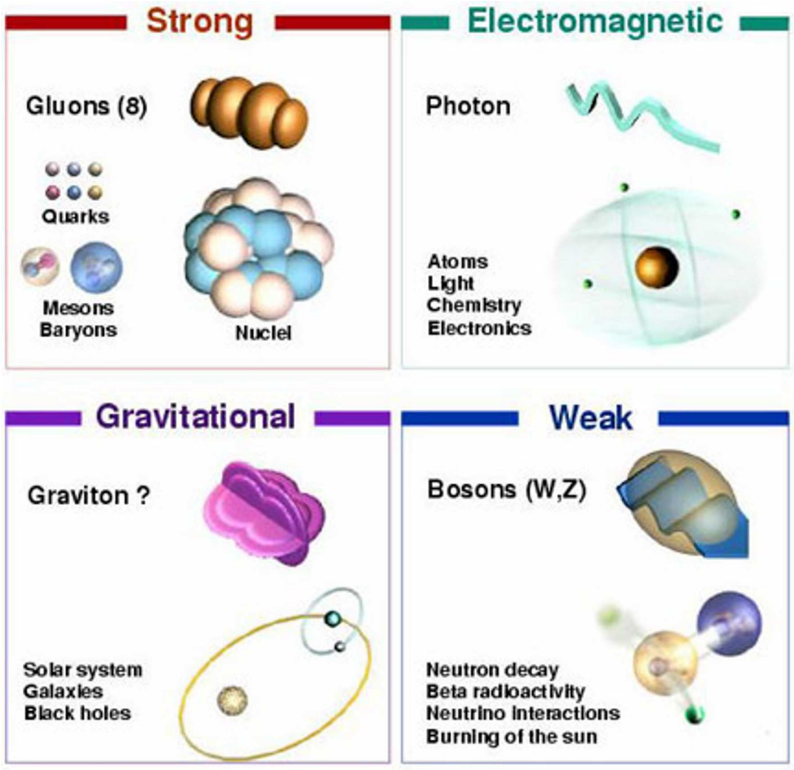

Figure 2.2: *The four interactions and their mediating particles are shown together with their typical occurrence* [3].

the gluons can change the quarks' colour charge. The strong interaction for example holds together the three quarks inside a nucleon.

The **gravitational interaction** is the only interaction that is not described by the Standard Model of Particle Physics and the dedicated boson , the graviton, has not been discovered yet. The gravitation has infinite range, but it is extremely weak compared to the other interactions.

2.3 Description of the Interactions by Gauge Theories

As mentioned above, three of the four fundamental interactions can be described by the exchange of field quanta: the bosons. *Gauge theories* are a mathematical way to receive those fields from symmetries.

A basic principle for such a theory is Noether's theorem: if the Langrange function $L(q_\alpha(t), \dot{q}_\alpha(t), t)$ of a physical system with the general coordinates q_α and momenta $\dot{q}_\alpha$ is invariant under a transformation $q_\alpha(t) \rightarrow q_\alpha(t,s) = q_\alpha(t) + \eta_\alpha(t)s + O(s^2)$, then it is possible to derive a conservation law.

The concept of the gauge theories shall be explained here by the example of the electromagnetic interaction. This concept was first developed by H. Weyl [5].

The Dirac equation for a spin 1/2 particle in an electromagnetic field A_μ is:

$$(i\gamma^\mu(\partial_\mu + iqA_\mu) - m)\Psi = 0 \tag{2.1}$$

$$\gamma^\mu = (\beta, \beta\alpha^i) \qquad i = 1, 2, 3. \tag{2.2}$$

In the chiral description, the 4×4-matrices are written as:

$$\alpha = \begin{pmatrix} -\sigma_i & 0 \\ 0 & \sigma_i \end{pmatrix}, \qquad \beta = \begin{pmatrix} 0 & 0 & 0 & 1 \\ 0 & 0 & 1 & 0 \\ 0 & 1 & 0 & 0 \\ 1 & 0 & 0 & 0 \end{pmatrix}, \qquad \sigma_i : \text{Pauli Matrices.} \tag{2.3}$$

Equation 2.1 is invariant under a transformation $A^\mu \rightarrow A'^\mu - \partial^\mu\chi(\vec{r}))$, which means that one can find a solution for this equation if A^μ is transformed in the given way. Ψ' can be generated by a local phase transformation:

$$\Psi(\vec{r}) \rightarrow \Psi'(\vec{r}) = e^{i \cdot (q/\hbar) \cdot \chi(\vec{r})} \tag{2.4}$$

As this transformation depends on the place $\vec{r}$, it is denoted as *local phase transformation*. Executing the local phase transformation on the wave function $\Psi(\vec{r})$ of a free particle, one finds that the transformed function $\Psi'(\vec{r})$ is no solution for the Dirac equation of a free particle.

$$(i\gamma^\mu\partial_\mu - m)\Psi'(\vec{r}) = -q\gamma^\mu\partial_\mu\chi(\vec{r})\Psi'(\vec{r}) \tag{2.5}$$

The invariance of the Dirac equation under a local phase transformation can be recovered by the implementation of a vector field $A_\mu(\vec{r})$ that transforms to $A'\mu(\vec{r}) = A_\mu(\vec{r}) - \partial_\mu\chi(\vec{r})$. With the covariant derivation $D_\mu = \partial_\mu + iqA_\mu$, the Dirac equation changes to:

$$(i\gamma^\mu D_\mu - m)\Psi(\vec{r}) = 0 \tag{2.6}$$

Thus, the electromagnetic field A_μ can be derived from the postulation of the invariance of the Langrangian against a local phase transformation. The quanta of the electromagnetic field are the photons and the underlying symmetry is the so called $U(1)_{em}$ group.

Similar to this calculation, the other gauge bosons can be derived from dedicated symmetries. In case of the electroweak interaction this is the $SU(2)_L \times U(1)_Y$ group. The $SU(2)_L$ group that is associated with the weak interaction can be described by the three Pauli matrices, according to the three gauge bosons $W^\pm$ and Z^0. The strong interaction corresponding to the $SU(3)_C$ group can be generated by the eight Gell-Mann matrices, according to the eight gluons. The Standard Model in complete can be described by the gauge symmetry group $\mathrm{SU}(3)_C \times SU(2)_L \times U(1)_Y$.

2.4 The Higgs Mechanism

The particle masses vary over at least 11 orders of magnitude from the electron neutrino ($m < 2\,\mathrm{eV}$) to the heaviest known particle, the top quark ($m \approx 178\,\mathrm{GeV}$). The Standard Model describes neither this large variations nor the origin of the masses.

A popular solution, proposed by P. Higgs, explains the masses by an additional field that couples to all particles: the *Higgs field*. The coupling is proportional to the mass of the particle. The corresponding vector boson of the Higgs Field is called the *Higgs boson*.

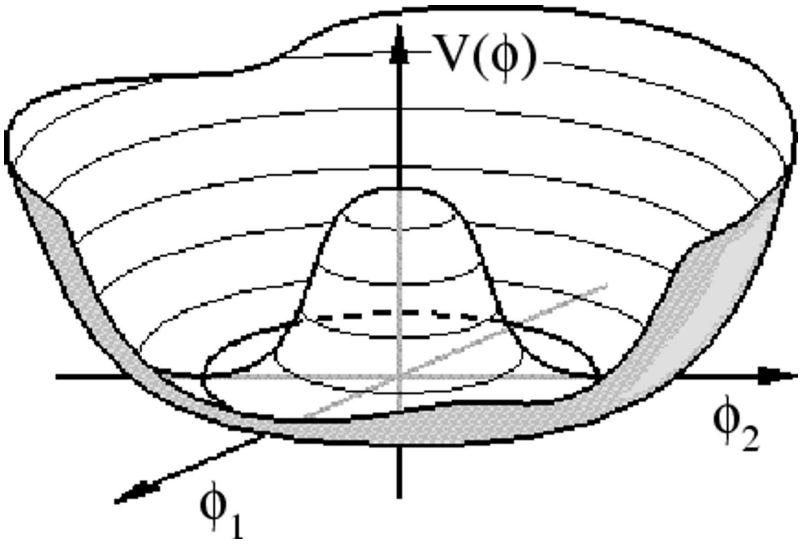

Figure 2.3: *The Higgs potential.*

Any invariance of the Lagrangian to a local gauge symmetry leads, as described above, to new gauge fields. However, a mass term inside the Lagrangian violates the gauge invariance, so that the interactions must be mediated by bosons with zero mass. For the weak interaction, this cannot be the case, as the corresponding bosons, $W^{\pm}$ and Z^0, do have a rest mass. A solution is presented by the Higgs mechanism: the particles themselves have zero mass and receive their mass by a spontaneous symmetry breaking of a gauge symmetry.

The spontaneous symmetry breaking can be realised by the introduction of scalar fields in the Lagrange density:

$$\mathcal{L} = (\partial^{\nu}\phi)(\partial_{\nu}\phi) - \mathcal{V}(\phi) \tag{2.7}$$

with the Higgs potential ($\lambda, \mu \neq 0$):

$$V(\phi) = -\mu^2|\phi|^2 + \lambda^2|\phi|^4 \qquad \text{and} \tag{2.8}$$

$$\phi(x) = \frac{1}{\sqrt{2}}(\phi_1(x) + i\phi_2(x)). \tag{2.9}$$

The minimum of this potential is not in the origin, but forms a circle around it (Fig. 2.3), so that there is an infinite number of ground states with identical energy

$$\phi_0 = \frac{1}{\sqrt{2}}\frac{\mu}{\lambda}e^{i\theta}. \tag{2.10}$$

The phase ϕ can be chosen freely. This case, where the potential is symmetric but not the vacuum expectation value, is called spontaneous symmetry breaking. Now, a state

$\phi(x)$ near the ground state shall be discussed. The phase θ can be set to zero. Therefore, the Higgs field is tailored around the vacuum expectation value:

$$\phi(x) = \frac{1}{\sqrt{(2)}}(\frac{\mu}{\lambda} + \zeta(x) + i\eta(x)) \tag{2.11}$$

Replacing this Higgs field in the previous formulas and neglecting terms of 3rd and 4th order in η and ζ, the following potential and Lagrangian are obtained:

$$V(\phi) = \mu^2(-\phi\phi^* + \frac{\lambda^2}{\mu^2}(\phi\phi^*)^2) \tag{2.12}$$

$$= \mu^2\eta^2 - \frac{1}{4}\frac{\mu^4}{\lambda^2} \tag{2.13}$$

$$\mathcal{L} = (\frac{1}{2}(\partial^\nu\eta)(\partial_\nu\eta) - \mu^2\eta^2)) + \frac{1}{2}((\partial^\nu\zeta)(\partial_\nu\zeta)) + ... \tag{2.14}$$

This Lagrange density describes two particles: a massive particle with $m_\eta = \sqrt{2}\cdot\mu$ and a particle with zero mass. The former particle is the Higgs boson, while the latter, the Goldstone boson, is not observed in nature (It is absorbed by the fields of the electroweak interaction via a gauge transformation).

2.5 Open Questions

Although the Standard Model of Particle Physics has been tested and proven by many experiments, there are still numerous open questions. Some of them shall be brought up here:

- Originally, the Standard Model does not explain particle masses. Up to now, there is no experimental evidence for the existence of the Higgs boson and the Higgs mechanism that is the favoured way to explain the origin of masses (see section 2.4). The experiments of the former particle collider LEP[3] exclude the existence of a neutral Higgs boson with a mass up to 114.4 GeV [6], while fits to electroweak precision measurements exclude higgs masses beyond 250 GeV.
- The Standard Model is not satisfying, because there are too many free parameters - like coupling constants which describe for example the particle masses - that can only be determined by experiments.
- There is still no theory to describe gravitation at quantum level.

These are only some of the reasons, why it is widely assumed, that the Standard Model needs to be extended or even replaced by a more general theory. Physicists keep developing extensions and theories but no evidence has been found yet for one of them. One of the experiments trying to explore a new energy scale in order to investigate new theories and to probe the Standard Model, is the currently built Large Hadron Collider at the particle physics laboratory CERN (see 3.1).

[3] Large Electron Positron Collider

Chapter 3

The CMS Experiment at the LHC

As described in chapter 2, there are many things to explore within and beyond the Standard Model. Tools to do this are particle colliders where particles are accelerated to nearly the speed of light and then brought to collision. In these collisions, a fraction of the energy (kinetic energy + mass) of the colliding particles is released, producing energy densities like they existed shortly after the big bang. According to Einstein's formula $E = mc^2$, this energy can be transformed into new particles. The more energy is available, the more mass the produced particles can have.

3.1 The Large Hadron Collider (LHC)

3.1.1 The Machine

The Large Hadron Collider (LHC, Fig. 3.1) is the future proton-proton storage ring at the European Organization for Nuclear Research CERN in Geneva. It is one of the most ambitious projects in high energy physics. The LHC is built in the tunnel of the former e^+/e^--storage ring LEP[1] with a circumference of 26.7 km. Centre of mass energies up to 14 TeV will be reached, thus the LHC will be the largest and most powerful collider in the world. It will also be able to accelerate heavy ions, for example lead ions.

The LHC can reach much higher beam energies (7 TeV) than LEP (108 MeV) because it is operated with 2000 times heavier particles: The energy loss due to synchrotron radiation of a charged particle with the mass m and the energy E on a circular track with a radius R is proportional to $\frac{E^4}{m^4 \cdot R}$. Thus, although working with the same radius, the energy loss of protons is much lower than the energy loss of electrons.

The protons of the two contrariously circulating beams are guided by 1232 14.3 m long superconducting dipole magnets, each reaching a magnetic field of around 8.4 T at the highest beam energies. Both proton beams, guided in two separate beam pipes within one support structure, are divided into 2808 bunches of $1.15 \cdot 10^{11}$ protons per bunch. With a revolution frequency of 11.25 kHz, this leads on average to a current of 0.582 A.

One very important parameter of every particle collider is its luminosity $\mathcal{L}$. It is a measure for the frequency of particle collisions. With a Gaussian beam distribution, N_b

[1] Large Electron-Positron Collider

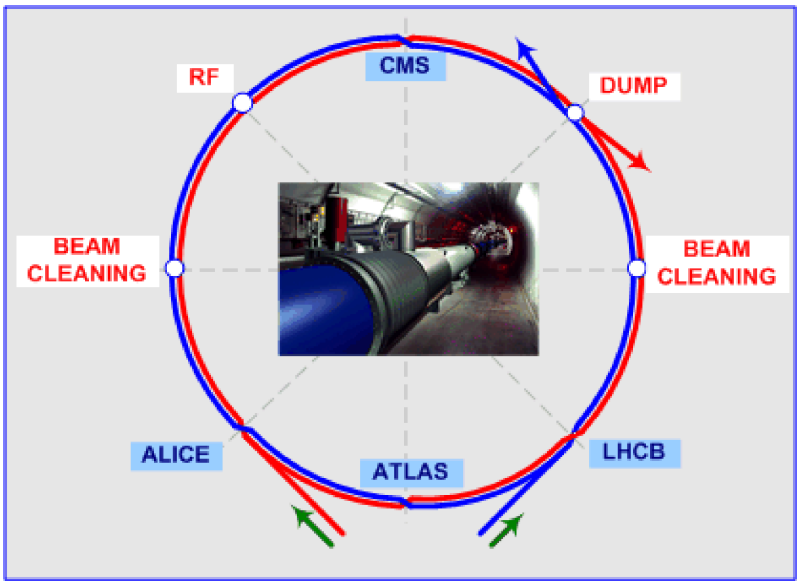

Figure 3.1: *Scheme of the Large Hadron Collider and its four experiments.*

particles per bunch, n_b bunches per beam and a revolution frequency f, the luminosity is approximately given by

$$\mathcal{L} = \frac{N_b^2 n_b f}{4\pi\sigma_x\sigma_y} \ , \tag{3.1}$$

where σ_x and σ_y are the beam widths in x- and y-direction.

The LHC design luminosity of $\mathcal{L} = 10^{34}\, cm^{-2}s^{-1}$ is foreseen for the bunch crossing areas of CMS and ATLAS[2].

3.1.2 The Experiments and Physics Goals

Collisions will take place every 25 ns at the four interaction points where the experiments ALICE[3], ATLAS, CMS and LHCb[4] are located. While ATLAS and CMS are multipurpose detectors, ALICE is specially designed for heavy ion physics and LHCb for b-physics.

With the LHC it will most likely be possible to discover new physics and to verify or exclude numerous theories. One major aim is the search for the Higgs boson and the determination of its mass. Other theories like supersymmetry (SUSY) or the quark-gluon-plasma will be investigated by the LHC-experiments.

3.2 CMS and its Subdetectors

CMS (Fig. 3.2) is a conventionally designed particle detector. It consists of several subdetectors that surround the LHC beam pipe like onion skins. The LHC beamline is the z-axis of CMS, the angle with respect to this axis is called θ and the angle around the beamline is called ϕ. In addition, the pseudorapidity η is introduced which is linked to θ

[2] A Toroidal LHC ApparatuS
[3] A Large Ion Collider Experiment
[4] Large Hadron Collider beauty experiment

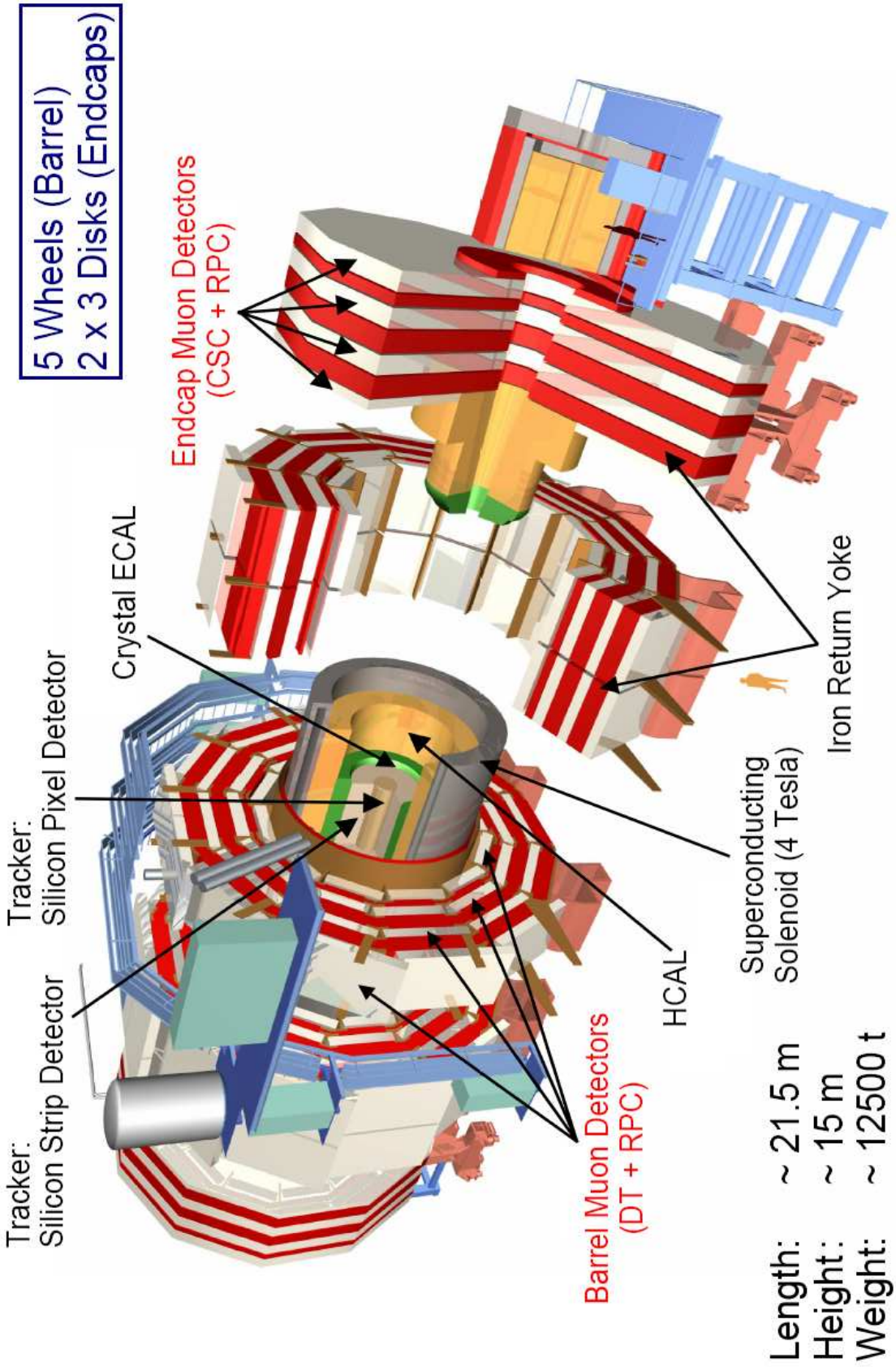

Figure 3.2: *The CMS Detector.*

by: $\eta = -\ln\tan(\theta/2)$. Thus, a large absolute value of η represents a small angle to the beam axis.

The detector is subdivided into the so called barrel region and the end caps. The barrel region consists of the solenoid magnet with the tracking system and the calorimeters inside. In addition five iron wheels constitute as return yoke for the magnetic field and hold the muon system. For particle detection in the forward region, three large discs are placed at both ends of the barrel region - the *end caps*. In total CMS reaches a length of 21.5 m, a diameter of 15 m and a weight of 12500 t.

3.2.1 The Tracking System

For track reconstruction and momentum measurement close to the interaction point, CMS uses a tracking system [7] consisting of a silicon pixel detector [8] and a silicon strip detector (Fig. 3.3). The tracker is operated at a temperature of $-10°$C to increase the lifetime of the silicon modules in the high radiation environment near the interaction point. Operating in a 4 T magnetic field, the tracking detectors have a fine granularity to cope with the high track densities close to the interaction region. Following a $1/r^2$-dependence, at a distance of 10 cm from the interaction point, a track density of 1 track/cm^2 is expected every 25 ns, while at a distance of 60 cm it is still 0.01 tracks/cm^2.

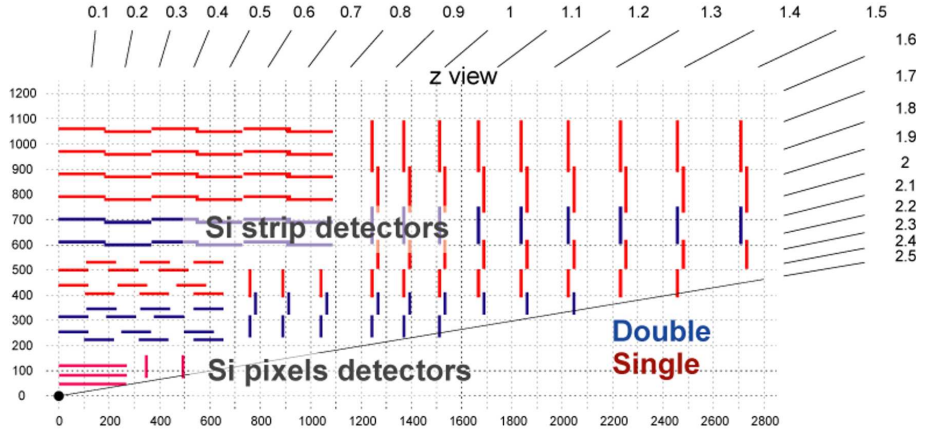

Figure 3.3: *Cross section of one quarter of the CMS tracking system. Some of the silicon modules are mounted double sided (back to back with the strips tilted by 100 mrad) for measuring both coordinates θ and ϕ.*

The three layers of the pixel detector are placed as close to the interaction point as possible. They are located at 4, 7 and 11 cm from the beam line. Due to the short distance to the interaction point, the pixel detector will have to stand and analyse very high particle fluxes. The pixel size is 100 μm $\times$ 150 μm which leads to a hit resolution of 10 μm in the ϕ-coordinate and 14 μm in the z-coordinate. The end caps cover the area between $r = 6$ cm and $r = 15$ cm from the beam line.

The silicon strip detector consists of the tracker inner barrel (4 layers), the tracker outer barrel (6 layers) and the end caps (9 large discs + 3 small discs in the inner end cap) and has an active area of approximately 210 m^2. It covers a cylindrical area with a diameter of 2.4 m and has a total length of 5.4 m. The strips are approximately 10 cm long, with an

offset of about 100 μm. These values vary slightly in the different layers of the silicon strip detector.

With those parameters, the tracker obtains for isolated charged leptons a momentum resolution of [9]

$$\Delta p/p = 15\% \, p_T[\text{TeV}] \oplus 0.5\% \tag{3.2}$$

dependent on the momentum that must be inserted in units of TeV. The notation $\oplus$ is defined by $a \oplus b = \sqrt{a^2 + b^2}$.

3.2.2 The Calorimeters

The calorimeters measure the energy of the incoming particles by absorbing them. For a precise measurement the particles must deposit their whole energy inside the calorimeters i.e. they must be stopped. The inner part is the electromagnetic calorimeter, measuring the energies of electrons, positrons and photons. Hadrons (like $\pi^{\pm}$, $p^{\pm}$, ...) deposit most of their energy within the hadronic calorimeter.

The Electromagnetic Calorimeter (ECAL)

The electromagnetic calorimeter [10, 11] is a scintillating crystal calorimeter built out of 80 000 lead tungstate ($PbWO_4$) crystals each with a length of 23 cm and a cross section of $22 \times 22\,\text{mm}^2$ in the barrel region and a length of 22 cm and a cross-section of $30 \times 30\,\text{mm}^2$ in the end caps. The crystal length corresponds to a thickness of 26 radiation lengths[5]. Lead tungstate was chosen because of its high density, leading to a short radiation length, a small Moliere radius[6] of 22 mm and a fast scintillation time of 25 ns. Those parameters allow to build a very compact calorimeter with an energy resolution of 1% for electrons with an energy of about 120 GeV.

The Hadronic Calorimeter (HCAL)

The hadronic calorimeter [12, 13] is a sampling calorimeter with 50 mm thick copper absorbers interleaved with 4 mm active scintillator sheets. The barrel hadronic calorimeter is constructed out of two 4.3 m long half-barrels, surrounding the tracker and the electromagnetic calorimeter, are placed inside the magnet coil. End cap hadronic calorimeters are placed at each end of the barrel, so that a hermetic coverage of up to $|\eta| = 3$ is guaranteed. The end caps are about 10 nuclear interaction lengths[7] thick, the barrel calorimeter has roughly 6 interaction lengths. Extra scintillators are placed outside the magnet coil, using the solenoid as additional absorber so that a total of 11 nuclear interaction lengths in the barrel region is reached.

To cover a region up to $|\eta| = 5$, two hadronic forward calorimeters are placed at the ends of CMS at a distance of 12 m from the interaction point. For being in a harsh radiation field, conventional materials could not be used for the forward calorimeters. Instead, they are built of steel absorbers and radiation resistant quartz fibers.

[5] The energy of an electromagnetic shower has dropped by a factor of 1/e after one radiation length.
[6] Moliere radius: The radius in which 90% of the shower energy is inclosed.
[7] The analogon for radiation lenghts in case of electromagnetic showers.

3.2.3 The Solenoid

The magnetic field of CMS is generated by a 12.5 m long superconducting coil with a diameter of roughly 6 m that is cooled with liquid helium. The coil provides a solenoidal magnetic field of up to 4 T, which allows a high resolution measurement of the transverse momentum of charged particles. The magnetic flux returns through the iron yoke that is instrumented with the muon system. The calorimeters and the tracking system are located inside the coil.

3.2.4 The Muon System

One of the main features of CMS, as the name Compact Muon Solenoid implies, is the good identification of muons and the exact measurement of their momentum, charge and direction. Since the muons are the only detectable particles that cross the calorimeters, long tracks are available for momentum measurement. The momentum resolution of the stand-alone muon system will be 8-15% $\Delta p_T/p_T$ for 10 GeV muons and 16-35% $\Delta p_T/p_T$ at 1000 GeV. In combination with the tracker information, the momentum resolution will be 0.8-1.5% $\Delta p_T/p_T$ at 10 GeV and 5-13% $\Delta p_T/p_T$ at 1000 GeV [14].

The Muon Drift Tubes (DT):

The muon detector in the barrel region consists of drift tube chambers that are installed on the magnet field return yoke. Fig. 3.4 shows one of the first cosmic muons seen by a whole sector of the barrel muon system during the commissioning of the muon chambers. As the object of this thesis is a gas monitoring device for the CMS barrel muon system, the muon DTs are described later in detail (see section 4.3.1).

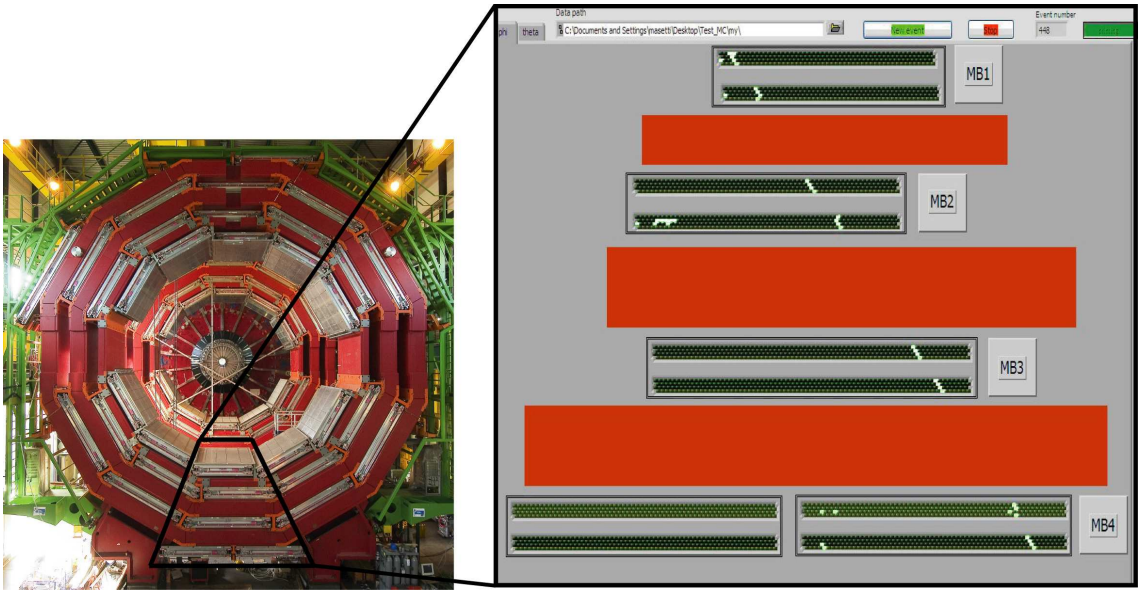

Figure 3.4: *One of the first cosmic muons seen in a complete sector of the CMS barrel muon system.*

The Cathode Strip Chambers (CSC):

The end cap muon system is instrumented with cathode strip chambers. These are trapezoidal multiwire proportional chambers with simultaneous readout of wires and cathodes. A chamber consists of 6 layers, each with two cathode planes, a gap filled with $Ar/CO_2/CF_4$ $(40/50/10)\%$ and a wire layer in between. The cathode plane is divided into strips with a width between 3.5 and 16.0 mm. Perpendicular to the cathode strips, the anode wires are strung with a pitch between 3 and 4.75 mm.

A traversing charged particle ionises gas molecules. In the applied electric field electrons from the ionisation drift to the anode wire, where they form an avalanche. A signal in the cathode strips is induced by the charges of the avalanche, so that one layer can measure two coordinates at the same time.

CSCs are used in the end caps, where the magnetic field is very inhomogeneous. Because of the short drift distances, the magnetic field has much less effect than it would have on the drift tubes.

The Resistive Plate Chambers (RPC):

Mainly for triggering purposes but also for redundancy, there is a third kind of muon detectors used in CMS: the resistive plate chambers, which have a very fast signal response (< 3 ns) and an excellent time resolution of $\delta_t < 1.3$ ns [15].

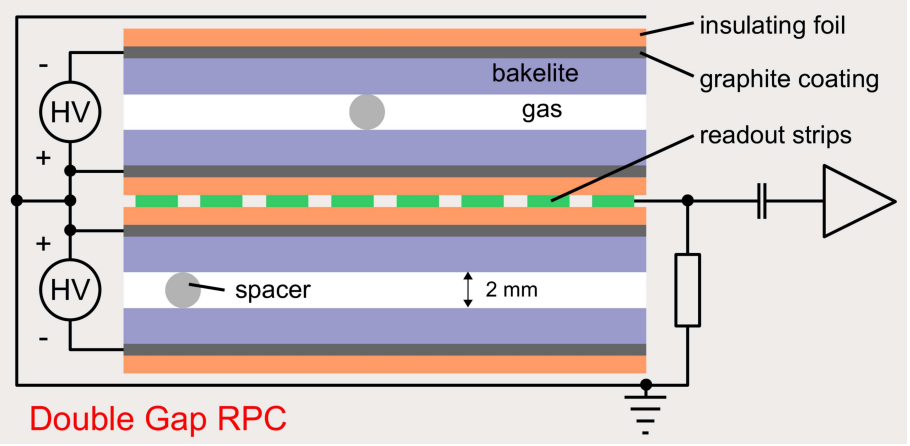

Figure 3.5: *Scheme of an RPC*

The CMS RPCs are double gap RPCs, where each gap consists of two high resistive bakelite plates with a gas gap inbetween and a graphite coating on the outside. The gas gap is filled with $C_2H_2F_4/iC_4H_{10}/SF_6$ in a $(96/3.5/0.5)\%$ ratio. A voltage of 9.5 kV is applied to the graphite coating, so that the field is strong enough to provide gas amplification in the gas gap. When the avalanche reaches the bakelite plates, they are discharged. This leads to a collaps of the electric field, so that the gas amplification is stopped. The avalanche and discharging takes place in a lateral region of about $0.1\,cm^2$, while rest of the chamber remains sensitive. The moving charges of the avalanche induce a signal in the aluminum electrodes placed isolated outside the graphite coating.

In CMS, RPCs are used in the barrel and in the end cap region. In the barrel, the RPCs are directly attached to the drift tube chambers: on both faces of the two inner stations and on one face of the outer two stations. In the end caps, the RPCs form four discs covering a range up to $|\eta| = 2.4$.

3.2.5 Trigger and Data Acquisition

As described in section 3.1 the proton beams cross each other every 25 ns at the CMS detector, corresponding to a bunch crossing rate of 40 MHz. With an average of 20 collisions per bunch crossing at the design luminosity, this leads to total number of about 10^9 interactions per second. With its 10^8 readout channels, CMS will produce a data rate in the order of 10^{15} bits per second, which is far to much to be all stored. Therefore, a three level trigger system [16, 17] is used to filter interesting events and reduce the data to a storable amount.

The level-1 trigger reduces the rate to about 100 kHz and is based on custom pipelined hardware processors. The information used for the data reduction are taken from coarse measurements in the calorimeters and the muon system. For the decision if an event is accepted, the event topology and the kinematical parameters transversal energy E_T and transversal momentum p_T are analysed. The decision has to be available after a limited time of 3.2 μs. For this time, the data are kept in the readout buffers.

If an event is accepted by the level-1 trigger, it is sent to the high level triggers. In the high level triggers, more time is available to analyse an event, so that data from the whole detector can be taken into account. The processing takes place in a farm of about 1000 commercial CPUs and can take up to 1 s of processing time per event. In this step, the rate is reduced to an event rate of 100 Hz with a size of 1 MB per event. In total, the triggers reduce the event rate by a factor of 10^7.

Chapter 4

Driftchambers

4.1 Function of a Drift Chamber

Drift chambers are gas filled detectors for the detection of charged particles. A charged particle traversing the gas volume at the time $t_0 = 0$ ionises some of the gas atoms, so that electron-ion-pairs are produced. In an electric field which is applied to the gas volume, the electrons and ions start drifting in opposite directions: the negatively charged electrons to the anode and the positively charged ions to the cathode. For the anode, usually a thin wire ($d \approx 20 - 50\,\mu$m) is used in order to obtain a high electric field nearby. Electrons reaching the vincinity of the anode wire after the drift time t_d are accelerated by this strong field so that they can ionise other gas molecules. As this process is repeated numerous times, the electrons form an enlarging avalanche that can be measured as a negative electric pulse. This process is known as charge multiplication.

If the time t_0 of the particle crossing is exactly known (e.g. from external triggers), the drift time t_d can be converted into a drift distance. For a known constant drift velocity v_d the distance x from the anode is:

$$x = v_d \cdot t_d. \tag{4.1}$$

Drift chambers only give information about the position, where a particle traversed the chamber, but not about the kind of particle.

4.2 Physics of Drift Chambers

An introduction to the physical processes inside a drift chamber shall be given on the following pages. Section 4.2.1 discusses shortly the impact of the gas on the drift properties. In section 4.2.2 the effects regarding the traversing particle are discussed while section 4.2.3 deals with the effects regarding the drifting electrons in the gas.

4.2.1 Drift Gases

In most cases, the drift gas is a noble gas, such as argon. Argon is often prefered, because it gives more primary ionisation than helium or neon and is not as expensive as the heavier noble gases krypton and xenon. Noble gases have higher ionisation potentials

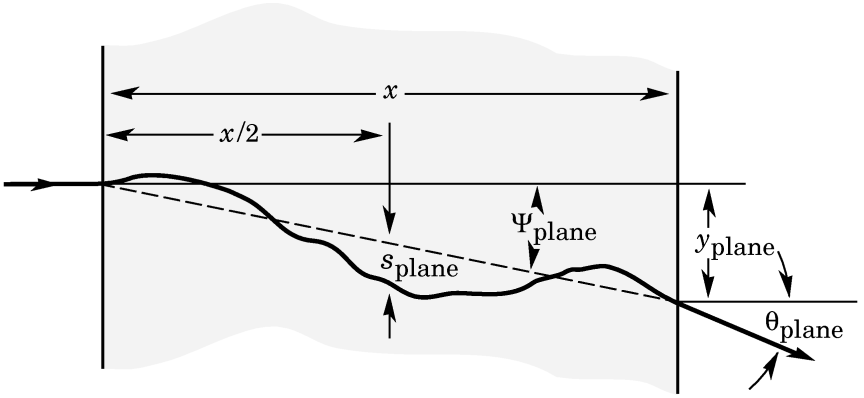

Figure 4.1: *Sketch to define the variables in multiple scattering* [2]

than other gases. For other gases, there are competing processes, such as molecular vibrational excitations, which will take away energy that will be lost for ionisation in the charge multiplication process.

With a pure noble gas a drift chamber cannot be run under stable conditions. When ionisation takes place, also excitation of atomic states can occur. The decay of the excitation states emits UV photons, some of which are energetic enough to ionise other gas atoms or, if they hit the cathode, create free electrons by the photoelectric effect. In both cases, the new electrons cause a new avalanche, leading in the worst case to a permanent discharging. For a pure noble gas, this happens at low anode voltages before one could reach a high gain.

This problem can be solved by adding a *quench gas* with polyatomic molecules like CH_4, C_4H_{10} or CO_2. In collisions with excited atoms of the noble gas, the quench gas absorbs the excitation energy. A molecule can then transfer a fraction of this energy to another quench gas molecule. In further processes, the energy can be shared between a large number of molecules, none of which will have enough energy to release electrons from the cathode.

Sometimes, electronegative gases like oxygen are added to the gas mixture. Such gases will capture electrons to form negative ions. This may allow higher anode voltages leading to larger charge multiplication. On the other hand, the ions have a low mobility, which reduces the amplification. A too large fraction of an electronegative gas may lead to a completely insensitive detector, because all electrons from the primary ionisation are captured.

However, there is no "perfect gas mixture". The optimal mixture for a detctor depends on the desired drift velocity and amplification. Other aspects may be the costs or security reasons.

4.2.2 Traversing Particles

Multiple Scattering

A charged particle traversing a medium is deflected by many small-angle scatterings. The dominating process is the interaction with the Coulomb field of the nuclei in the medium. For small angles the angular distribution is roughly Gaussian with a width of [2]

$$\theta_{plane}^{rms} = \theta_0 = \frac{13.6\,MeV}{\beta p} z \sqrt{\frac{x}{X_0}} \left[1 + 0.038 \ln\left(\frac{x}{X_0}\right)\right]. \tag{4.2}$$

This formula is valid for elementary charged particles with an accuracy better than 11% for $10^{-3} < \frac{x}{X_0} < 100$. Here β, p and z are the velocity, the momentum and the charge number of the scattered particle, $\frac{x}{X_0}$ is the thickness of the passed medium in radiation lengths[1].
The quantities shown in Fig.4.1 can be calculated according to reference [2]:

$$\Psi_{plane}^{rms} = \frac{1}{\sqrt{3}}\theta_0 \tag{4.3}$$

$$y_{plane}^{rms} = \frac{1}{\sqrt{3}} x\theta_0 \tag{4.4}$$

$$s_{plane}^{rms} = \frac{1}{4\sqrt{3}} x\theta_0 \tag{4.5}$$

Energy Loss

a) Energy Loss of Charged Heavy Particles in Matter

The energy loss of a charged particle inside a medium is mainly caused by interactions with the atomic shell. The mean value of the energy loss dE of an elementary charged particle with a mass $m \gg m_e$ by interactions with the atomic shell when travelling the distance dx can be described by the Bethe-Bloch formula [1]:

$$\left(\frac{dE}{dx}\right)_{ion} = \frac{4\pi N_A \alpha^2}{m_e \beta^2} \rho \frac{Z}{A} (C + \ln \beta^2\gamma^2) \tag{4.6}$$

$$\begin{aligned}
m_e &= \text{electron mass} \\
\alpha &= \frac{e^2}{\hbar c} \approx \frac{1}{137} \quad \text{(fine structure constant)} \\
\beta &= v/c \quad \text{(particle velocity)} \\
\gamma &= \frac{1}{\sqrt{1-\beta^2}} \\
Z &= \text{charge number of atoms in the medium} \\
A &= \text{mass number of atoms in the medium} \\
N_A &= 6.02 \cdot 10^{23}/\text{mol} \\
\rho &= \text{mass density} \\
C &\approx 8 \quad \text{(dependent on the material)}
\end{aligned}$$

[1] The mean distance over which a high-energy electron looses all but 1/e of its energy [2].

The energy loss depends only on the velocity β, not on the mass of the particle. The graph of the Bethe-Bloch formula (Fig.4.2) reaches after a fast decrease for small $\beta\gamma$ a minimum for $\beta\gamma \approx 4$. For $\beta \to 1$, $\frac{dE}{dx}$ increases slowly. This so called "relativistic rise" is caused by the logarithmic term of (4.6). A particle with $\beta\gamma$ close to the minimum is called "Minimum Ionising Particle" (MIP).

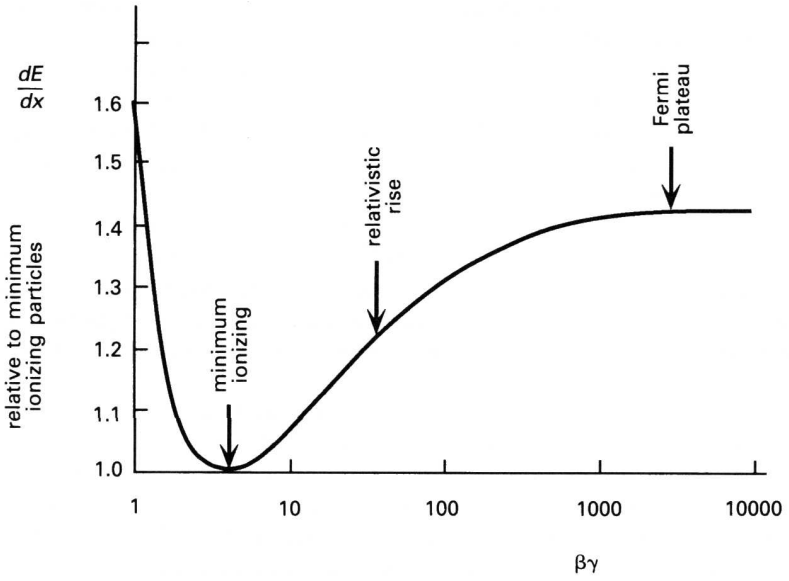

Figure 4.2: *Variation of the mean rate of energy loss dE/dx for a fast charged particle in a medium as a function of* $\beta\gamma$ [18].

b) Energy Loss of Electrons

In the small gas volume of the drift velocity monitoring chamber, the traversing particles that interact with the atomic shell are electrons. For the energy loss of an electron, it must be taken into account, that the interacting particles are identical and that electrons with an energy of a few MeV are already relativistic ($\beta = v/c \approx 1$).

The energy loss by ionsiation is dominating up to a critical energy of [2]

$$E_C = \frac{710MeV}{Z + 0.92} \tag{4.7}$$

For Argon (Z=18), we receive $E_C = 37.5\,\text{MeV}$. Electrons with a higher energy will loose most of their energy by bremsstrahlung[2]. The ionising electrons in the drift velocity monitoring chamber have a maximum energy of $E_{max} = 2.28\,\text{MeV}$, so that it is sufficient to discuss the energy loss by ionisation.

For relativistic electrons, the Bethe-Bloch-equation (4.6) changes to [1]

$$\left(\frac{dE}{dx}\right)_{ion,e} = \frac{4\pi N_A \alpha^2}{m_e}\rho\frac{Z}{A}\left(\frac{1}{2}\ln\gamma^2 + D\right) \qquad D \approx 7 \tag{4.8}$$

[2]Bremsstrahlung: The radiation emitted by an accelerated charged particle within a coulomb field

4.2.3 Drifting Electrons

Electron Drift and Diffusion

Free electrons produced by the ionisation process collide with gas molecules and thus quickly lose a part of their energy until they reach the Maxwellian probability distributions of energy ϵ and velocity v [19]

$$F(\epsilon) = A\sqrt{\frac{\epsilon}{kT}} \cdot e^{-\epsilon/kT} \tag{4.9}$$

$$F(v) = \left(\frac{m}{2\pi kT}\right)^{3/2} e^{-mv^2/2kT} \tag{4.10}$$

where ϵ is the thermal energy of the particle, k the Boltzmann constant, T the temperature of the gas and C the normalisation constant for the energy distribution. The average thermal energy is

$$< \epsilon >= \int_0^\infty \epsilon F(\epsilon) d\epsilon = \frac{3}{2} kT. \tag{4.11}$$

The average velocity $\overline{v} := \sqrt{< v^2 >}$ can be calculated using the correlation between the kinetic and the average thermal energy:

$$\tfrac{1}{2} m < v^2 > = \frac{3}{2} kT \tag{4.12}$$

$$\Rightarrow \quad \overline{v} = \sqrt{\frac{3kT}{m}}. \tag{4.13}$$

The direction of this velocity is randomly changed by scatters on the gas molecules so that free electrons starting at $t_0 = 0$ from the origin will be diffused, forming the following Gaussian density after a time t [20, 21]:

$$\frac{dN}{N} = \frac{1}{\sqrt{4\pi Dt}} e^{-x^2/4Dt} dx. \tag{4.14}$$

$\frac{dN}{N}$ ist the fraction of electrons found in the element dx at a distance x from the origin. The standard deviation of this distribution is $\sigma_x = \sqrt{2Dt}$ for one dimension or $\sigma_V = \sqrt{6Dt}$ for the three-dimensional distribution. D is the diffusion constant that is linked to the mean free path λ between two collisions and the average velocity $\overline{v}$ of the electrons:

$$D = \frac{\overline{v} \cdot \lambda}{3} \tag{4.15}$$

In presence of an electric field E, the electrons are accelerated in the direction of the field, gaining an additional velocity $u = eE\tau/m_e$ between two collisions. τ is the mean time between two collisions. For small fields, the energy distribution stays thermal with $\epsilon_0 = \frac{3}{2}kT \approx 0.04\,\text{eV}$ (at room temperature) while for stronger fields, the energy gain

between two collisions dominates the energy distribution. Macroscopically, the effect of this additional velocity appears as the drift velocity v_d that is characteristic for a given gas and field configuration. It can be shown, that the drift velocity is [22]:

$$v_d = \frac{2}{3}\frac{eE}{m}\left\langle\frac{\lambda}{\overline{v}}\right\rangle + \frac{1}{3}\frac{eE}{m}\left\langle\frac{d\lambda}{d\overline{v}}\right\rangle. \tag{4.16}$$

The averaging is done over the velocity distribution of the electrons. The mean free path λ results from the number density N of the gas molecules and the scattering cross-section $\sigma(\epsilon)$:

$$\lambda = \frac{1}{N\sigma(\epsilon)} \tag{4.17}$$

$$\overline{v} = \sqrt{\frac{2\epsilon}{m}} \tag{4.18}$$

Replacing λ and $\overline{v}$ with $\sigma(\epsilon)$ and ϵ, equation 4.16 becomes:

$$v_d = \frac{1}{3}\frac{eE}{mN}\left(\left\langle\sqrt{\frac{2m}{\epsilon}}\frac{1}{\sigma(\epsilon)}\right\rangle + \left\langle\sqrt{\frac{2m}{\epsilon}}\epsilon\frac{d}{d\epsilon}\frac{1}{\sigma(\epsilon)}\right\rangle\right) \tag{4.19}$$

For this equation, the averaging is done over the energy distribution of the electrons. For small drift fields, the part in brackets becomes constant because the energy distribution is the thermal energy distribution (4.9) with a constant $<\epsilon>=\epsilon_0$. In this case, we obtain the following relation:

$$v_d \sim \frac{E}{N}. \tag{4.20}$$

And with the Ideal Gas Law $pV = N\,k\,T$:

$$v_d \sim \frac{ET}{p}. \tag{4.21}$$

Thus, for thermal drift electrons, one would expect a linear dependence of the drift velocity on the electric field. An increasing electric field E will lead to a higher velocity u because of a higher acceleration. A decreasing pressure p has the same effect due to an enlargement of λ. For being able to work with a constant drift velocity, one would have to make great efforts to hold the parameters E, p and T constant.

For electrons in stronger drift fields E, the mean energy exceeds ϵ_0 and varies with E so that additional effects occur, such as variations in the scattering cross-section. In some gas mixtures it is possible to find a region where the effects of a higher u and the variations in the cross-section cancel out each other, so that the drift velocity v_d remains constant when varying E or p.

The theoretical description of processes for non thermal electrons [23, 24] is much more complicated than for the thermal electrons. Although the dependency of the drift velocity on the *reduced electric field* E/p is not linear any more, it is common practice to regard the drift velocity as a function of E/p.

Charge Multiplication

When the drifting electrons reach the anode, their number is too small to generate a detectable electric signal without further amplification. This amplification can be achieved in a very strong electric field where the drifting electrons gain enough energy to ionise further atoms. The resulting free electrons themselves can ionise other atoms, so that the number of free charges increases exponentially. Strong fields occure in the vincinity of charged thin wires. The electric field of wire at the distance r from the wire centrum is given by

$$E(r) = \frac{\lambda}{2\pi\epsilon_0}\frac{1}{r}, \tag{4.22}$$

where λ is the linear charge density on the wire. In the easiest setup, a cylindrical arrangement of anode and cathode (Fig.4.3) with the capacity $C = \frac{2\pi\epsilon_0}{\ln(b/a)}$ and the potential difference $V_0 = V(b) - V(a)$ between anode and cathode (a = radius of the anode wire, b = radius of the cathode), the electric field is [21]:

$$E(r) = \frac{C \cdot V_0}{2\pi\epsilon_0}\frac{1}{r} = \frac{V_0}{\ln(b/a)}\frac{1}{r} \tag{4.23}$$

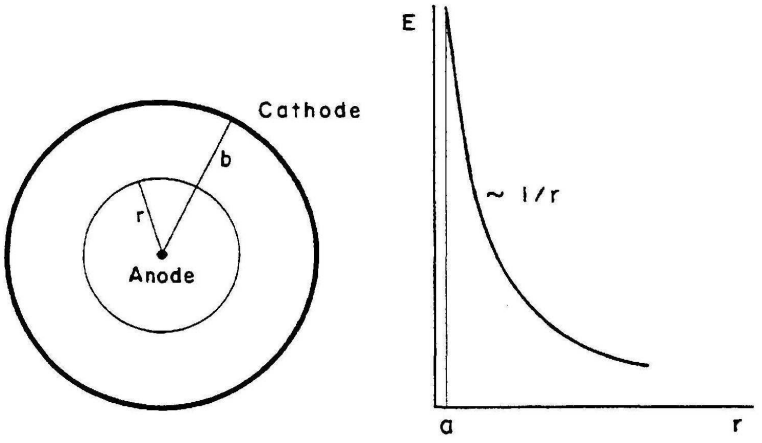

Figure 4.3: *Sketch of a cylindrical drift cell and its electric field* [21].

If the potential V of the wire exceeds a critical value V_T, the electric field around the wire is large enough to allow charge multiplication. The time development of this process is shown in Fig.4.4: An electron starts drifting towards the anode. In regions of higher fields, gas atoms are ionised. Due to the lateral diffusion, the increasing number of electrons and ions forms a drop-like avalanche around the anode wire. Because of their higher mass, the ions are drifting slowly (10^3 times slower than the electrons) to the cathode.

Common values for the anode wire diameter are 20–50 μm, leading to amplifications by a factor of up to 50 000, so that signals in the order of mV can be achieved at the anode.

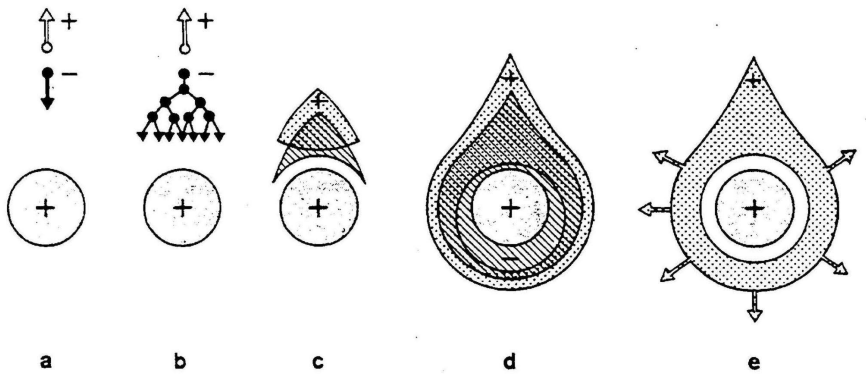

Figure 4.4: *Development of a charge avalanche [21]: a) An electron-ion pair is generated. b) The electron is accelerated by the electric field and ionises other atoms. c) The electrons continue drifting to the anode wire, still ionising more atoms. d) Now, the electron cloud surrounds the anode wire. d) The electrons are collected by the anode wire and a cloud of ions drifts to the cathode.*

4.3 The CMS Muon Barrel Drift Tubes

4.3.1 The Drift Tubes (DT)

In the barrel region of CMS, four stations of muon drift tube chambers (DT) are installed in concentrical cylinders inbetween the iron of the return yoke. The stations are numbered from MB1 (innermost) to MB4 (outermost). The chambers of the inner three stations consist of three so called superlayers, while the MB4 have only two superlayers. A superlayer is built out of four layers of drift cells. The design of the drift cell is shown in figure 4.5. Two of the three superlayers are designed to measure the bending in the r-ϕ-plane, the other is for the θ-coordinate. A charged particle passing through a cell ionises the gas. Due to the electric field, primary electrons start drifting to the anode wire. Near the wire, the electric field becomes strong enough for charge multiplication and thus an electric signal in the anode wire can be measured. Knowing the exact drift time and the drift velocity of the electrons, the position where the particle has crossed the cell can be calculated.

The drift cells (Fig. 4.5) have a pitch of 42 mm in width and 13 mm in height, and a length of 2.5 m for the ϕ-superlayers and 2-4 m for the θ-superlayers depending on the station. The left and right boundaries of the cell, the so called I-beams, hold the cathodes with a voltage of up to $U_C = -1200\,\mathrm{V}$. In the cell center, an anode wire with a voltage of $U_A = +3600\,\mathrm{V}$ is strung. For field shaping purposes, two field forming stripes ($U_F = +1800\,\mathrm{V}$) are glued isolated on the grounded aluminium plate. The gas inside the DTs is $\mathrm{Ar/CO_2}$ with a (85/15)%-ratio which is held slightly beyond normal pressure. With electric fields of $2 - 2.5\,\mathrm{kV/cm}$, this leads to an almost costant drift velocity of $v_d = 55\,\mu\mathrm{m/ns}$ (see also chapter 4.3.2) along the cell width. This is important because the level-1 trigger assumes a linear time to drift distance relation to save computing time. For offline analysis, the real time to trift distance relation can be used.

To calculate the distance to the anode wire from the drift time, the drift velocity must be exactly known and in the easiest case, it is constant over the entire volume. As described in section 4.2.3, the drift velocity depends amongst others on the gas mixture and on

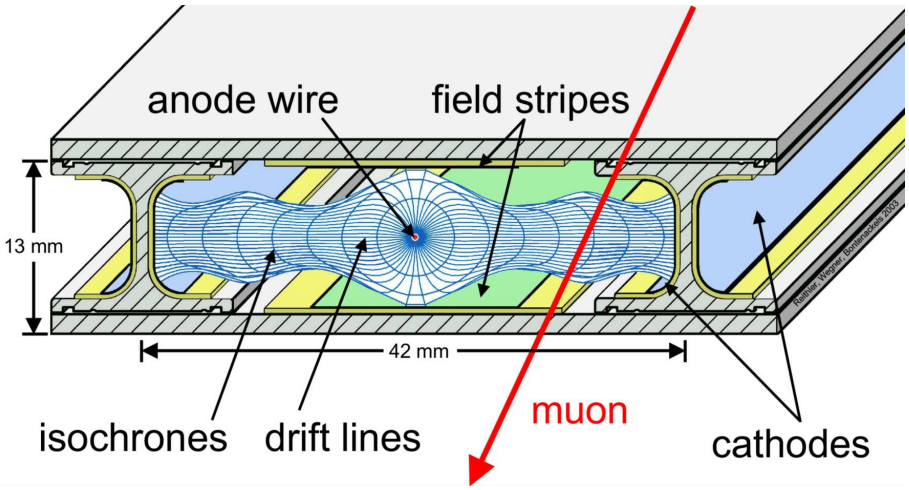

Figure 4.5: *Cross section of a muon barrel DT drift cell with drift lines and isochrones.*

the electric field. Despite the field stripes, the electric field inside the drift cells is not completely homogeneous (see Fig. 4.6 (right)). Thus it is necessary to adjust the gas mixture and field strength in a way that field fluctuations do not lead to a varying drift velocity. Fig. 4.6 shows, that the drift velocity in the drift cells is almost constant although the electric field varies from 1 to 3 kV/cm in the main drift region. The raise of the electric field near the anode wire cannot be prevented for geometrical reasons ($E \sim \frac{1}{r}$) and is needed for charge multiplication.

4.3.2 The Gas

The properties of the gas used in the CMS barrel muon system are discussed in the following paragraphs.

For the selection of the drift gas in the CMS barrel muon system, different aspects need to be considered. CMS will be operated underground so that one wants a non-flammable gas and, as CMS has a very large volume, the costs should be as low as possible. Organic components are avoided, because they are possible sources of aging effects especially in areas of high radiation. Since the trigger assumes a linear space-drifttime relationship, the drift velocity in the gas should be independent from the not completely homogeneous drift field.

Ar/CO_2-mixtures fulfill all those requirements for CO_2 fractions between 10% and 20%. For fractions below 10%, the quenching properties are poor, resulting in discharges at relative low voltages and for fractions above 20% the plateau where the drift velocity is independent of the eletcric field becomes to short (see Fig. 4.7).

Therefore an Ar/CO_2 mixture in a (85/15)% ratio is used.

Ionisation in Ar/CO_2

In this gas mixture, a minimum ionising particle ionises an average of 30 atoms/cm and for every ionisation process there will be about two secondary ionisations. Thus, a particle produces around 100 free electrons/cm.

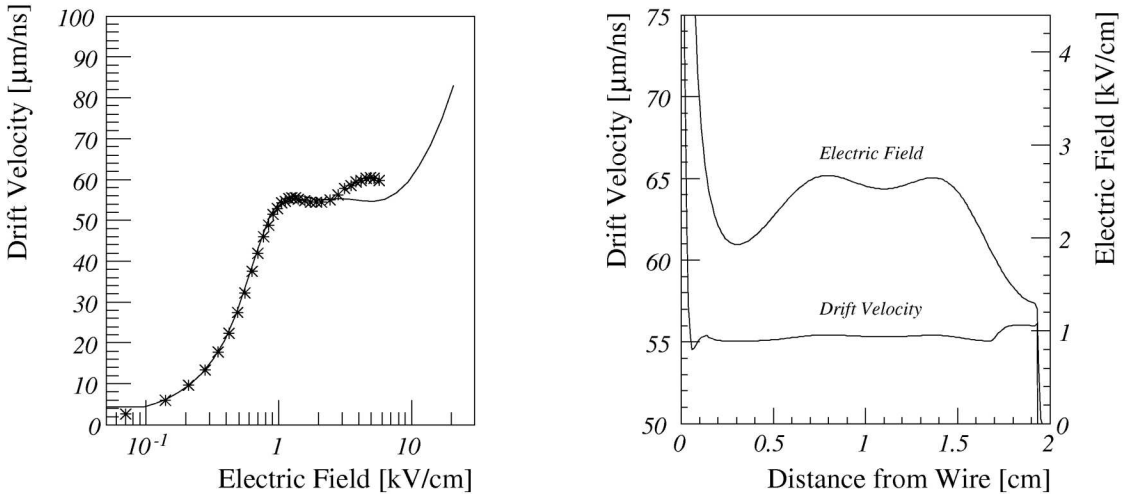

Figure 4.6: *Left: The drift velocity in Ar/CO_2 (85/15) as a function of the electric field strength. Right: The electric field and drift velocity as a function of the distance to the anode wire in the muon barrel drift cells at normal pressure [25].*

Electron Drift in Ar/CO_2

The average drift velocity for different gas mixtures of Ar/CO_2 is shown in Fig. 4.7. For the mixture used in the CMS barrel muon drift tubes, there is a plateau at a drift velocity of $v_d = 55\,\mu$m/ns from about 1 kV/cm up to 5 kV/cm. Impurities in the gas lead to different effects. Oxygen for example is a gas with a high electronegativity which catches free electrons, leading to a smaller or vanishing signal. Nitrogen influences the drift velocity, so that the relation between position and drift time changes.

4.3.3 The Gas System

A scheme of the muon barrel drift tube gas system is shown in Fig. 4.8. Five pipes leave the mixer room, one for each wheel. Flow, pressure and temperature are monitored for each line. At every wheel, the gas input is split, so that the gas flows simultaneously through the 50 muon chambers. At every chamber, the gas supply is split again to flow in parallel through the three superlayers. The gas flow for an entire chamber is about 50 l/h, for a superlayer 17 l/h. At the outlet of the chamber, the three pipes from the superlayers are joined again. At this manifold, lines to the gas analysers with a flow of about 5 l/h are branched off, so that the gas from each chamber can be analysed separately. The other branch is merged with the gas outputs from the other chambers and wheels before it returns to the mixer room, where the gas is cleaned and sent back into the circuit. The cleaning is done by filters with an organic material, filtering out mainly oxygen.

The pressure in the gas circuit will be held at a constant level slightly above the external pressure. If the difference to the external pressure exceeds a limit of 10 to 20 mbar (the exact value is not yet defined), the pressure is changed by e.g. 20 mbar to he next level [27]. Thus, there are only a few discrete pressure values, for which the gas properties are well known.

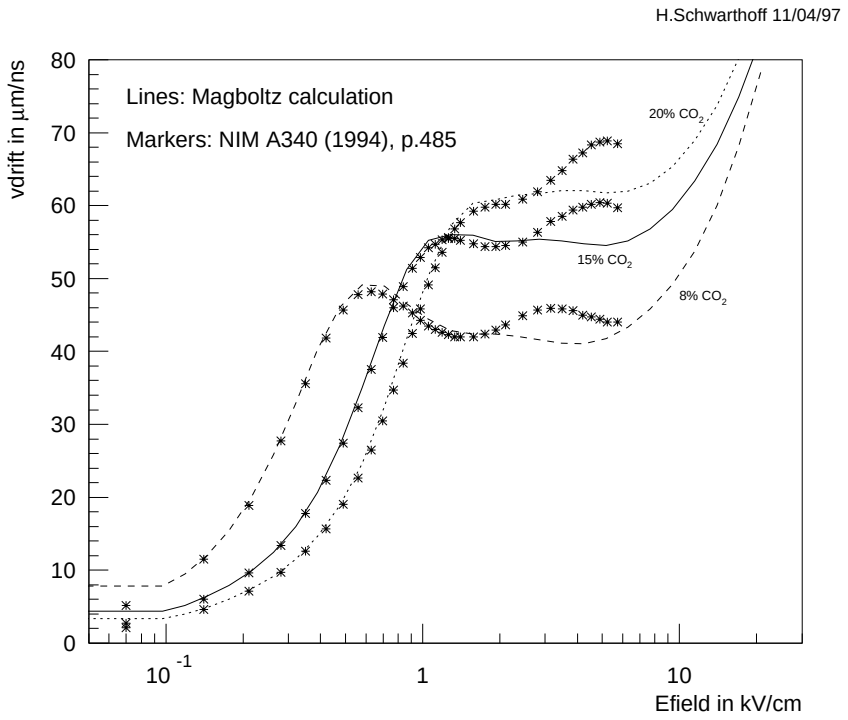

Figure 4.7: *The drift velocity for different mixtures of Ar/CO_2 as function of the electric field [26].*

4.3.4 The Gas Monitoring

Two devices are intended to check the gas quality: an oxygen analyser and a small drift chamber for a direct monitoring of the drift velocity. The oxygen analyser is a commercial device[3], while the development of the drift velocity monitoring chamber is the object of this diploma thesis.

If there are impurities in the gas, they most probable come from leaks in the pipes or the chambers. The oxygen analyser can determine the proportion of oxygen in the chamber gas, allowing to calculate the contamination by nitrogen, additional CO_2, and other components of air. In a gas mixture, oxygen can be detected and removed most easily, while the filtering of nitrogen is much more difficult. Thus, the fraction of nitrogen and the other gases is not known any more after the gas cleaning. Another aspect is, that even if the kind of impurity is known, one does not know its impact on the drift velocity. Therefore it is necessary to monitor the drift velocity directly with a dedicated drift chamber.

Requirements for the Drift Velocity Monitoring Chamber

The time resolution of the barrel muon drift cells is about $3 - 5\,\text{ns}$. The dominating effects limiting the resolution is the bending of the isochrones (Fig. 4.5) combined with the ionisation statistics. With a drift velocity of $55\,\mu\text{m/ns}$, a maximum drift distance of

[3]The oxygen analyser will be bought just in time for the start of CMS. Thus, the type and working principle is not known yet.

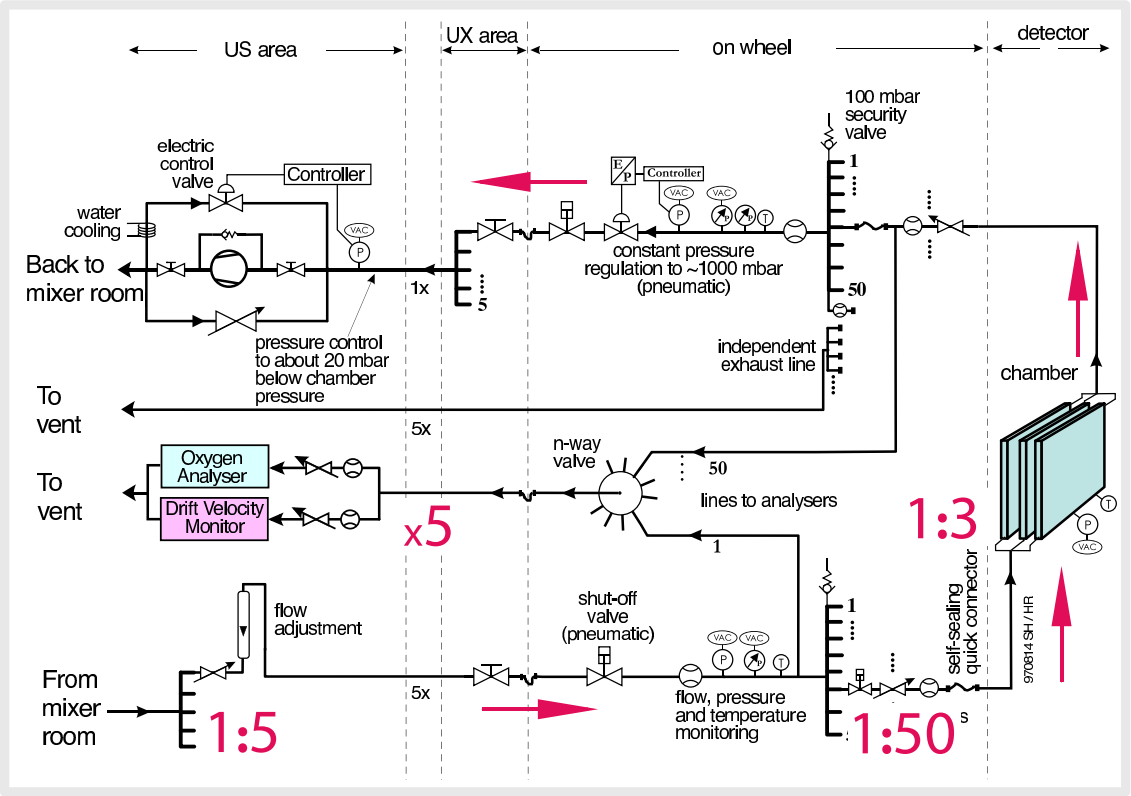

Figure 4.8: *The CMS muon barrel drift tube gas system [25].*

21 mm, and a resulting maximum drift time of $t_{max} = 380\,\text{ns}$, the time resolution is roughly 1% of t_{max}. Thus, the drift velocity should vary much less than 1% or should be known at least better than 1%.

Therefore, the objective of the drift velocity monitoring chamber (VdC) is to be able to **detect variations** of **0.1%** in the drift velocity.

If the VdC operates with a drift field on the plateau of the drift velocity (Fig. 4.7), the requirements on the homogeneity of the electric field inside the chamber are not very high, because the drift velocity in this region does not depend on the electric field. If there are impurities in the gas, the shape of this function changes and one does not know if there is still a plateau. In the case of a linear relation between v_D and E, the field homogeneity should be in the same order of magnitude as the sensitivity on variations.

For being more sensitive on variations, it is advantageous to operate the chamber outside the plateau. In this case one would want to have one defined field value to be able to establish a relation between the exact electric field and the drift velocity.

Although the resolution $\Delta v_D / v_D$ for variations is not directly connected to the field homogeneity $\Delta E/E$, one wants - due to the reasons given above - values in the same order of magnitude:

$$\frac{\Delta E}{E} \approx \frac{\Delta v_D}{v_D} \approx 0.1\,\% \tag{4.24}$$

Another aspect is the measurement of the absolute value of the drift velocity. This is much more difficult, because the chamber needs a precise calibration and a good under-

standing of systematic errors is essential. However, measuring an **absolute value** is **not necessary** for the function of the chamber!

4.3.5 Resolution of Drift Chambers

The effects described in the last sections limit the possible resolution of drift chambers. First, the ionising particle will not pass along an isochrone, so that electrons starting to drift from the particle's path will not reach the anode at the same time. The initial line of drifting electrons is additionally diffused according to the fact that the electrons will not start with zero velocity, but will have initial velocity that will in general not be along the drift line. Once the electrons start to drift, they underlie the effect of diffusion. As in general one electron is sufficient to start a measurable avalanche at the anode wire, the measured time wil be defined by the fastest of the electrons.

Chapter 5

The Drift Velocity Monitoring Chamber

5.1 Concept of the Chamber

The drift velocity monitoring chamber (VdC) for the CMS barrel muon drift chambers is based on a similar chamber [28, 29] used for the central tracker of the former L3-detector. This tracker was a time expansion chamber (TEC), operated with a gas mixture of CO_2/i-C_4H_{10} in a (80/20)% ratio, a pressure of 1.2 bar and a drift field of $E = 864\,\mathrm{V/cm}$, leading to a drift velocity of approximately $5.9\,\mu\mathrm{m/ns}$. A redesign of the gas monitoring chamber was necessary because of the higher drift field strength ($> 2\,\mathrm{kV}$) in CMS.

VdC	The Drift Velocity Monitoring Chamber (v_d-Chamber)
SC1	The thin scintillator
SC2	The thick scintillator
PMT1	The photomultiplier for the signals from SC1
PMT2	The photomultiplier for the signals from SC2

Table 5.1: *Definition of abbreviations*

Figure 5.1 shows a cross section of the VdC and its working principle. The chamber is divided into a drift volume and a detection volume. In the drift volume, the electric drift field is generated by the cathode with a variable voltage of up to 15 kV, the grounded separation plate between the drift and detection volume, and the field forming electrodes that make the field homogeneous in the drift region. The voltage supply of the field electrodes is derived from the cathode's voltage via a resistor chain (Fig. 5.2), dividing the cathode voltage in equal steps from the maximum voltage down to 0 V. Thus, the field strength can be changed by varying the cathode's voltage, while the field's shape always stays the same.

The gas in the chamber is ionised by two electron beams, originating from two radioactive ^{90}Sr sources each with 5 MBq activity. Both beams are separated by a distance of $\Delta x = x_2 - x_1$. After passing through the chamber, the electrons are detected by two scintillators whose coincidence gives the start signal for the time measurement. Meanwhile, the electrons from the ionised gas start to drift in the electric field towards the detection

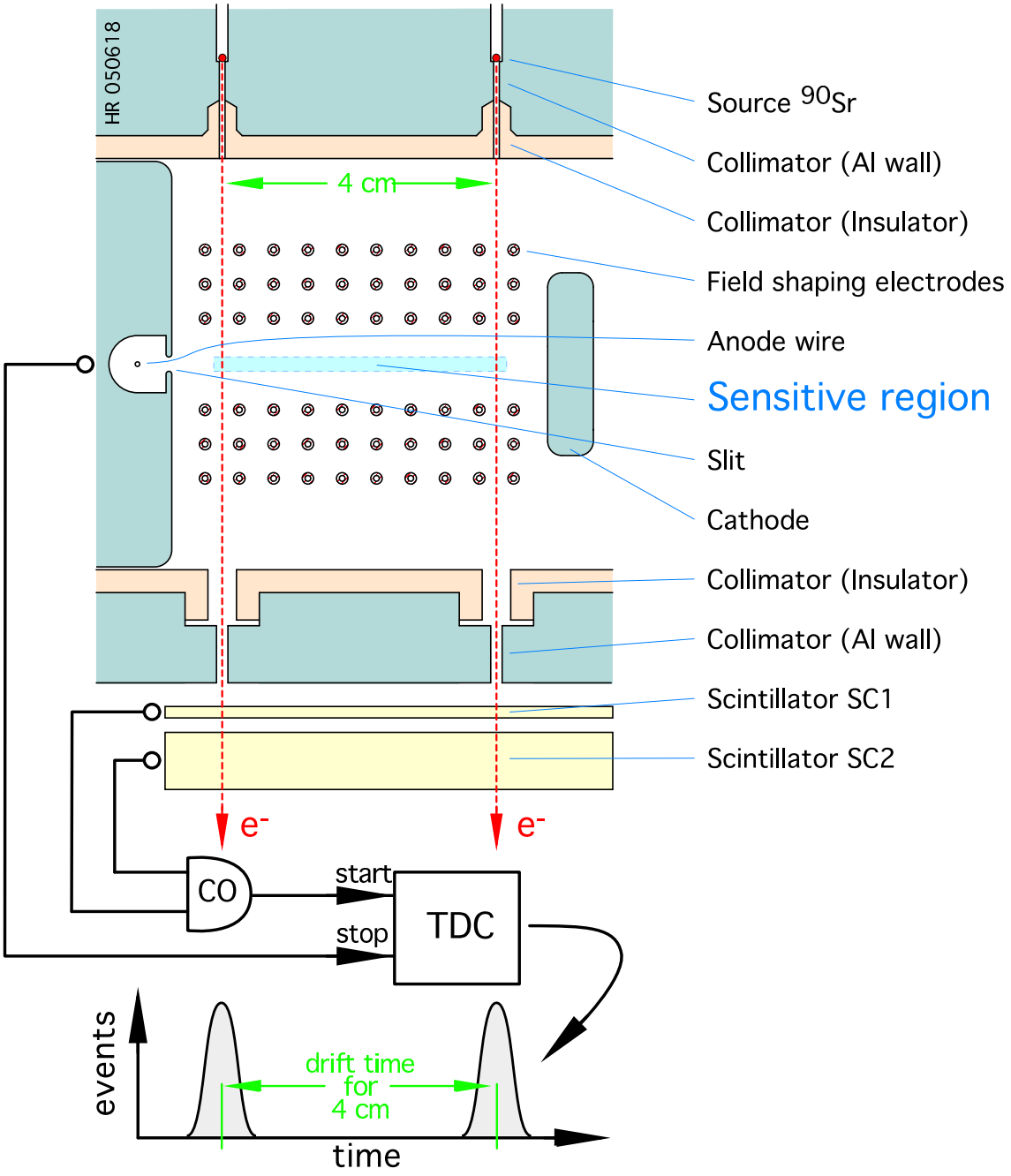

Figure 5.1: *Principle of the drift velocity monitoring chamber VdC [27]: When an electron from the ^{90}Sr-sources passes the drift chamber, a trigger signal is generated by the scintilators, while the electrons resulting from ionisation inside the gas volume drift to the anode wire, where their arrival is registered as an electric signal. The TDC measures the time difference between the two signals. Many of those measurements are combined in a drift time histogram from which the drift velocity can be derived.*

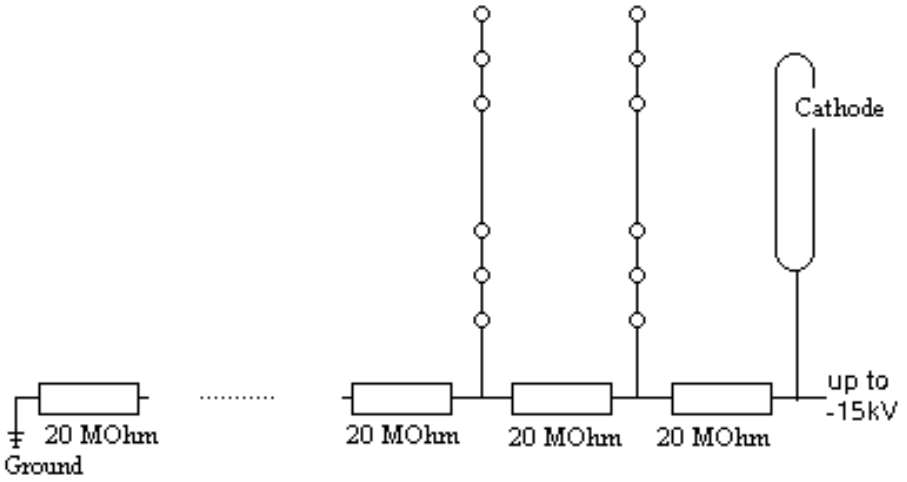

Figure 5.2: *Circuit diagram for the field shaping electrodes. By changing the cathode voltage, one can vary the field strength without changing the field shape. The values of the resistors between the different rows of electrodes are chosen such that they reduce the current.*

volume. Due to the design of the chamber, only the electrons that start to drift in the middle region, the so called *sensitive region*, can reach the detection volume while all other electrons are stopped at the field electrodes or the chamber walls. Thus, only the electrons which drift through the most homogeneous part of the electric field are taken into account for the determination of the drift velocity.

In the detection volume, the electric field is given by the grounded walls and the anode wire. In the region near the anode wire, the electrons are amplified by charge multiplication, providing a measurable signal. This signal is amplified, digitised and sent to a TDC[1] that measures the time between the startsignal from the scintillators and the arrival of the drifting electrons.

The combination of several measurements in a drift time histogram, leads to a drift time spectrum with two peaks as indicated in Fig. 5.1. The peaks represent the two drift times t_1 and t_2 from the two ionising β^- beams to the anode wire. As the electric field is homogeneous between the two electron beams, the drift velocity is constant and can easily be calculated:

$$v_d = \frac{\Delta x}{\Delta t} \qquad \text{with} \quad \Delta t = t_2 - t_1. \tag{5.1}$$

The advantage of this method is, that the drift time Δt is measured in a region where the drift field is nearly homogeneous. The unavoidable inhomogeneities near the anode wire affect both drift time measurements and thus cancel out when calculating the drift time.

5.2 The Radioactive Sources

For the radioactive sources, ^{90}Sr was chosen, because of its decay properties, especially its half-life time and the energy of its β-spectrum. A high energetic β-source is needed, since

[1] Time to Digital Converter

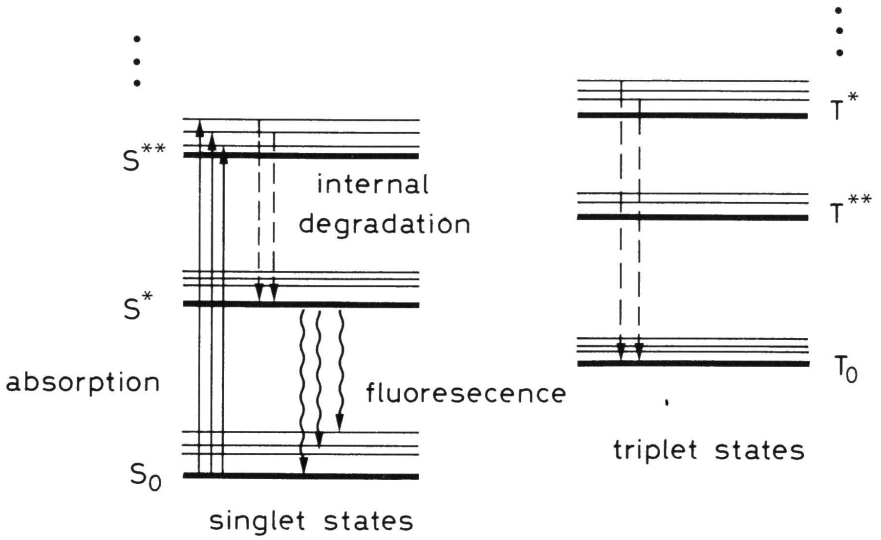

Figure 5.3: *Energy level diagram of a plastic scintillator with the spin singlet (denoted by S) and triplet (denoted by T) states*[30].

the electrons have to traverse the first scintillator to generate a signal in both scintillators for a coincidence measurement. An electron with an energy less than 1.2 MeV [28] does not reach the second scintillator. Only two nuclides emit electrons with a sufficient kinetic energy: ^{106}Ru ($E_{max} = 3.54\,\text{MeV}$) and ^{90}Sr ($E_{max} = 2.28\,\text{MeV}$). The use of ^{106}Ru was not reasonable because of its short half-life time (1.02 y). During the CMS runtime, the sources would have to be changed several times. ^{90}Sr has a half-life time of 28.5 y, so that the activity of the sources is large enough during the whole runtime.

^{90}Sr is a pure β^--source, decaying in a two step process into the stable ^{90}Zr:

$$^{90}\text{Sr} \xrightarrow{0.55\,\text{MeV}} {}^{90}\text{Y} \xrightarrow{2.28\,\text{MeV}} {}^{90}\text{Zr}. \tag{5.2}$$

Only the electrons from the ^{90}Y decay have enough energy to pass through the first scintillator. The half-life of this decay is 64 h so that the lifetime of the source is dominated by the ^{90}Sr decay.

Activity of the ^{90}Sr-Sources

The sources used for the prototype have an activity of 5 MBq each. The main reason for working with this activity is that this is the highest activity the institute is authorized to use without further safety arrangements. The following rough estimate shall evaluate the expected trigger rates.

To enter the chamber volume the β^- have to pass a first collimator, which has a circular profile of 1 mm diameter and a length of 17 mm corresponding to a solid angle of $\Omega_1 = 8.68 \cdot 10^{-4}\pi$ which is $2.17 \cdot 10^{-4}$ of the total solid angle. With an activity of 5 MBq, 1085 β^- per second reach the drift volume from each of the sources.

The second collimator at the opposite chamber wall is a 2 mm × 10 mm slit at a distance of 109 mm from the source. Only 6.42 mm from the 10 mm can be "seen" by the source

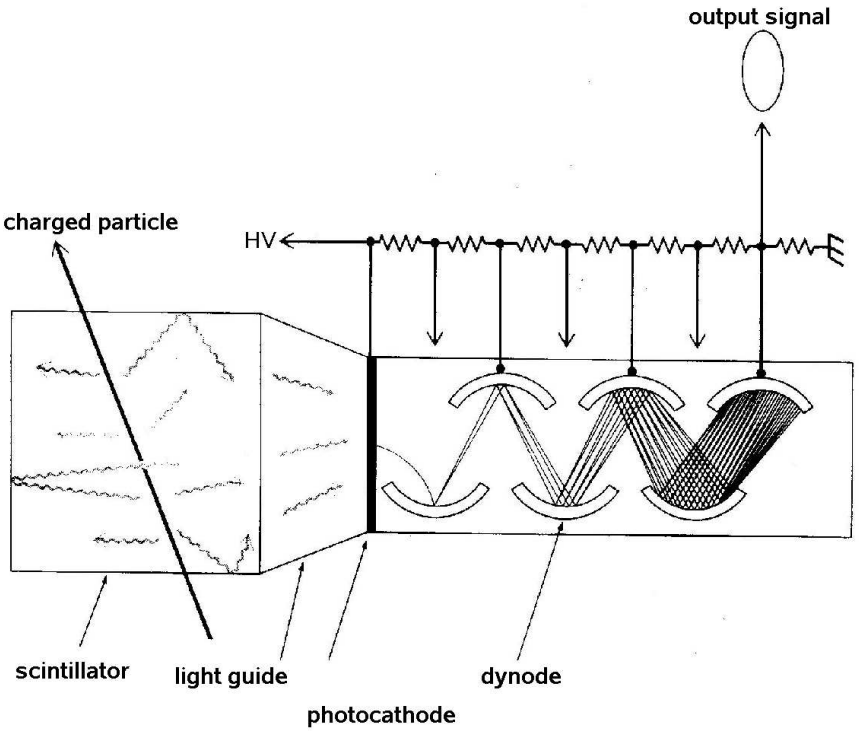

Figure 5.4: *Sketch of a photomultiplier with a scintillator attached to it* [1].

through the first collimator. This area covers $\Omega_2 = 3.44 \cdot 10^{-4}\pi$ or $8.6 \cdot 10^{-5}$ of the total solid angle, leading to a rate of 430 Hz at the scintillators.

Taking into account that roughly half of the electrons of the ^{90}Y-β-spectra have an energy too low to pass the first scintillator, one expects a coincidence rate of 215 Hz from each of the sources.

Neglecting multiple scattering and the detection efficiencies of PMTs[2] and scintillators, one should be aware that this estimate gives only a rough benchmark.

5.3 The Trigger

The β^- reaching the scintillators produce a light signal that is guided to the photomultipliers (PMTs). In the PMTs, the light signal is transformed into an electric pulse which is discriminated and sent to a coincidence unit that provides the start signal for the time measurement.

5.3.1 The Scintillators

The Scintillators used for the VdC are organic plasctic scintillators. Responsible for the scintillation process are free valence electrons that are not associated with a particular atom in the molecules. An energy diagram is shown in Fig. 5.3, where the spin singlet

[2] PMT = photomultiplier tube

state S_0 is the ground state. The bold lines are excited electron levels while the thin lines represent the vibrational levels.

A particle entering the material excites electrons to higher states (S^*, T^*, S^{**}, T^{**}, ...). The electrons from higher singlet states quickly fall back to the S^* state without emission of radiation. The S^* state decays in the process of *fluorescence* to one of the vibrational states of the ground state S_0 within a few ns, emitting a photon.

The excited spin triplet states decay radiationless to the lowest triplet state T_0 which falls to the ground state by interaction with another T_0 excited molecule: $t_0 + T_0 \rightarrow S^* + S_0 + Phonons$. Phonons are the quanta of lattice oscillations.

As the fluorescence photons result from decays to a vibrational state, they do not have enough energy to excite an electron from the ground state S_0. This explains the transparency of the scintillator to its own radiation. Thus, the photons can leave the scintillator and are detected e.g. by photomultiplier tubes.

5.3.2 The Photomultipliers

The photons produced in the scintillators are guided to the photomultipliers (Fig. 5.4). Reaching the PMT, the photons hit a photocathode where they produce electrons via $\gamma - e$ conversion through photoeffect. Those electrons are accelerated by an electric field to a dynode, where secondary electrons are emitted. This procedure is repeated through several dynode stages producing more and more electrons. Arriving at the anode at the end of the PMT the number of electrons is sufficient to give a measurable electric pulse.

Chapter 6

Simulation of the VdC

To optimize the geometry of the chamber - especially with regard to the electric field - the VdC was simulated with two different computer programs: **Garfield** and **COMSOL Multiphysics**. Computer simulations have the advantage, that one can try a lot of different geometries without building a prototype.

6.1 The Tools

6.1.1 Garfield

Garfield is a text based computer program for detailed two- and three-dimensional simulations of the physics processes in drift chambers [31]. For two-dimensional simulations, the geometry of the drift chamber can be generated directly with Garfield. For three-dimensional geometries, Garfield can import field maps, generated by finite elements software such as *Maxwell* [32], *Tosca* [33], *QuickField* [34] and *COMSOL Multiphysics*[35]. Garfield has interfaces to the programs *Magboltz* [36] and *Heed* [37] that simulate ionisation and electron transport in various gases.

In this thesis, Garfield is mainly used for simulations of the electric field inside the VdC.

Simulation and Calculation of the Electric Field

The structure of a Garfield simulation is explained in appendix A. The boundaries of the drift cell geometry can be specified as infinite planes or circular surfaces with a constant potential. These boundaries of the cell geometry are the only planes accepted by Garfield. All other surfaces must be built up by numerous circular surfaces.

Inside those boundaries, wires or tubes (pipes that surround wires) can be entered and to each wire or tube an electric potential can be assigned.

The eletric fields and potentials are computed in the *thin wire approximation*, neglecting dipole and other higher order terms. Therefore, care has to be taken that the wire diameters are small compared to the inter-wire distances. The computation is done in two steps:

- First, the charges on the wires and a reference potential are calculated in a way that the potential given in the CELL-section is produced on the wire surface.

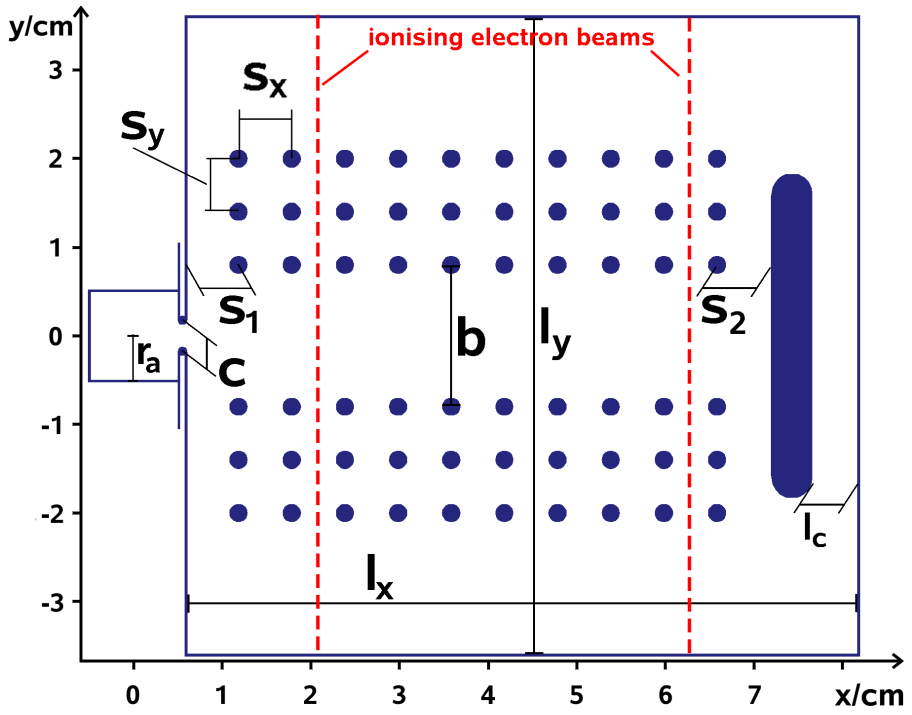

Figure 6.1: *Sketch of the VdC as simulated with Garfield including an overview of the variables used in this chapter.*

- In the second step the contributions of each wire to the field and potential at a given point are added up.

6.1.2 COMSOL Multiphysics

COMSOL Multiphysics was used, because Garfield is only able to generate geometries in 2D. Thus, it was necessary to check with another program, if the length in z-direction (along the field electrodes) is sufficient to avoid field components in this direction. COMSOL Multiphysics is a commercial software for the simulation of physical processes with finite elements methods.

The geometry can be entered via a graphical user interface similar to that in CAD programs. Physical properties (e.g. the electric potential) of the different elements have to be defined, from which COMSOL Multiphysics creates a so called *mesh*: The geometry is parted in small triangles (2D) or tetrahedrons (3D). The physical process is translated in partial differential equations with the physical properties as boundary conditions.

6.2 Optimisation of the E-Field Homogeneity

Starting from the geometry of the L3 gas test chamber, the geometry is optimised for the needs of CMS. The design has to be changed because of the higher voltages needed for

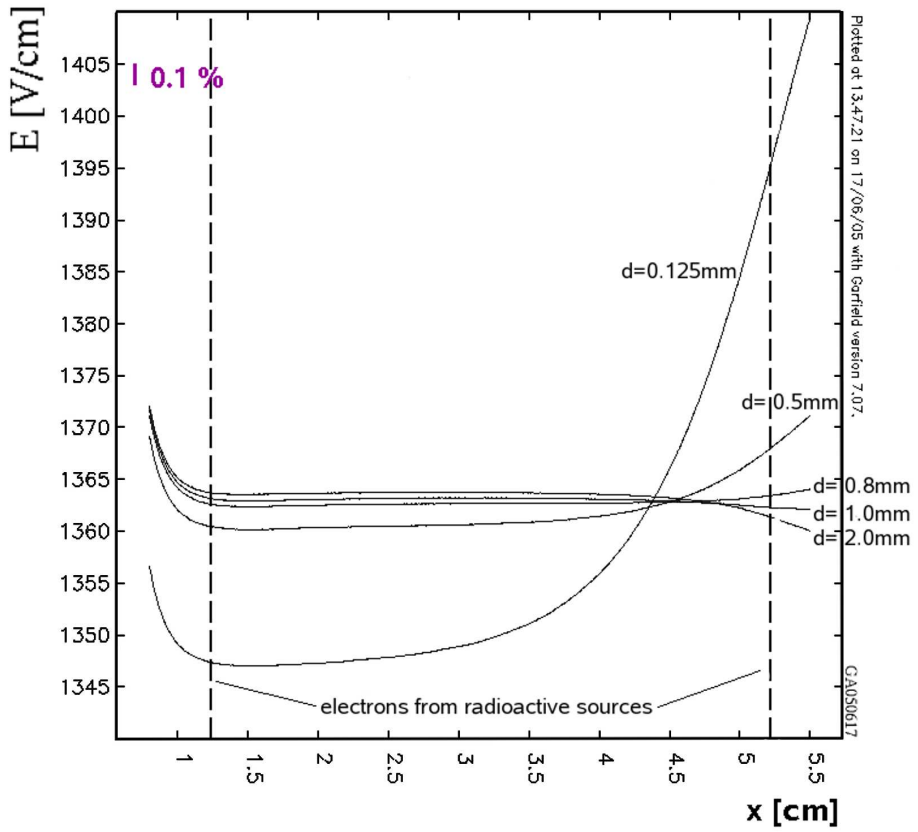

Figure 6.2: *The impact on the electric field along the central drift line (y=0) as a variation of the diameter d of the field shaping electrodes. The anode wire is at $x = y = 0$. The plot was computed with the first Garfield simulation: the results are not correct in detail but the main conclusions are nevertheless valid.*

CMS. The opportunity has been taken to study and to improve the field's homogeneity. Different - sometimes contradictory - aspects have to be considered:

- The electric field in the sensitive region should be as homogeneous as possible to be able to measure at a defined electric field.
- The chamber volume should be kept small so that the gas can be exchanged fast in order to measure gas samples from different muon chambers.
- The VdC must stand the high voltage needed to set up an electric field of more than 2 kV/cm to measure under the same conditions as they are present in the muon drift tubes. For this reason the distances between the parts with the highest voltage (cathode, field shaping electrodes) and the grounded walls needs to be sufficiently large.

Chapter 6.2.1 describes the simulations done with Garfield for the first prototype, but those simulations did not lead to the correct field, because the thin wire approximation was not taken into account adequately [38]. Nevertheless, these studies help to understand the dependence of the electric field on different chamber geometries. In the sections 6.2.2 and 6.2.3, the simulations with COMSOL Multiphysics are described, that made it possible to

find and correct the error on the first Garfield simulation. The results of the improved Garfield simulation are presented in 6.2.4.

6.2.1 Simulations for the Prototype

A major improvement of the field homogeneity was achieved by using small tubes (outer diameter $d = 2\,\text{mm}$) instead of wires as field shaping electrodes. Fig. 6.2 shows the impact of the diameter of the electrodes on the electric field. For diameters between 0.8 mm and 2 mm, the field homogeneity reaches its maximum. The value of 2 mm was taken for mechanical reasons: since the tubes cannot be strung with a tension like wires, they should be as stable as possible to prevent deformations. Due to the larger diameter, it is necessary to increase the field electrode spacing from 5 mm to 6 mm (from centre to centre) to have enough space for fixation and insulation.

With the 2 mm-electrodes the field is already very homogeneous in the middle region, but still needs improvement near the cathode and near the detection volume. This might be achieved by a variation of the resistor values in the resistor chain (as done for the L3-chamber, see chapter 5.1). However, therefore the absolute value of the resistors must be known very precisely, which is difficult for high resistor values. In contrast, small differences of the resistor values can be determined precisely e.g. by a *Wheatstone Bridge*. As the resistors used for the VdC resistor chain have very high values of about 20 MΩ, it was decided to use resistors with equal values.

Another way to modulate the electric field is performed by a variation of the distances between the given potentials. Therefore the fine-tuning can be done by varying the distances s_1 and s_2 between the first electrode row and the wall and the last row and the cathode respectively. Figure 6.3 shows the impact on the electric field as a variation of those two distances.

The following list describes further parameters which have been varied in order to study their effects on the electric field in the VdC:

- Number of layers and rows of field shaping electrodes:

  The field becomes more homogeneous when using more layers and/or rows. Since a larger number of layers/rows increase the volume of the chamber and the construction efforts, it was found that three layers and ten rows are sufficient.

- Enlargement in y-direction:

  Increasing the width of the chamber influences the field in the sensitive region slightly, but for minimizing the chamber volume, the grounded walls are placed as near as possible to the electrodes. However, the distance has to be large enough to prevent discharges between the electrodes and the walls.

- Enlargement in x-direction:

  Increasing the distance l_c between cathode and wall has no effect on the field in the sensitive region. Thus, l_c is defined by the needs of the electric strength and the fixation of the cathode.

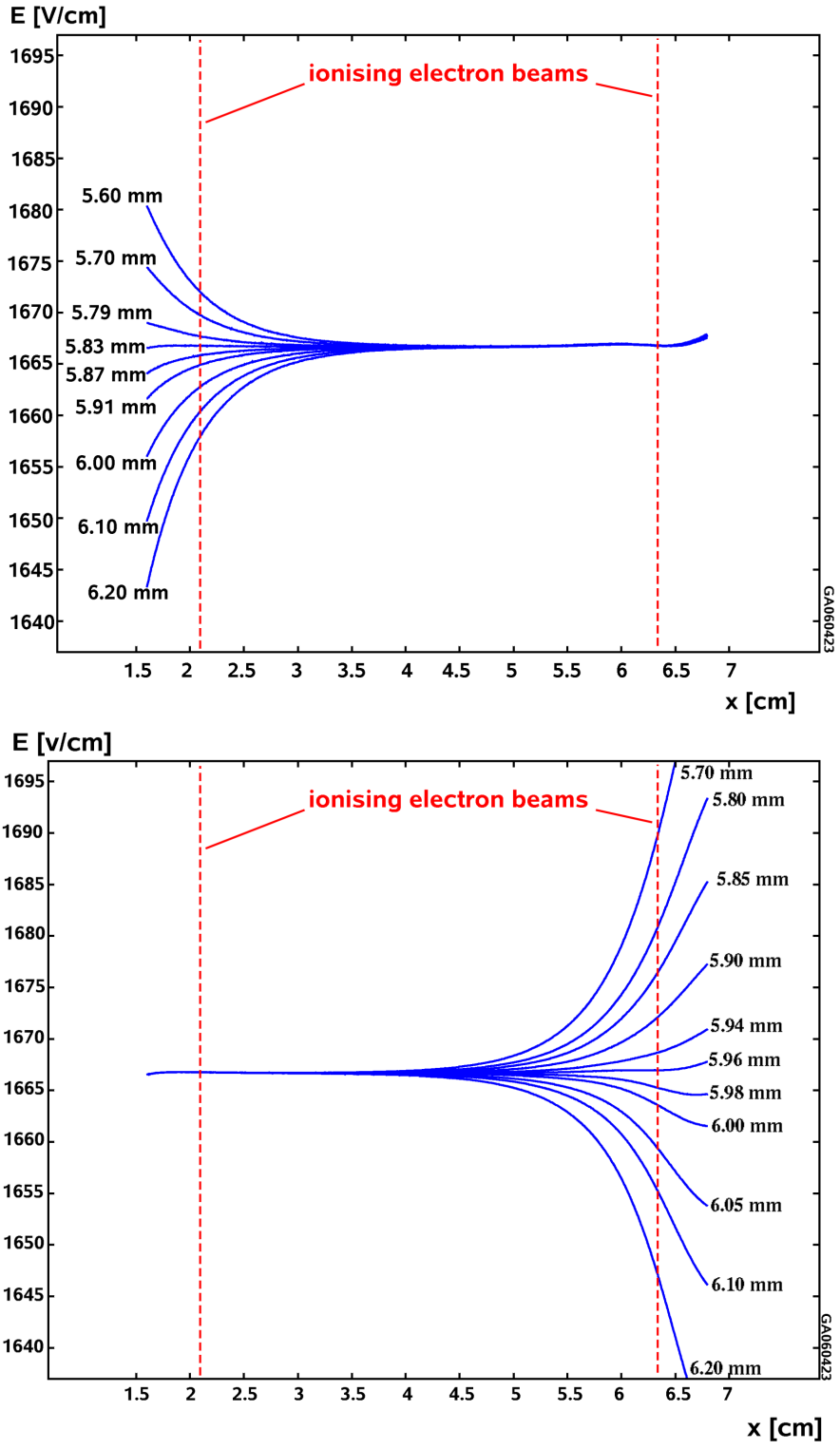

Figure 6.3: *(top) The impact on the electric field along the central drift line (y=0) as a variation of the distance s_1 between the centre of the first row of field shaping electrodes and the grounded wall to the detection volume. These plots are used to determine s_1 and s_2 for the prototype. Later simulations (section 6.2.4) lead to slightly changed values. (bottom) The impact on the electric field along the central drift line (y=0) as a variation of the distance s_2 between the centre of the last row of field shaping electrodes and the cathode.*

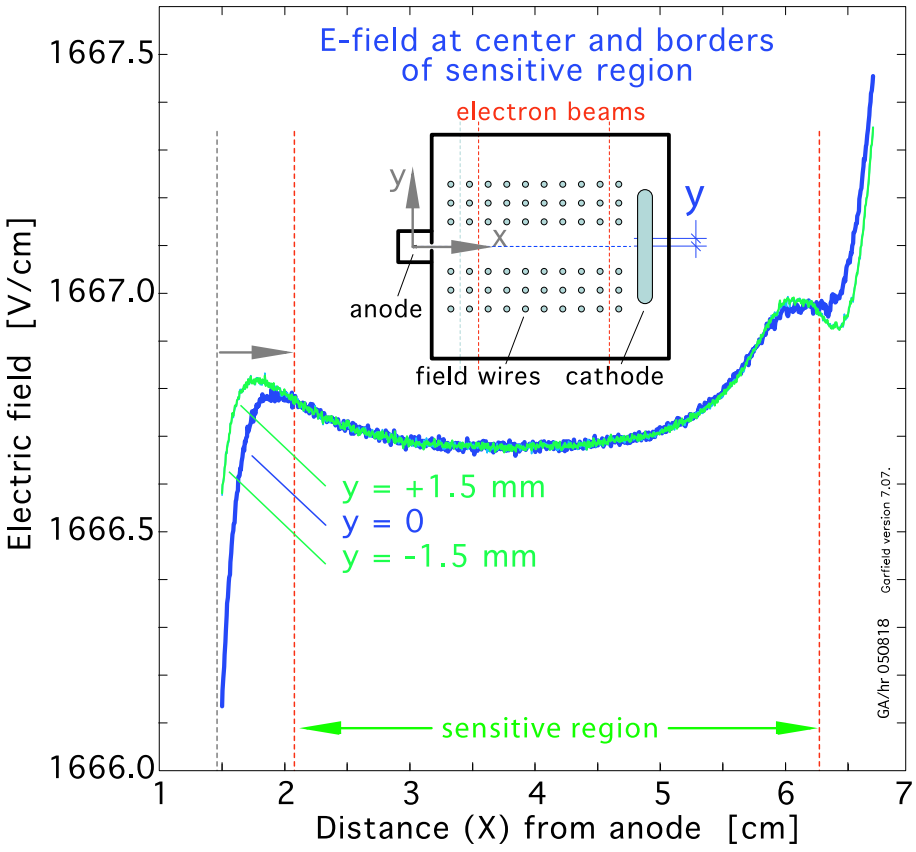

Figure 6.4: *The electric field along the central drift line ($y = 0$) and along $y = \pm 1.5\,mm$. The dashed lines display the places, where the β^- beams traverse the chamber. As a result of the field shape, the source at $x = 1.5\,cm$ (dashed grey line) was moved to $x = 2.1\,cm$ (dashed red line) to avoid the strongly inhomogeneous region. Note that this plot was created with the first simulation. The results of the improved simulation are introduced in section 6.2.4.*

- Geometry of the slit between detection volume and drift volume:

  Slit size and shape affect the electric field slightly in a way that can be compensated by adjusting the distance s_1. Thus, the solution of maximum field strength was chosen for the shape: a half-circle. The slit size c is kept as small as possible to prevent drift time differences between the electrons at different y-positions. For a width of 2.5 mm, about 25 drifting electrons per event will pass the slit, which are enough to achieve a measurable signal after the charge multiplication in the vincinity of the anode wire. The additional drift distance for electrons passing at the outer regions is 154 μm (in the approximation of a straight drift path from the slit to the anode wire) which leads to a drift time difference of roughly 3 ns, which is negligible with respect to the pulse width.

- Geometry of the detection volume:

  The effect of the geometry (size and shape) of the detection volume on the electric field in the drift volume is negligible: the wall between drift volume and detection volume separates the electric fields of the two volumes.

Description	Variable in Fig. 6.1	VdC	L3-Chamber
Field electrode spacing in x- and y-direction	s_x s_y	6 mm	$s_x = 5$ mm $s_y = 4$ mm
Width of drift volume in y-direction	l_y	72 mm	52 mm
Width of drift volume in x-direction	l_x	96.79 mm	65 mm
Distance of the two middle layers of electrodes	b	16 mm	16 mm
Number of rows of field shaping electrodes	–	10	10
Number of layers of field shaping electrodes	–	3	3
Diameter of field shaping electrodes	d	2 mm	0.125 mm
Distance from wall to first row of electrodes	s_1	5.83 mm	5 mm
Distance from last row of electrodes to cathode	s_2	5.9 mm	5 mm
Radius of the detection volume	r_a	5 mm	5 mm
Cathode length in y-direction	–	32 mm	32 mm
Diameter of anode wire	d_A	25 μm	30 μm

Table 6.1: *Parameters of the layout of the prototype. The distances are given with respect to the aluminum surfaces of the walls and the centres of the electrodes. The values are determined on the basis of the first simulation. For the chambers being built in future, some of the parameters have to be slightly changed due to the improved simulation (section 6.2.4).*

- Diameter of the anode wire:

  The diameter of the anode hardly influences the electric field in the drift volume, so that it is defined by the needs of the charge multiplication (a smaller diameter leads to a higher amplification).

The simulation leads to the parameters given in table 6.1, defining the geometry of the prototype. The resulting electric field is shown in figure 6.4. One can see, that the field is not only homogeneous along the central drift line ($y = 0$) but also at the border regions ($y = \pm 1.5\,mm$).

6.2.2 2D-Simulations with COMSOL Multiphysics

As explained before, COMSOL Multiphysics was intended mainly to simulate the VdC in 3D, but simulations in 2D have also been performed to cross-check the results of the Garfield simulation. The calculated field (Fig. 6.5) differs strongly from the Garfield result (Fig. 6.4). The outstanding effects are the wiggles with a height of $\approx 0.1\%$ of the field strength, but also the overall field shape is slightly different. However, the field variations in the area between the two electron beams stay below 0.5 %.

As the distance between two wiggles is exactly 6 mm, they clearly originate from the field electrodes. The improved Garfield simulation (section 6.2.4) confirms this effect.

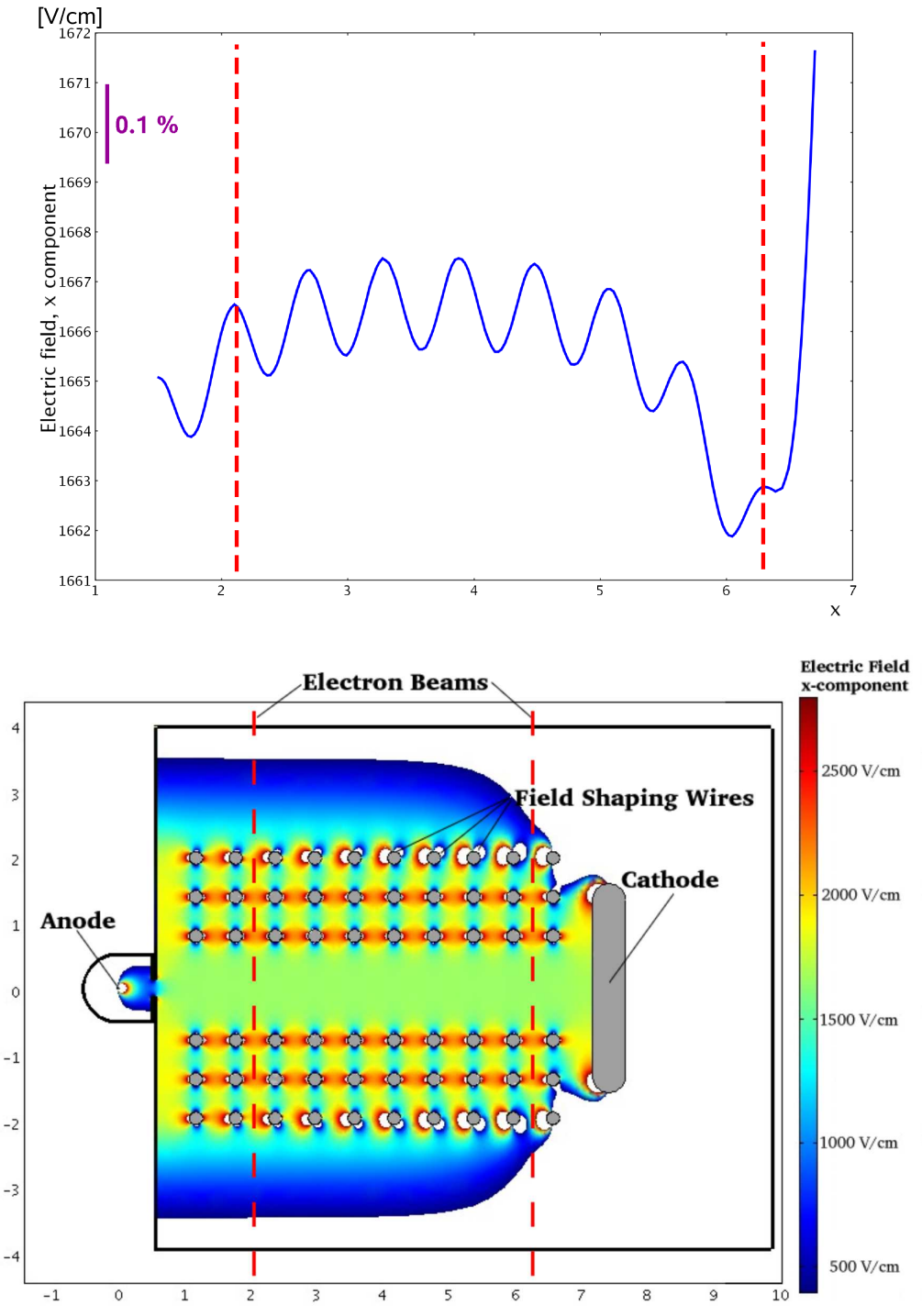

Figure 6.5: *(top) The electric field in the prototype along the central drift line ($y = 0$) computed with COMSOL Multiphysics in a 2D simulation. (bottom) The x-component of the electric field in the $x - y$-plane computed with COMSOL Multiphysics.*

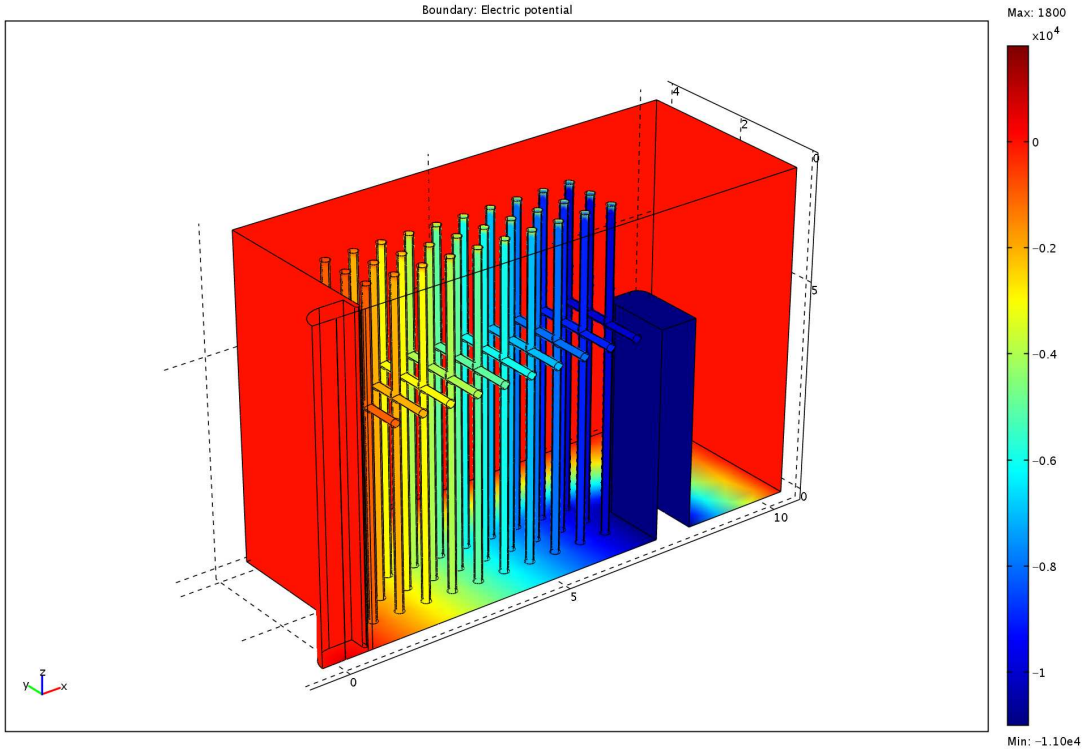

Figure 6.6: *One quarter of the VdC simulated with COMSOL Multiphysics in 3D. The colours represent the electric potential V from* red = 0V *to* blue = -11 000V. *The sensitive area is situated along the egde at y=z=0 that represents the central drift line.*

Figure 6.5 shows a coloured surface plot of the x-component of the electric field.

6.2.3 3D-Simulations with COMSOL Multiphysics

The 2D simulations for the VdC assume an infinite length in z-direction (along the field shaping electrodes). In reality, however, the length is finite. Since this length has been chosen before the 3D simulations were in place, it is only possible to check if the value taken (154 mm) is sufficient. Systematic studies to determine the best value (as small as possible to have a small gas volume, but sufficient to prevent electric field components in z-direction) are not done yet. To minimise the effect of the grounded walls on the field in the drift region, the field shaping electrodes are connected by small pieces of the 2 mm tubes. Thus, the electrodes surround the sensitive area completely.

For the simulation in 3D, the symmetries of the chamber with respect to the $x-y-$plane and to the $x-z-$plane were used so that only a quarter of the chamber has to be simulated to save computing time. Still, the mesh (see section 6.1.2) had to be refined locally in the areas around the lines where plots are made, to obtain a reasonable resolution. Figure 6.6 shows the simulated geometry.

The x-component of the electric field computed along the central drift line ($y = 0$ and $z = 0$) is similar to the results obtained from the 2D-simulations.

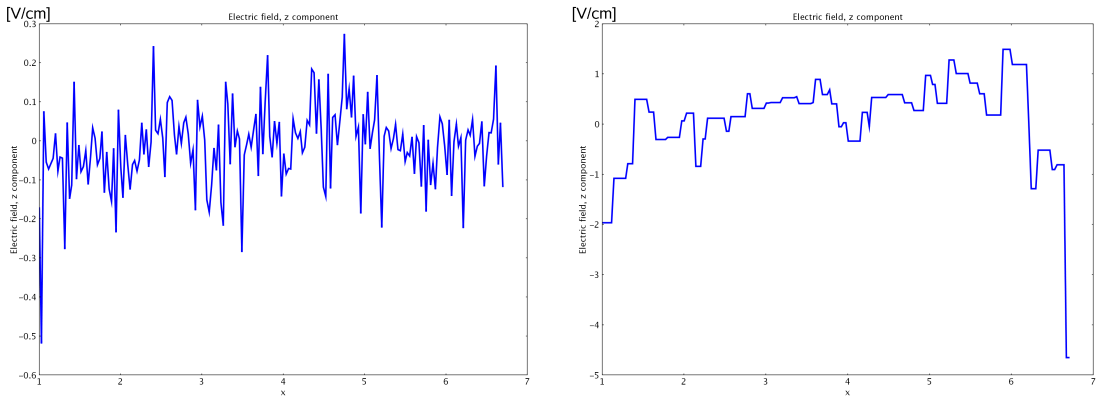

(a) (b)

Figure 6.7: *The z-component of the electric field at the borders of the sensitive region: (a) at $y = 1.5\,mm$ and $z = 0\,mm$ (b) at $z = 10\,mm$ and $y = 0\,mm$.*

Looking at the z-component of the electric field (Fig. 6.7) at the borders of the sensitive area, one can see that the deflection in z-direction can be neglected. The variations are due to the granularity of the mesh. Thus, a length of 154 mm in z-direction is sufficient for the drift volume. In further simulations, it has been shown that the effects of the chamber length can also be neglected without the interconnections: for the chosen length of 154 mm, the interconnections do neither improve nor disturb the electric field in the sensitive area.

6.2.4 Improved Simulation with Garfield

The reason for the different results of Garfield and COMSOL Multiphysics is the thin wire approximation done by Garfield (see section 6.1.1). The wire diameters have to be small compared to the inter-wire distances, which is not the case for the field shaping electrodes which have 2 mm diameter and are spaced by 6 mm distance. This problem can be solved by an improved simulation where the field electrodes are not simulated by one wire but rather by a circle of multiple thin wires. Figure 6.8 shows an enlarged cutout of the chamber. In the upper plot (old simulation), one can see the equipotential lines running through the wires, which is obviously wrong. In the lower plot (improved simulation), they are bent around the wires as they should.

With those changes implemented in the simulation the wiggles of the electric field are verified by Garfield. The field shape is now similar to the field calculated by COMSOL Multiphysics and can be optimised easily by adjusting s_1 and s_2 (see in Fig. 6.9). The field homogeneity in the sensitive area is now

$$\frac{\Delta E}{E} \approx 0.1\% \quad \text{with} \tag{6.1}$$

$$s_1 = 5.76\,\text{mm} \tag{6.2}$$

$$s_2 = 5.85\,\text{mm}. \tag{6.3}$$

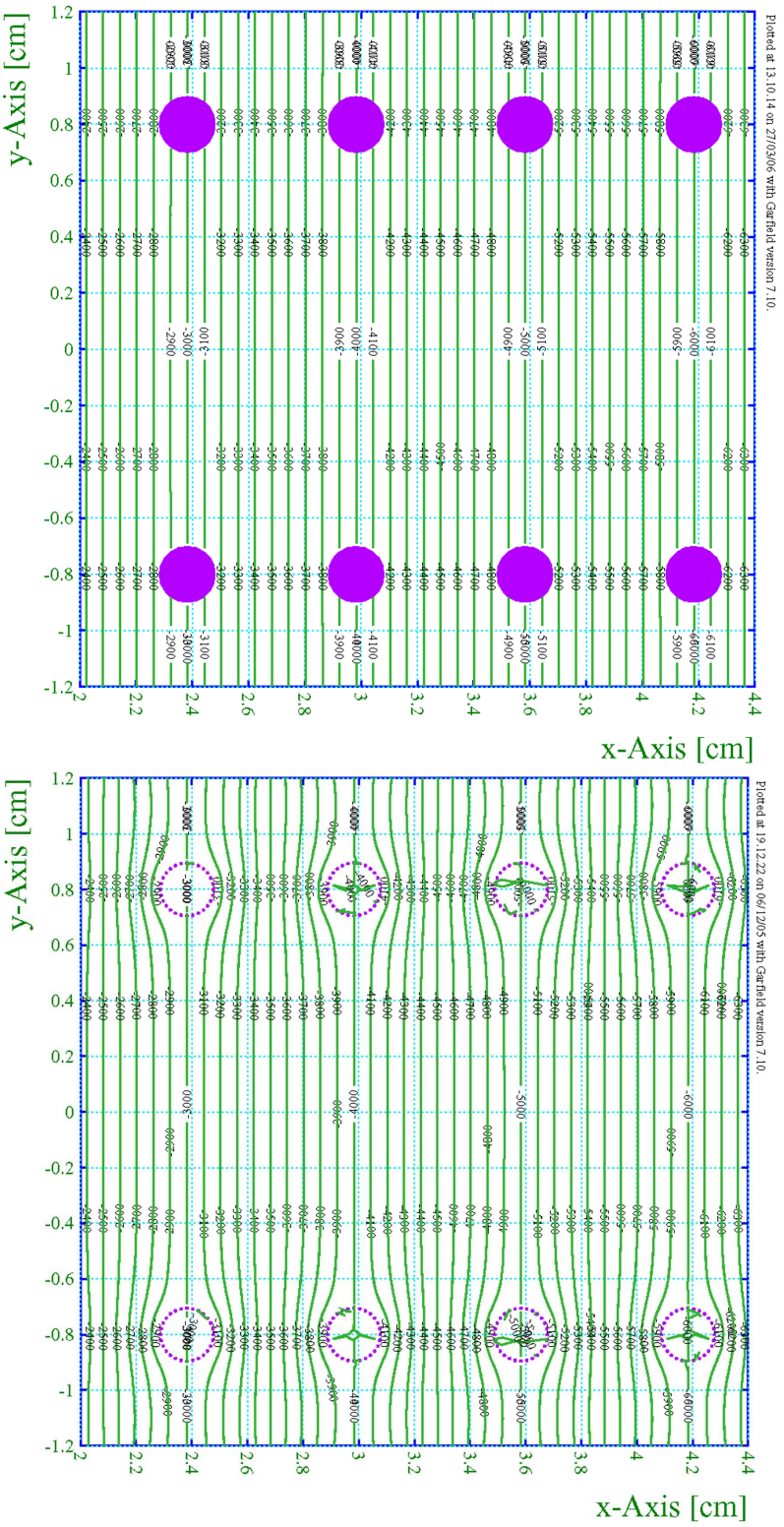

Figure 6.8: *In the first simulation (top) the equipotential lines go through the field electrodes, which is obviously wrong. In the improved simulation (bottom) each wire is simulated by a circle of multiple wires with the same potential, so that the equipotential lines are bent correctly around the electrodes.*

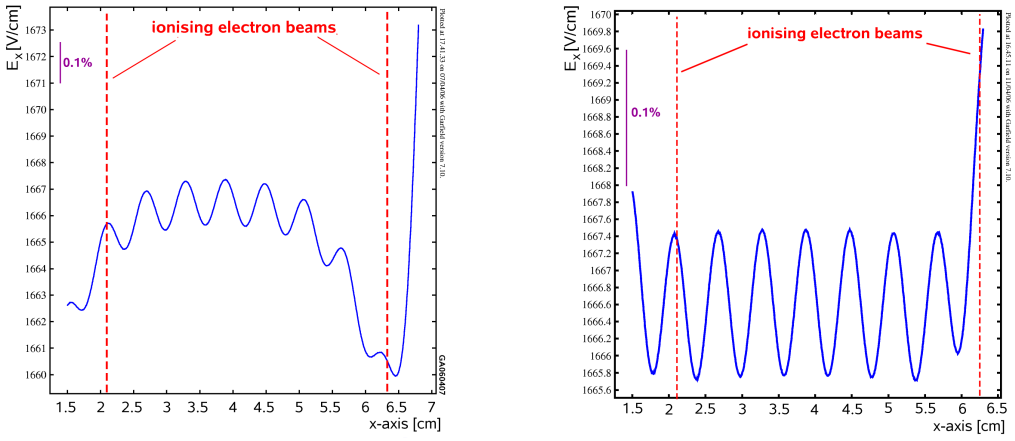

Figure 6.9: *(a) The electric field in the prototype along the central drift line when using the improved simulation. (b) After adjusting s_1 and s_2, the overall field shape becomes more homogeneous, while the wiggles cannot be eliminated.*

6.3 Impact of Tolerances

The VdC geometry is calculated with a precision of 10 μm, while the construction accuracy is approximately 40 μm [39]. Therefore it must be checked, how stable the electric field is when variations of the positions of this order of magnitude are assumed

Position of field electrodes: In figure 6.10 the position of a field shaping electrode in the inner layer is shifted by 50 μm in x-direction. One can see, that the field is very vulnerable to inaccuracies of the electrode position. Therefore, greatest efforts have to be made to place the field electrodes as exactly as possible.

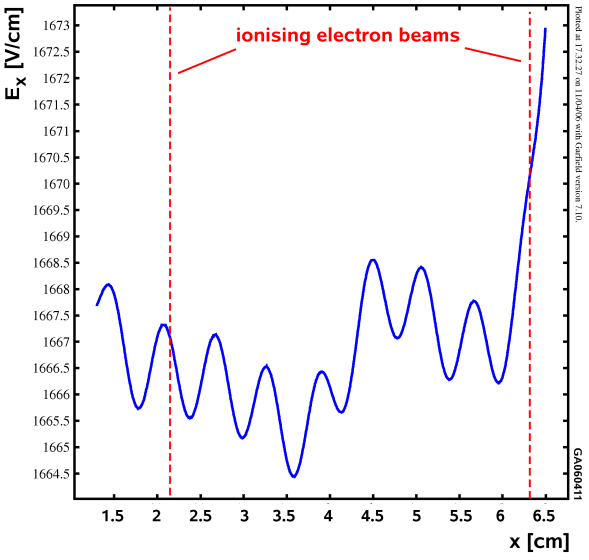

Figure 6.10: *The effect on the electric field when shifting the electrode at x=4.176 cm and y=0.800 cm by 50 μm in x-direction.*

Resistor Values: Figure 6.11 demonstrates the effect of an imprecise resistor. To study this, the value of the resistor between the 1st and 2nd row (at $x_1 = 6.6\,\text{cm}$ and $x_2 = 6.0\,\text{cm}$) of the field electrodes was increased by $10\,\text{k}\Omega$ from $18\,\text{M}\Omega$ to $18.01\,\text{M}\Omega$. The field near the cathode is slightly increased. The accuracy that can be achieved by the procedure described in chapter 7.4.1 is about $1\,\text{k}\Omega$. Simulations with fluctuations of this order of magnitude do not lead to a visible effect.

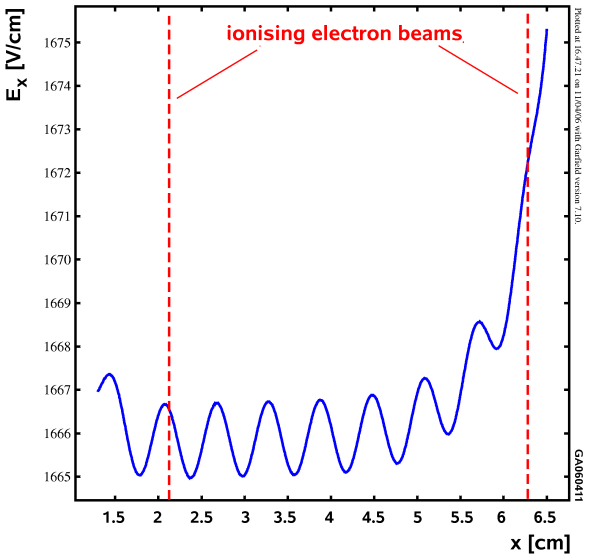

Figure 6.11: *The effect on the electric field when increasing the value of the resistor between the 1th and 2nd row (at $x_1 = 6.6\,cm$ and $x_2 = 6.0\,cm$) of the field electrodes by $10\,k\Omega$.*

6.4 Other Systematic Errors

There are other effects which may disturb the electric field or interfere on the path of the ionising electron beams, some of which will be discussed in this chapter.

Space Charges in the Drift Volume

Free electrons and ions originating from the ionising electron beams and from the charge multiplication are always present in the chamber. Being charged they influence the electric field. All these free charges are generated in the same plane, so that their effect can be discussed in a 2D geometry.

Electrons from the sources will reach the drift volume with a rate of 1085 Hz per source (see section 5.2), leading to an average time of $920\,\mu\text{s}$ between two ionisations. The electrons drift with a velocity of roughly $55\,\mu\text{m/ns}$ in direction of the anode, thus reaching the chamber wall after $1.0\,\mu\text{s}$ from the far and accordingly $0.3\,\mu\text{s}$ from the near source. This means, that the drifting electrons from one event do not disturb the next ones.

On the contrary, the ions drift 1000 times slower so they stay much longer in the drift volume, forming a positively charged rectangular plane. With a drift velocity of roughly $0.05\,\mu\text{m/ns}$ the distance between two ionisation lines is about $d_x = 4\,\text{cm}$ in x-direction

(drift-direction). In y-direction (direction of the ionising electrons), there are 100 electron-ion-pairs per cm leading to an average distance of $d_y = 0.01\,\mathrm{cm}$ between the ions. The resulting charge density of the ions originating from each of the β-sources is $\rho = 25\,\mathrm{e/cm^2}$.

Furthermore, some ions resulting from the charge multiplication will drift back to the drift volume. The assumed gain factor is 50 000, but those ions are emitted nearly symmetrically around the anode wire (see Fig. 4.4), so that only a small part of them reaches the drift volume. The slit to the drift volume is situated at a distance of $r_a = 0.5\,\mathrm{cm}$ and has a width of 0.25 cm, leading to

$$\frac{0.25\,\mathrm{mm}}{2\pi \cdot 0.5\,\mathrm{mm}} \cdot 50\,000 = \frac{1}{4\pi} \cdot 50\,000 \approx 4\,000 \tag{6.4}$$

That means, that for one electron reaching the detection volume, 4 000 ions drift back into the drift volume, leading to a mean distance between the ions of 0.001 cm and a charge density of 100 000 $\mathrm{e/cm^2}$.

A homogeneously charged plane ($0 < x < a$, $-b/2 < y < b/2$) generates the following electric field [$r^2 = (x' - x)^2 + (y')^2$]:

$$\begin{aligned} E(x) &= \frac{\rho}{4\pi\epsilon_0} \cdot \left[\int_{-b/2}^{b/2} \int_0^a dy'\, dx'\, \frac{x' - x}{r^3} \right] \\ &= \frac{\rho}{4\pi\epsilon_0} \cdot \left[2 \ln \left(\frac{b/2 + \sqrt{x^2 + (b/2)^2}}{b/2 + \sqrt{(a-x)^2 + (b/2)^2}} \cdot \frac{|a - x|}{|x|} \right) \right] \end{aligned} \tag{6.5}$$

This function diverges for $x \to a$ and $x \to 0$, but for distances smaller than the distances between the ions the estimation of a homogeneous charged plane does not apply any more. Furthermore, the change-over from one of the planes to the next is in reality not sharp. In a distance of 0.001 cm (the distance between the ions drifting away from the anode wire in y-direction) from the ends of the planes, the calculated electric field does not exceed values of $10^{-5}\,\mathrm{V/cm}$, which is negligible with respect to the drift field of $\approx 2 \cdot 10^3\,\mathrm{V/cm}$.

Deflection of the Ionising Electron Beams

The β^- traversing the drift volume are deflected perpendicular to their momentum by the drift field. For calculating the deflection, the maximum possible drift field of $E_{el} = 2.5\,\mathrm{kV/cm}$ and an electron with the comperatively low kinetic energy of $E_{kin} = 1.5\,\mathrm{MeV}$ shall be considered. The momentum p and the relativistic β and γ-factors for the electron are calculated to:

$$p = \sqrt{(E_{kin} + E_0)^2 - E_0^2} = 1.945\,MeV \tag{6.6}$$

$$\beta = \sqrt{1 - \frac{E_0^2}{E^2}} = 0.967 \tag{6.7}$$

$$\gamma = \frac{1}{\sqrt{1 - \beta^2}} = 3.935 \tag{6.8}$$

The electron reaches the collimator at the opposite wall of the chamber ($d = 72\,\mathrm{mm}$) after a time

$$t = \frac{d}{\beta c} = 0.25\,\mathrm{ns} \tag{6.9}$$

Relativistic effects must be taken into account for calculating the deflection Δx. Following reference [40], an electron traversing a homogeneous electric field perpendicular to the field lines is deflected after a time t in direction of the field by

$$\begin{aligned} \Delta x &= \frac{1}{qE_{el}} \cdot \left(\sqrt{m^2c^4 + c^2q^2E_{el}^2t^2 + m^2c^4\gamma_0^2\beta_0^2} - \sqrt{m^2c^4 + m^2c^4\gamma_0^2\beta_0^2} \right) && (6.10) \\ &= 345\mu\mathrm{m} && (6.11) \end{aligned}$$

where $\gamma_0 = \gamma(t = 0)$ and $\beta_0 = \beta(t = 0)$. The electron mass is $m_e = 9.108 \cdot 10^{-31}\,\mathrm{kg}$ and the charge $q = -e = -1.602 \cdot 10^{-19}\,\mathrm{C}$.

This deflection affects both electron beams in the same way so that there will be no error in the drift velocity measurement. However, the deflection reduces the number of electrons which pass through the second collimator.

Chapter 7

Construction of the VdC

This chapter describes the construction of the prototype of the VdC. For the realisation of the chamber with the parameters resulting from the simulation and given by Tab. 6.1, the following aspects needed to be considered:

- Gas tightness: To avoid impurities the VdC has to be leakproof. This goal is achieved by O-ring seals and/or gluing.
- Electric strength: Because of the very high voltage needed at the cathode (up to 15 kV), a great effort has been made to avoid discharges inside the small volume of the VdC. It is impossible to measure the signals of a few hundred μV from the drift electrons at the anode wire while high voltage discharges occur inside the chamber, because discharges induce much larger signals on the anode wire than the drifting electrons.
- Precision: For producing a highly precise electric field, geometrical chamber dimensions and resistor values have to be as accurate as possible.

7.1 The Components

The mechanical components of the VdC are produced on CNC[1] milling machines to achieve the highest possible precision. For maintenance reasons it was decided to make all of the components removable. The cathode side (Fig. 7.1) and the detection volume (Fig. 7.2) can be removed without disassembling the whole chamber. Figure 7.3 shows the body of the VdC with cathode and detection volume removed.

The chamber body is made of aluminum and is grounded in order to shield the drift field from external influences. To achieve a high field strength, the inner walls are covered with Araldite. The electrodes are fixated in the aluminum walls with small insulators made of Polyetheretherkethone (PEEK). During the high voltage tests it turned out that PEEK carbonises very fast: After a few discharges along the surface, it becomes conductive and thus does not insulate the electrodes from the grounded walls anymore. Therefore, plates of Polyamid (PA6) are inserted in the top and bottom walls of the chamber (Fig. 7.4) providing a higher protection against sparking.

[1] Computerised Numerical Control

Due to the 2 mm diameter of the field shaping electrodes, a spacing of at least 6 mm between the different rows of field shaping electrodes is needed for fixation and isolation.

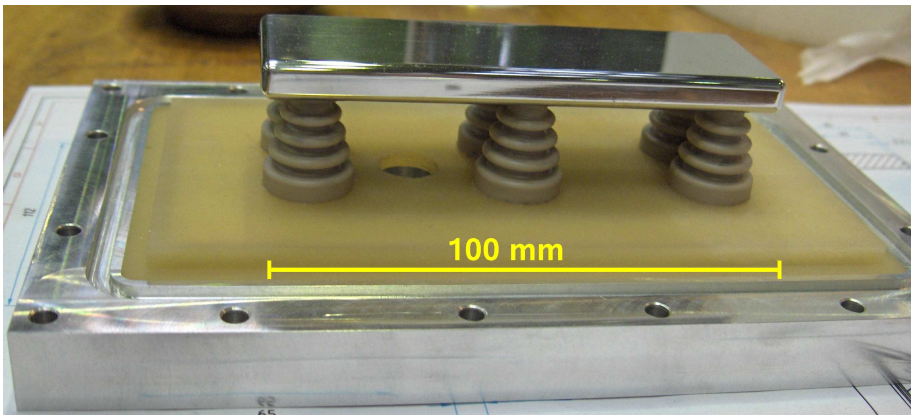

Figure 7.1: *The cathode. It is positioned on 6 insulator feet. A conductor through a further insulator (not mounted here) connects the cathode to high voltage.*

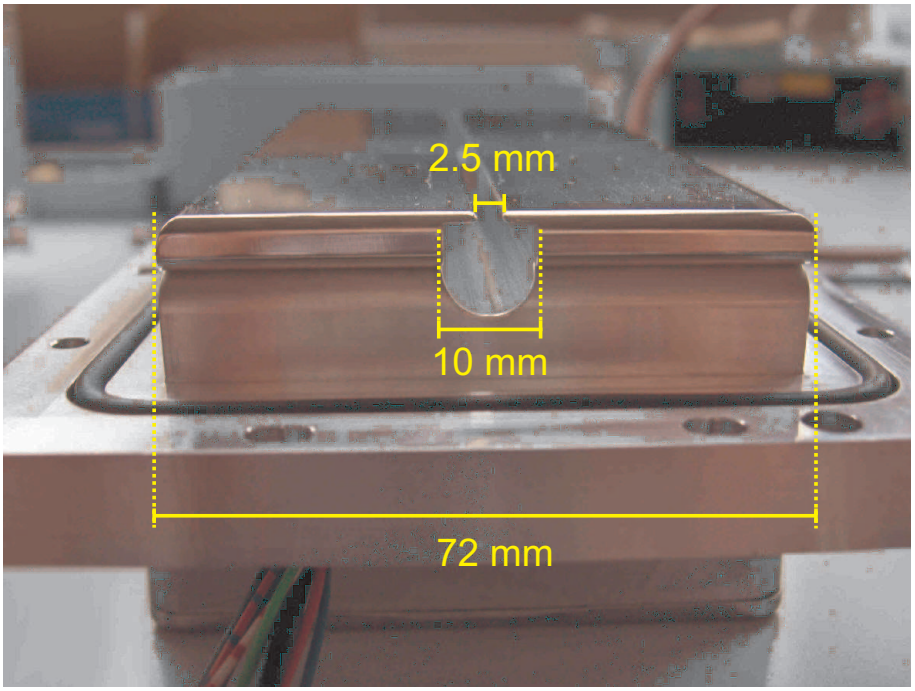

Figure 7.2: *The detection volume with the 2.5 mm wide collimator slit at the top.*

The electronics part of the chamber is also made removable. The resistor chain and the voltage supply for the anode wire are placed in boxes made of PEEK that can easily be unplugged from the chamber. For reasons of electric strength, they are sealed with Araldite.

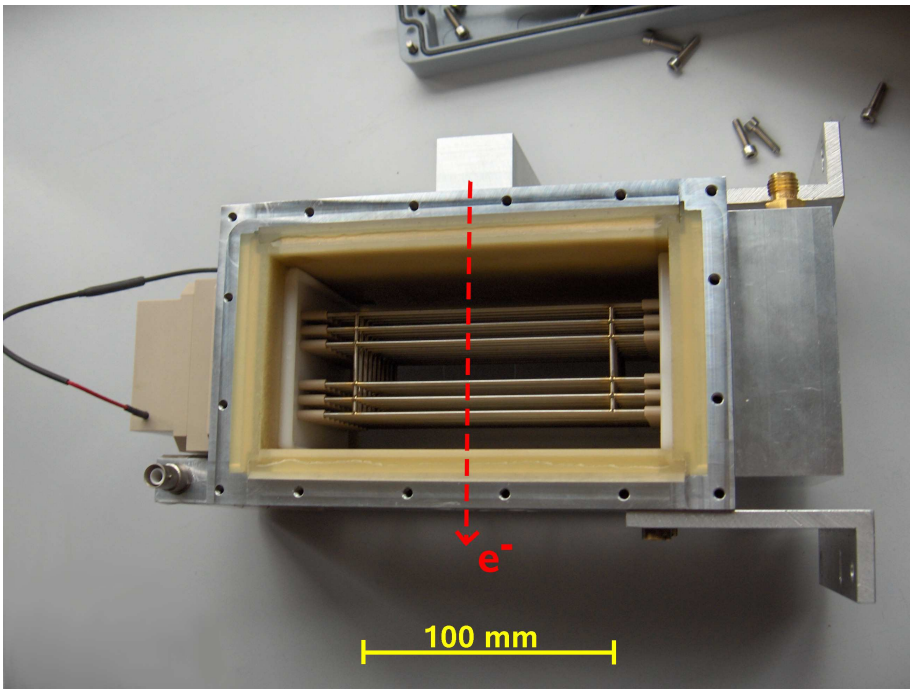

Figure 7.3: *A look into the chamber body from the cathode side. The cover holding the cathode is removed.*

7.2 The Field Shaping Electrodes

The field shaping electrodes are small tubes made of stainless steel (Inconel 600) with an outer diameter of 2 mm. As can be seen in figures 7.3 and 7.4, there are interconnections near the ends of the tubes. Those interconnections serve several purposes:

- Shielding of the drift field against the grounded walls. With the interconnections, the drift field is surrounded by electrodes with the right potential.
- Electric connection between field shaping wires being at the same potential: Only one of the six electrodes with the same potential must be directly connected to the resistor chain.
- Mechanical precision: The distance between the field electrodes is fixated by the interconnections.

The interconnections are welded on the field electrodes with a laser, using a special fixture guaranteing, that the field electrodes keep the distance of 6 mm.

7.3 Electric Strength

The most secure solution to avoid sparking is to work with large distances between the potentials. This is not the best solution for the VdC since one chamber has to monitor the gas from multiple muon chambers one after another, which means that it is necesary to change the gas inside the VdC as quickly. Therefore, a small gas volume is advantageous.

Figure 7.4: *The field shaping electrodes fixated in a Polyamid-plate that is inserted in the chamber walls. The electrodes are additionally protected by small insulators made of PEEK.*

For this reason, the walls of the chamber which are grounded for electrostatic shielding are covered with a 4 mm layer of Araldite. The cathode, that has to hold the highest voltage, is screwed to six insulator feet (made of PEEK, Fig. 7.1). A seventh foot contains the high voltage supply for the cathode. To allow disassembling of the chamber for maintenance, the edges of the six walls are not completely glued with Araldite: a small slit remains open. In the first high voltage tests, this turned out to be a problem, because electric discharges occured between the electrodes and the edges. Therefore, the distance to the grounded walls is extended by increasing the thickness of the Araldite layer so that the slit is bent. Fig. 7.5 a) shows the orginal version with a straight slit, while the slit in 7.5 b) is much longer.

7.4 High Voltage Supply

7.4.1 Cathode and Field Electrodes

Fig. 7.6 shows a circuit diagram of the high voltage supply for the cathode and the field shaping electrodes. The VdC is designed to stand cathode voltages up to 15 kV. To ensure that the cathode voltage is stable, there are capacitors that bleed off small fluctuations in the supply voltage.

The resistors in the resistor chain (see section 5.1) are not soldered directly on the field shaping electrodes, but on extensions that can be removed easily for chamber maintenance. A special module was built which is just plugged onto the chamber. The resistors have values of approximately 20 MΩ to minimize the current. Each 20 MΩ resistor is made up

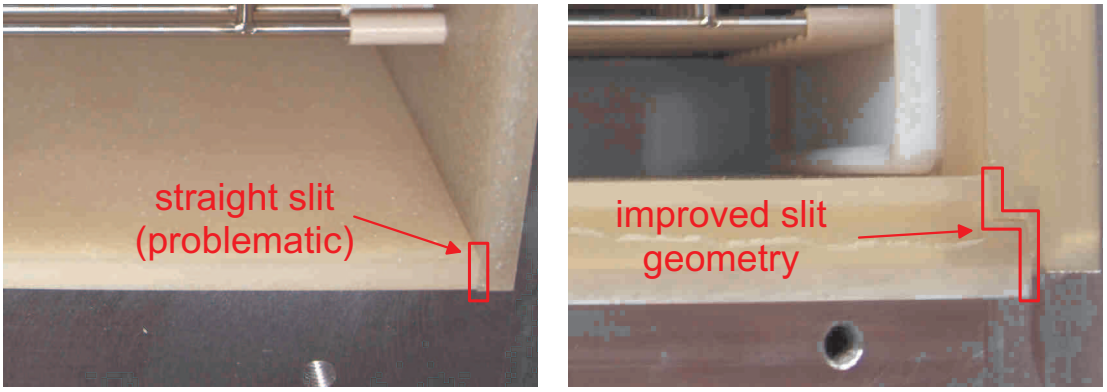

(a) (b)

Figure 7.5: *The Araldite layer at the edges of the VdC walls. In the first tests there were discharges through the slits to the edges (a) of the chamber. After elongation of the slits from the electrodes to the grounded walls by a thicker Araldite layer and bending (b), the sparking vanished.*

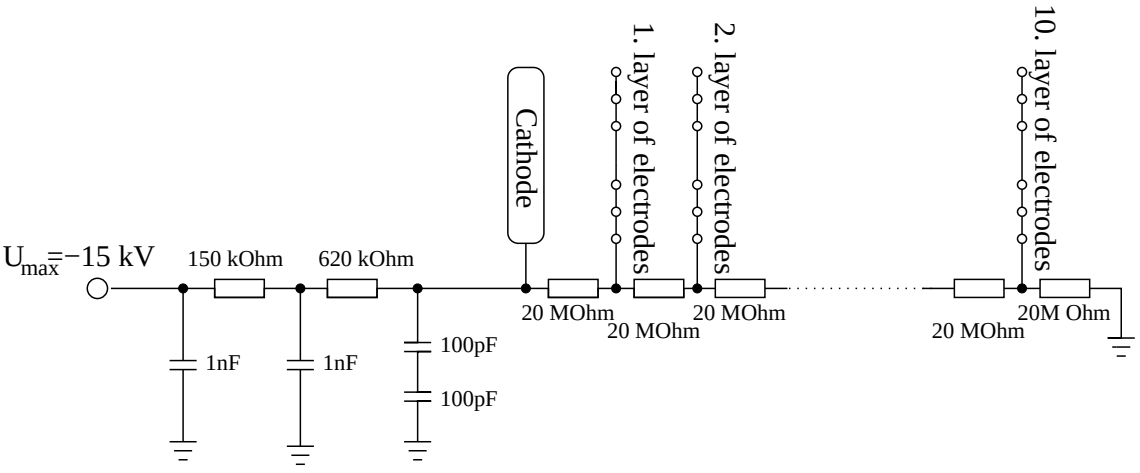

Figure 7.6: *The high voltage supply for the cathode and the field electrodes. Small fluctuations in the supply voltage are bleed off via the capacitors.*

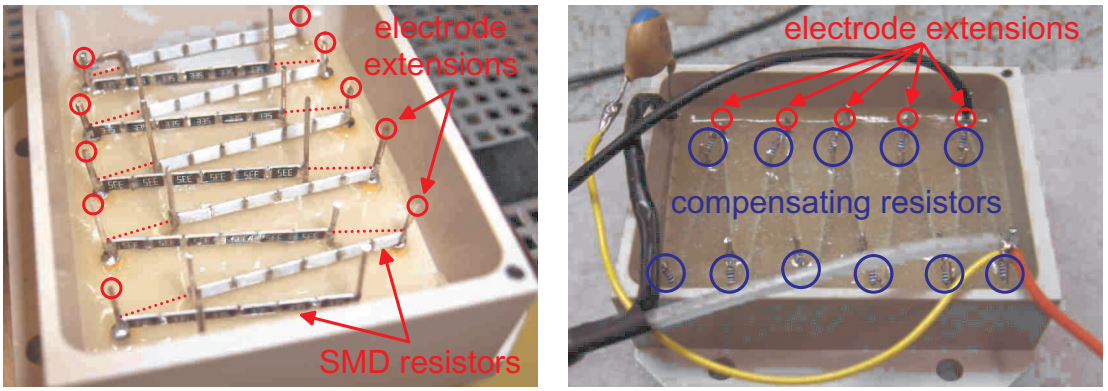

(a) (b)

Figure 7.7: *(a) The 20 MΩ-resistors are connected to the extensions of the field shaping electrodes. The dashed red lines indicate the places where the compensating resistors are soldered on the resistors. (b) After sealing the resistors with Araldite, the compensating resistors are added to adjust the resistor values.*

of six 3.3 MΩ SMD[2]-resistors. For $V_{max} = 15\,\text{kV}$ and $R_{total} = 11 \cdot 20\,\text{M}\Omega = 220\,\text{M}\Omega$, the following current and electrical power can be calculated:

$$I_{max} = \frac{U}{R_{total}} = 68\,\mu\text{A} \tag{7.1}$$

$$\Rightarrow P_{max} = U \cdot I = 1.02\,\text{W} \tag{7.2}$$

Working with 20 MΩ-resistors, two major problems must be solved:

- A precise measurement of the absolute values of highly resistive resistors is very difficult.
- To ensure electric strength, the resistors have to be sealed by Araldite.Doe to such high resistor values the conductivity of the insulator is not negligible.

The first problem turned out to be easily solved: it is not necessary to know the exact resistor value, it is much more important that all resistors have the same value. Measurements of the equality of resistors can be done very precisely with a bridge circuit. The only disadvantage is that the fine tuning of the electric field cannot be done by varying the resistor values and is therefore to be done by varying the distance between the electrodes.

The small differences in the resistor values and the impact of the insulator is corrected by additional compensating resistors. The 20 MΩ-resistors are soldered on the extensions of the field shaping electrodes, with one end left open (Fig. 7.7) and then sealed with Araldite. In the next step, the differences of the resistors are determined with a Wheatstone Bridge and compensated with additional resistors of about 10-20 kΩ.

The compensating resistors are sealed as well. Compared to their resistance the conductivity of the insulator can be neglected. Using this procedure, an accuracy of better than 1 kΩ [41] can be achieved. This accuracy is limited by the voltmeter used in the Wheatstone Bridge.

[2]Surface Mounted Device

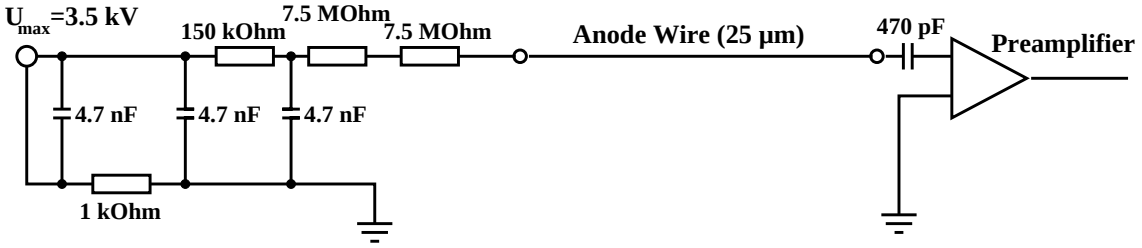

Figure 7.8: *Circuit diagram for the anode [41]. The capacitors in the HV supply filter out small AC-parts of the supply voltage. The anode wire is connected to a preamplifier via a further capacitor that lets the signals - which are AC-components - pass.*

7.4.2 Anode

The anode voltage supply circuit (Fig. 7.8) is similar to the one for the cathode: capacitors filter out remaining AC-components of the voltage supply. The preamplifier at the other end of the anode wire (or signal wire) has to amplify signals that have 6 orders of magnitude lower voltage than the HV supply. Therefore, a 470 pF capacitor that keeps the direct-current away from the preamplifier, is placed between signal wire and preamplifier, so that only the small ($\sim 200\,\mu$V) voltage fluctuations resulting from the drift electrons can be seen by the peamplifier. On the HV end of the signal wire, there are two 7.5 MΩ resistors that make sure, that the signals take the way with the lower resistance to the preamplifier, where they are amplificated by a factor 100. The preamplifier - produced for the muon system of the UA1 detector[3] - amplifies only the AC component of the applied voltage and accepts pulses with a voltage of more than 100 μV. The maximum output voltage is limited to 3 V. The analog amplified pulse is then sent to a comparator with an adjustable threshold, where a digital signal is generated [41].

[3]Experiment at the former $p^+ - p^-$ collider SPS (Super Proton Sychrotron) at CERN

Chapter 8

Commissioning and First Tests

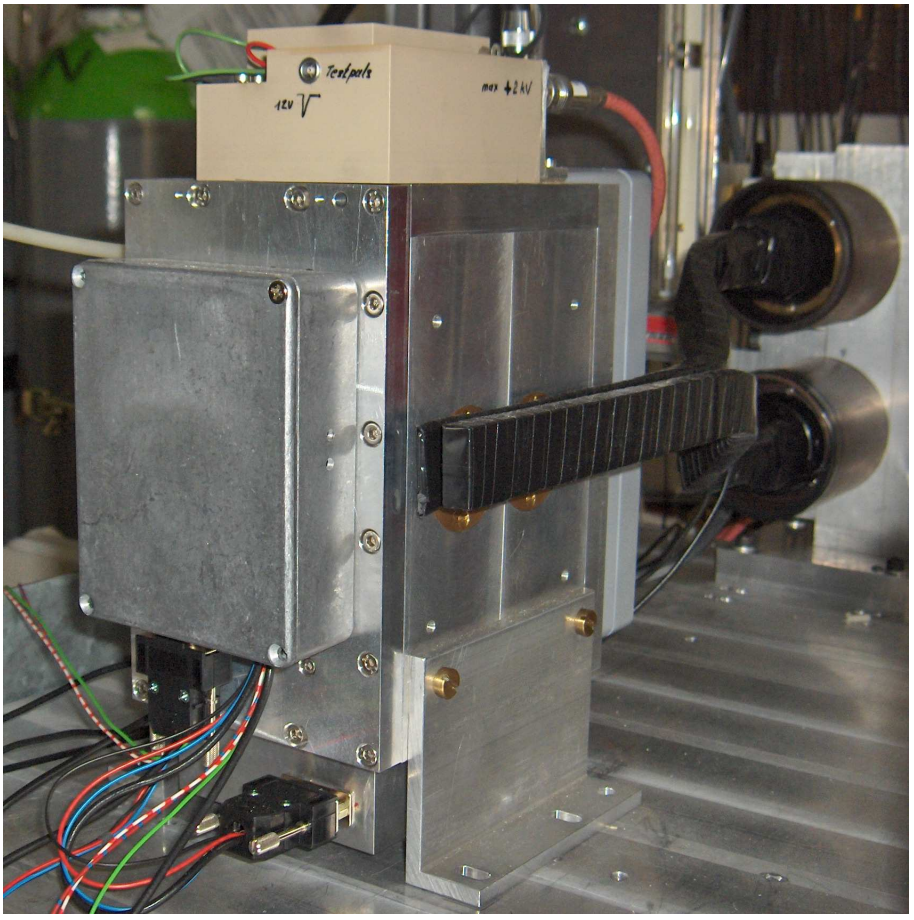

Figure 8.1: *The fully mounted VdC at the teststand in Aachen. On the right, one can see the two scintillators and the photomultipliers. The box on the front plate contains readout electronics.*

The design of the data acquisition used for the prototype chamber in Aachen is in principle the same as it will be used later at CMS although some details will be solved more elegantly. Electronic units (discriminators, coincidences,...) will be integrated in the chamber, but will work following the same principle. The TDC is already the final one, while the software used for the first tests is still in an initial state.

8.1 Calibration of the Trigger

Fig. 8.2 illustrates the used electronic units and the pulse shape at the different stages. The PMTs produce negative signals (1) that are approximately 20 ns long. These pulses are sent to discriminators, where they are translated into NIM signals (2). The signal from PMT2 is widened ($\sim 50-100$ ns), while the pulse from PMT1 is made rather short (~ 10 ns) and is delayed (3) by a few ns before it is sent to the coincidence unit. The advantage of this procedure is, that the starting point for time measurement is always given by the same scintillator so that time fluctuations of the other signal do not disturb the measurement. In the case of the VdC, the signal from PMT2 is taken as reference signal because the thick scintillator SC2 is supposed to produce more light so that the signal should be more stable in time. Time fluctuations appear in the order of a few ns. After the coincidence, the signal (4) has to be translated from NIM to differential ECL, because the TDC accepts only differential ECL, while all other units are NIM devices. The TDC converts the ECL signals to digital information, that can be read and analysed by a computer.

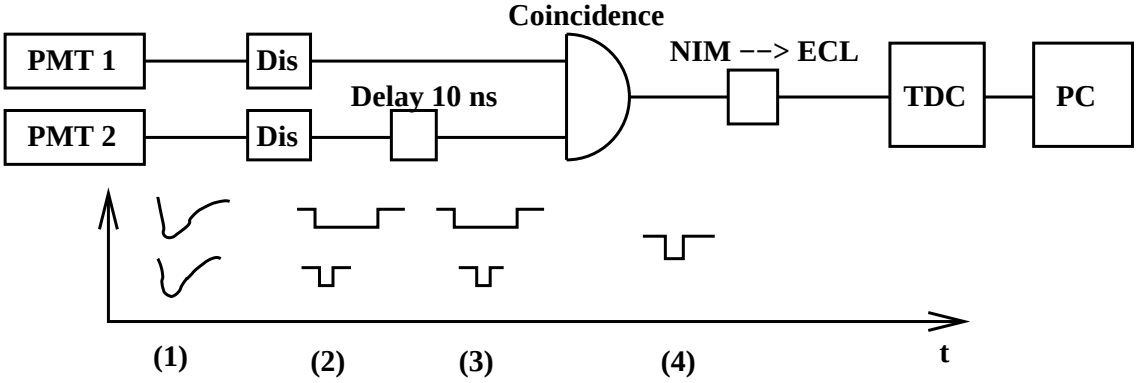

Figure 8.2: *The signals from the two PMTs are first sent to discriminators, where the signal from PMT1 is translated into a long ($\sim 50-100$ ns) NIM-pulse, the signal from PMT2 in a short (~ 10 ns) one. The latter is delayed by 10 ns so that it arrives always later at the coincidence than the PMT1 signal. Thus, the start of the coincidence signal is always defined by the pulse from PMT2.*

As explained in section 5.3.2, the photomultipliers need a high voltage supply. The optimal high voltage value needs to be adjusted for every PMT. With a too high voltage, the PMTs produce too much noise and the probability of accidental coincidences increases. On the other hand, a too low voltage leads to a loss of real signals because the amplification is not large enough. Another point is the lifetime of the photomultiplier tubes, that is strongly correlated to the applied voltage. The PMTs are adjusted by measuring the dependency of the coincidence rate on the high voltage using the following steps:

1. The voltage is set to a value, where the PMTs are known to work (can be checked for example by measuring the coincidence rates with and without the ^{90}Sr sources). The discriminator thresholds[1] should be at the lowest possible level.

[1] The discriminator threshold defines the minimum pulse height. A smaller pulse will not be accepted by the discriminator.

2. The high voltage of one PMT is varied to find the plateau in the coincidence rates. The voltage is set to the beginning of the plateau.

3. The same is done with the second PMT.

4. Steps 2 and 3 are repeated until the values do not change anymore.

Having found the correct high voltage values the discriminator thresholds can be carefully increased until the thresholds reach values where real signals are cut away, leading to a decreasing coincidence rate.

With this setup, the trigger accepts as many events as possible. Now, it is necessary to check the signal to noise ratio. This is done by comparing the coincidence rates with and without ^{90}Sr sources. Depending on the needs, one can try to improve the signal to noise ratio by increasing the discriminator threshold or decreasing the PMT voltage. However, this will lead to a loss of real events.

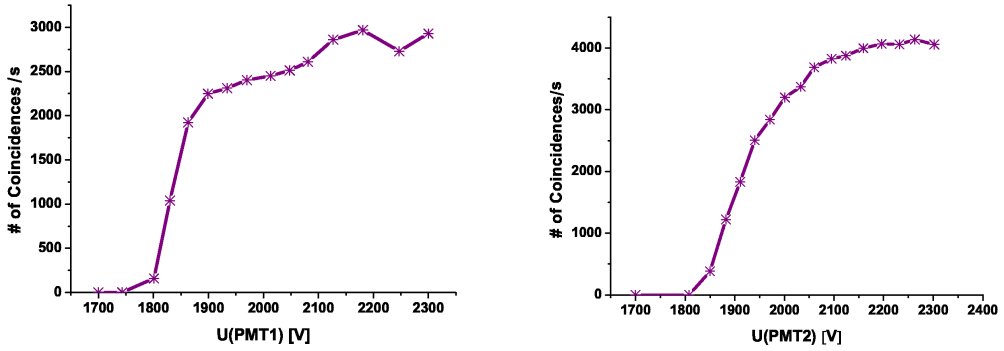

(a) (b)

Figure 8.3: *The coincidence rate as a function of the voltages of PMT1 (a) and PMT2 (b) with the ^{90}Sr sources directly in front of the thin scintillator SC1.*

Figure 8.3 shows the dependency of the trigger rates on the photomultiplier voltages. For PMT2, the region of saturation is reached at a value of about 2100 V. For PMT1, the determination of the optimal value was rather difficult: The gradient of the curve for PMT1 decreases a bit at 1900 V, but still does not reach saturation. To avoid loosing real signals, it was decided to run PMT1 with 2100 V, too. The coincidence noise rate with those voltages is about 1 Hz which is tolerable when having a coincidence rate of about 20 Hz while the radioactive sources are installed inside the VdC.

The coincidence rate of about 20 Hz is far below the expected value (see section 5.2). In tests concerning the scintillator efficiency the coincidence rates showed a strange behaviour when varying the position of a radioactive source. One expects increasing rates when decreasing the distance to the PMT because of a reduced absorption loss, but this behaviour was not observed. A reason for this might be the light proof wrapping of the scintillators or the used scintillator material which showed - especially in the thin scintillator - small cracks. Tests with a new wrapping technique lead to better results, but still the coincidence rate is much lower than expected.

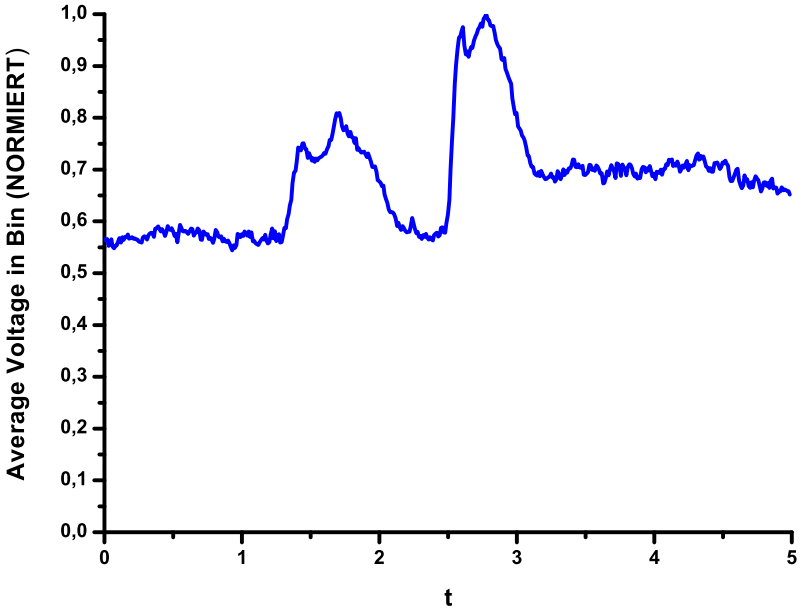

Figure 8.4: *The histogram taken with the oscilloscope in average mode. The bin width is 0.01 µs.*

8.2 Tuning of the Chamber Signal

As described in section 7.4.2, the signal from the drifting electrons on the anode wire is separated from the DC high voltage by a capacitor and sent to a preamplifier (Fig. 7.8). The amplified signal is translated into a digital pulse by a comparator with an adjustable threshold. This threshold and the anode voltage are parameters that must be adjusted similarly to the trigger signals. When using a too low anode voltage, the electric field around the wire is not strong enough to allow charge multiplication, a too high value leads whereas to continuous discharges making measurements impossible.

With a diameter of 25 µm for the anode wire, charge multiplication in Ar/CO_2 should occur at voltages of about 1.6 kV [41]. This value is determined from experiences with the muon drift tube chambers and other experiments. Surprisingly, much higher voltages are needed to obtain measurable signals. Furthermore, the charge multiplication does not start always at the same value: the needed voltage fluctuates between 2.0 kV and 2.7 kV. After replugging the voltage supply to the anode wire the behavior improved. The reason might be a bad contact, but systematic studies on that topic have to be done in order to understand these effects completely.

Due to those problems, it was not possible to determine the optimal value for the anode voltage and thus for the comparator threshold so that they have to be readjusted regularly.

8.3 Data Acquisition

When the first tests of the VdC took place, the final readout components were not available so that the data had to be taken with a digital oscilloscope. This data is the first to demonstrate, that the chamber works, although a detailed analysis is not possible. Later

data was taken with the muon DT cosmics DAQ[2] system of the III. Physicalische Institut, so that existing analysis tools could be used. Finally, data have been taken with the TDC that will be used later at CMS.

8.3.1 Oscilloscope

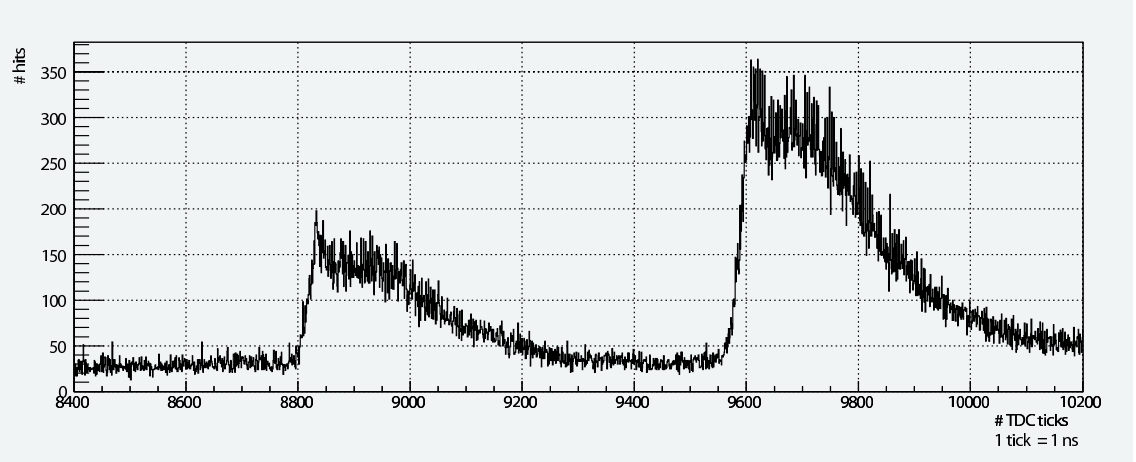

Figure 8.5: *The data taken with the cosmic muon DAQ.*

The used oscilloscope is a Tektronix TDS 644B [42], a four channel digital oscilloscope. This oscilloscope can be operated in the so called *average mode*, where the oscilloscope calculates for every time bin the average voltage over the measurement period. In this operation mode, the oscilloscope calculates the average over the entire pulse, not only the start time of the pulse (as it is done by the TDCs), resulting in a larger pulse width. One channel is used to trigger the oscilloscope with the signal taken directly from the coincidence unit. A second channel is used for the chamber signals. The resulting histogram with a bin width of 0.01 μs is shown in figure 8.4. One can clearly see the two peaks with a distance of roughly 1 μs, the double peak structure originates from afterpulses that occur in nearly every event. The reason for those afterpulses might be that the analog pulses from the anode are much longer than the discriminated pulses so that one analog pulse is translated into numerous NIM pulses.

8.3.2 Cosmics DAQ

The TDC of the cosmics DAQ, a Le Croy 2277A with a time resolution of 1 ns, continuously takes data. The trigger signal is delayed and when it reaches the TDC, the data that is already in the buffer will be read out. Therefore, two trigger signals are sent to the TDC: one in time to be recorded for a histogram and a second one delayed, that does the triggering. In operation with the muon test tubes chamber, every TDC channel corresponds to a cell of the muon chamber, two of those channels are used for the first trigger signal and for the chamber signal, respectively

The results are shown in Fig. 8.5. The distance of the two peaks is roughly 750 ns, which are in good agreement with the expected value. The rise of the peaks is already

[2] Data AcQuisition

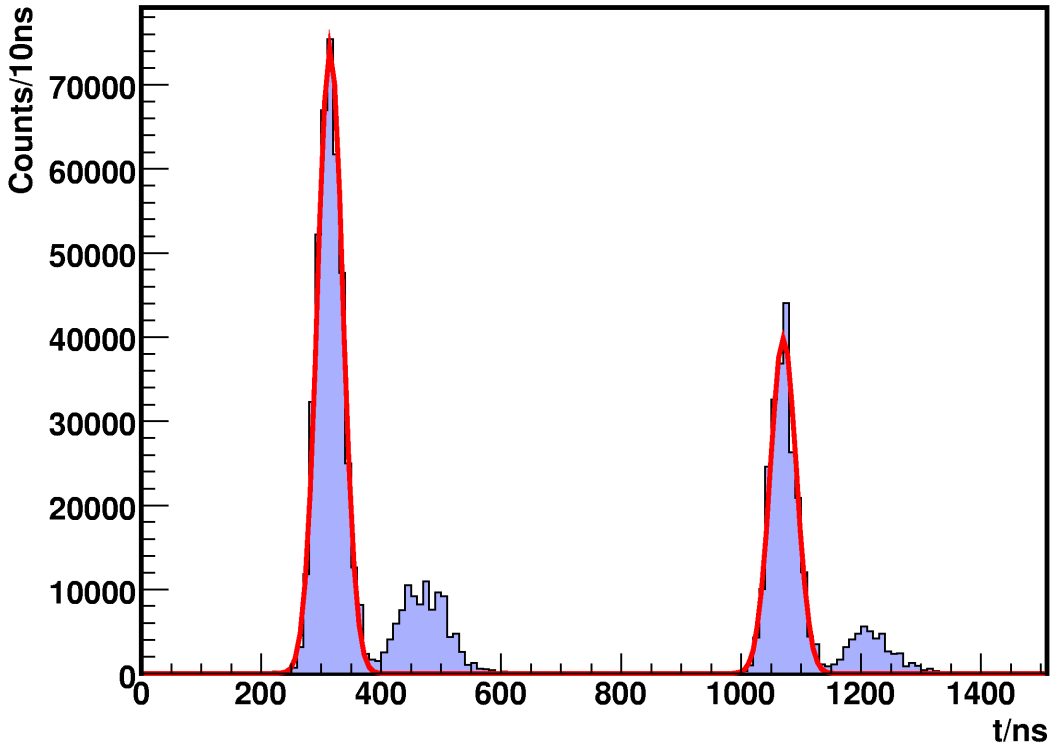

Figure 8.6: *First data recorded with the final readout.*

comparatively sharp, while the long tails result from afterpulses. With the existing DAQ tools, it is possible to analyse the pulse distribution more precisely. It is found that half of the events have eight or more pulses.

8.3.3 Final DAQ

The readout for the VdCs at CMS will be done by a CAEN V767 TDC [43] with a time resolution of 25/32 ns. This TDC accepts differential ECL signals and has 128 channels. Thus, one TDC is enough for to serve six chambers.

For the tests in Aachen, the TDC is operated in gate mode, which means that the trigger signal length is increased to certain value (in case of the VdC tests: 2 μs) and the TDC records all data that comes in during this time interval. For the VdC (low trigger rate and a small amount of data per event) the operation mode is not essential. For higher data rates, one would prefer the continuous mode. The software [44] - a LabVIEW code - is a preliminary version and is only used for data taking. The analysis of the data is done offline with Root [45].

8.4 The First Results

The first measurements using the final readout were done in March 2006. The data shown in Fig. 8.6 are from the first long term run ($\approx$ 10 h) with 783 731 events. The cathode

voltage was 12.2 kV, leading to a drift field of 1.85 kV/cm. For analysing the data, Gaussian distributions were fitted with Root [45] to the two big peaks. The small peaks result from afterpulses. As the TDC saves only the start of the pulse as time information, afterpulses can be suppressed by using a longer pulses. The time difference of the two peaks is:

$$\Delta t = 755.30 \pm 0.06^{stat}\,\text{ns} \tag{8.1}$$

With a drift distance of 4.2 cm, the measured drift velocity is:

$$v_d = 55.607 \pm 0.004^{stat}\,\frac{\mu\text{m}}{\text{ns}} \tag{8.2}$$

This is the expected drift velocity at this field strength. As the main purpose of the VdC is the monitoring of variances in the drift velocity, the statistical error is very important. For this measurement (see details in Appendix B), it is smaler than 0.01%.

When operating at CMS, the measuring time will be much shorter, but the desired accuracy of $\Delta v_d/v_d = 0.1\%$ can be reached already after a measuring time of roughly 3 min (see Appendix B).

Chapter 9

Conclusions

The direct monitoring of the drift velocity in the CMS barrel muon system with a dedicated drift chamber is necessary, since it is the only way to determine the effect of all gas impurities, even without detailed knowledge about the kind of impurities.

The drift velocity monitor chamber (VdC) for CMS was developed and a prototype was built in 2005. Starting from a similar chamber for the L3-experiment, the properties are optimised with systematic studies for the needs of the CMS barrel muon system. One of the main tasks is the improvement of the electric field homogeneity to $\Delta E/E \approx 0.1\%$ in the sensitive region.

The first measurements with the chamber are very promising: in a long time ($\approx 10\,\mathrm{h}$) run, the statistical error on the drift velocity is found to be below 0.01% which is an order of magnitude better than needed. The desired resolution can be reached in a measuring time in the order of a few minutes.

The measured absolute value of the drift velocity is $v_d = 55.6\,\mu\mathrm{m/ns}$ at $1.85\,\mathrm{kV/cm}$ which lies in the expected range.

However, for a better understanding of the absolute value, all sources of systematic errors have to be analysed more precisely.

The work on the chamber will be continued at the institute. The next steps will be the better understanding of some effects like the afterpulses or the trigger rates. The intention is to deliver a fully operating system of 6 VdCs to CMS when the experiment starts running in summer 2007.

Appendix A

Garfield Programs

The Garfield programs for simulating the electric field of the VdC are subdivided in three sections. Apart from those sections, there are several other sections possible in a Garfield simulation e.g. for setting a magnetic field, defining the gas or calculating drift properties. The sections used for the simulation of the VdC are:

- The MAIN-Section:

  In the MAIN-section, global variables are defined. The overall chamber dimensions are calculated later, so that it is possible to modify a chamber parameter by just changing its value in this section.

- The CELL-Section:

  In this section the chamber geometry is generated. The definition of the wires begins with the command "rows" and ends with a free line. Every line is subdivided in 6 positions. The first one defines a label for the wire. In the second one, the number of wires created in this line is specified. If the number is larger than 1, the line will be handled as a loop with the loop variable i. The next position gives the diameter of the wire. Positions 4 and 5 define x- and y-coordinate of the wire's centre. In the last position, the wire potential can be defined. A Garfield line that is too long can be ended with an ellipsis and continued in the next editor line.

- The FIELD-Section:

  The FIELD-section is used to define the plot parameters (surface or graph, electric field, potential, x component of the field, ...)

Table A.1 gives an overview over the variables used in the programs.

A.1 Simulation for the Prototype

In the first simulation, the field shaping electrodes are defined each as one wire, which does not lead to the correct electric field (see chapter 6.2.4). One line in the cell definition generates an entire layer of electrodes. The last two rows near the cathode are generated separately (wire labels b, u, d and e) for being able to change their resistor values ($r1$ and $r2$) for the simulation.

Variable name	In Fig. 6.1	Description
breite	l_y	width of the VdC in y-direction
kath_y	–	width of cathode in y-direction
r_anodkam	r_a	diameter of detection volume
abstx	s_x	field electrode spacing in x-direction
absty	s_y	field electrode spacing in y-direction
abst1	s_1	distance of first row of field electrodes (centre) to wall
breitedrft	b	distance of middle layers of field electrodes (centre to centre)
spalt	c	width of slit between drift volume and detection volume
d_anode	–	diameter of anode wire
dfeldform	–	diameter of field shaping electrodes
abstkatwnd	l_c	distance of the cathode to the wall
anzebenen	–	number of rows of field shaping wires
kath_x	–	width of cathode in x-direction
abstkath	s_2	distance of last row of electrodes (centre) to cathode
laenge_x	l_x	overall length of the drift volume in x-direction
trennwand	–	thickness of wall between drift volume and detection volume
wand	–	diameter of wires for simulation of the walls
drahtabst	–	distance of two wires for simulation of the walls (centre to centre)
uanode	–	potential of anode wire
ukathode	–	potential of cathode
rn, r1, r2	–	values o the resistors
rges	–	absolute resistivity of the resistor chain

Table A.1: Variables used in the programs.

```
************************************************************
*** Garfield-program for simulation of the VdC          ***
*** 2005 by Georg Altenhoefer                           ***
************************************************************
*** measures in [cm];   voltages in [V]                 ***
************************************************************
*** simulation for the prototype                        ***
*** 11/05: improved version (vdc4.0)                    ***
************************************************************

***********************************
&MAIN
***********************************
*** Measures ***
global breite=7.2
global kath_y=3.2
global wand=0.01
```

```
global r_anodkam=0.5
global abstx=0.6
global absty=0.6
global abst1=0.583
global breitedrft=1.6
global spalt=0.25
global d_anode=0.005
global d_feldform=0.2
global abstkatwnd=0.5
global anzebenen=10
global kath_x=0.5
global sdriftgr=6.3
global sdriftkl=2.1
global abstkath=0.596
global laenge_x={abst1}+({anzebenen}-1)*{abstx}+{abstkath}+{kath_x}+{abstkatwnd}
global trennwand=0.1
global drahtabst={wand}+0.00001

*** Strom ***
global uanode=1800
global ukathode=-11000
global rn=2000000
global r1=2000000
global r2=2000000
global rges=r1+r2+({anzebenen}-1)*rn

*** Draht-Anzahlen ***
global anztrennla=entier(({breite}/2-spalt/2-trennwand/2-sqrt({((trennwand/2+...
drahtabst/2)^2-((trennwand-wand)/2)^2)}))/{drahtabst})
global anzkathode=entier({kath_y/2}/{drahtabst})
global anzanodkam=entier(2*r_anodkam/{drahtabst})
global anzkathbr=entier({kath_x}/{drahtabst})

************************************
&CELL
************************************

  OPTIONS ISOMETRIC
  OPTIONS LAYOUT
  CELL-IDENTIFIER "abstkath:{abstkath}cm"

  plane y={breite/2}, V=0
  plane y=-{breite/2}, V=0
  plane x={r_anodkam+trennwand+laenge_x}, V=0
  plane x=-{r_anodkam}, V=0
  rows
  **** Anodendraht ****
  a 1 {d_anode} 0 0 {uanode}
  **** Feldformumgsdraehte ****
  b 3 {d_feldform} {r_anodkam}+{trennwand}+{abst1}+({anzebenen}-1)*{abstx} ...
    {breitedrft}/2+i*{absty} {ukathode}-{r1}*{ukathode}/{rges}
  u 3 {d_feldform} {r_anodkam}+{trennwand}+{abst1}+({anzebenen}-1)*{abstx} ...
    -{breitedrft}/2-i*{absty} {ukathode}-{r1}*{ukathode}/{rges}
  d 3 {d_feldform} {r_anodkam}+{trennwand}+{abst1}+({anzebenen}-2)*{abstx} ...
    {breitedrft}/2+i*{absty} ...
```

```
    {ukathode}-{r1}*{ukathode}/{rges}-{r2}*{ukathode}/{rges}
  e 3 {d_feldform} {r_anodkam}+{trennwand}+{abst1}+({anzebenen}-2)*{abstx} ...
   -{breitedrft}/2-i*{absty} ...
    {ukathode}-{r1}*{ukathode}/{rges}-{r2}*{ukathode}/{rges}
  f {anzebenen}-2 {d_feldform} {r_anodkam}+{trennwand}+{abst1}+i*{abstx} ...
    {breitedrft}/2+2*{absty} (i+1)*{rn}*{ukathode}/{rges}
  g {anzebenen}-2 {d_feldform} {r_anodkam}+{trennwand}+{abst1}+i*{abstx} ...
    {breitedrft}/2+{absty} (i+1)*{rn}*{ukathode}/{rges}
  h {anzebenen}-2 {d_feldform} {r_anodkam}+{trennwand}+{abst1}+i*{abstx} ...
    {breitedrft}/2 (i+1)*{rn}*{ukathode}/{rges}
  j {anzebenen}-2 {d_feldform} {r_anodkam}+{trennwand}+{abst1}+i*{abstx} ...
    -{breitedrft}/2 (i+1)*{rn}*{ukathode}/{rges}
  k {anzebenen}-2 {d_feldform} {r_anodkam}+{trennwand}+{abst1}+i*{abstx} ...
    -{breitedrft}/2-{absty} (i+1)*{rn}*{ukathode}/{rges}
  l {anzebenen}-2 {d_feldform} {r_anodkam}+{trennwand}+{abst1}+i*{abstx} ...
    -{breitedrft}/2-2*{absty} (i+1)*{rn}*{ukathode}/{rges}
  **** Trennwand ****
  m entier({anztrennla/4}) {wand} {r_anodkam}+{wand}/2 ...
   {spalt}/2+{trennwand/2}+sqrt({{((trennwand/2+drahtabst/2)^2-...
((trennwand-wand)/2)^2)})+i*{drahtabst} 0
  m {anztrennla} {wand} {r_anodkam}+{trennwand}-{wand}/2...
    {spalt}/2+{trennwand/2}+sqrt({{((trennwand/2+drahtabst/2)^2-...
((trennwand-wand)/2)^2)})+i*{drahtabst} 0
  m 1 {trennwand} {r_anodkam+trennwand/2} {spalt/2+trennwand/2} 0
  n entier({anztrennla/4}) {wand} {r_anodkam}+{wand}/2 ...
-({spalt}/2+{trennwand/2}+sqrt({{((trennwand/2+drahtabst/2)^2-...
((trennwand-wand)/2)^2)})+i*{drahtabst}) 0
  n {anztrennla} {wand} {r_anodkam}+{trennwand}-{wand}/2...
     -({spalt}/2+{trennwand/2}+sqrt({{((trennwand/2+drahtabst/2)^2-...
((trennwand-wand)/2)^2)})+i*{drahtabst}) 0
  n 1 {trennwand} {r_anodkam+trennwand/2} -{spalt/2+trennwand/2} 0
  o {anzkathode} {wand}...
    {r_anodkam}+{trennwand}+{abst1}+({anzebenen}-1)*{abstx}+{abstkath}+{wand/2}...
    {wand/2}+i*{drahtabst} {ukathode}
  **** Kathode ****
  t {anzkathode} {wand}...
    {r_anodkam}+{trennwand}+{abst1}+({anzebenen}-1)*{abstx}+{abstkath}+{wand/2}...
    -{wand/2}-i*{drahtabst} {ukathode}
  v {anzkathode} {wand}...
    {r_anodkam}+{trennwand}+{abst1}+...
({anzebenen}-1)*{abstx}+{abstkath}+{kath_x}-{wand/2}...
    {wand/2}+i*{drahtabst} {ukathode}
  w {anzkathode} {wand}...
    {r_anodkam}+{trennwand}+{abst1}+...
({anzebenen}-1)*{abstx}+{abstkath}+{kath_x}-{wand/2}...
     -{wand/2}-i*{drahtabst} {ukathode}
  x 1 {kath_x-2*wand-0.00001} ...
    {r_anodkam}+{trennwand}+{abst1}+({anzebenen}-1)*{abstx}+{abstkath}+{kath_x/2}...
    {kath_y/2} {ukathode}
  y 1 {kath_x-2*wand-0.00001} ...
    {r_anodkam}+{trennwand}+{abst1}+({anzebenen}-1)*{abstx}+{abstkath}+{kath_x/2}...
    -{kath_y/2} {ukathode}
  **** Anodenkammer ****
  q {anzanodkam} {wand} {r_anodkam}+{wand}/2-(i+1)*{drahtabst} ...
    {r_anodkam}+{wand}/2 0
```

```
  r {anzanodkam} {wand} {r_anodkam}+{wand}/2-(i+1)*{drahtabst} ...
    -{r_anodkam}-{wand}/2 0

************************************
&FIELD
************************************
  track 1.6 0 6.8 0
  plot-field graph ex

&STOP
```

A.2 Improved Simulation

For the improved Garfield simulation, the field shaping electrodes are individually represented by multiple wires forming a circle with the diameter of the field shaping electrodes. For that, some additional variables had to be defined: The diameter of the small wires m_ring, their distance abs_m_ring, their number n_ring and the diameter of the circle d_ring, because the radius of the wires must be taken into account. For reasons of symmetry, the number of the small wires is always a multiple of 4.

Below, the generation of the circles is shown for four of the field shaping electrodes. Every row generates one field electrode. The other field electrodes and circular structures like the cathode edges or the shape of the slit between drift volume and detection volume are generated similarly.

```
[...]
** dicke des ringmantels **
global m_ring=0.01
global d_ring={d_feldform}-{m_ring}
global abs_m_ring={m_ring}+0.01
** n_ring: anzahl der einzeldraehte: durch 4 teilbare ganze zahl (wg. symmetrie): **
global n_ring=4*entier(Pi*{d_ring}/{abs_m_ring}/4)
[...]
************************************
&CELL
************************************
[...]
rows
[...]
  f {n_ring} {m_ring}...
      {r_anodkam}+{trennwand}+{abst1}+0*{abstx}+{d_ring/2}*cos(2*Pi*i/{n_ring}) ...
      {breitedrft}/2+2*{absty}+{d_ring/2}*sin(2*Pi*i/{n_ring})...
      (0+1)*{rn}*{ukathode}/{rges}
  f {n_ring} {m_ring}...
      {r_anodkam}+{trennwand}+{abst1}+1*{abstx}+{d_ring/2}*cos(2*Pi*i/{n_ring}) ...
      {breitedrft}/2+2*{absty}+{d_ring/2}*sin(2*Pi*i/{n_ring})...
      (1+1)*{rn}*{ukathode}/{rges}
  f {n_ring} {m_ring}...
      {r_anodkam}+{trennwand}+{abst1}+2*{abstx}+{d_ring/2}*cos(2*Pi*i/{n_ring}) ...
      {breitedrft}/2+2*{absty}+{d_ring/2}*sin(2*Pi*i/{n_ring})...
```

```
      (2+1)*{rn}*{ukathode}/{rges}
  f {n_ring} {m_ring}...
      {r_anodkam}+{trennwand}+{abst1}+3*{abstx}+{d_ring/2}*cos(2*Pi*i/{n_ring}) ...
      {breitedrft}/2+2*{absty}+{d_ring/2}*sin(2*Pi*i/{n_ring})...
      (3+1)*{rn}*{ukathode}/{rges}
[...]
```

Appendix B

Calculation of the Statistical Error in the Measured Drift Velocity

B.1 Statistical Error of the First Measurement

n	t_n	$\sigma(t_n)$	N
1	315.08 ns	21.26 ns	400 329
2	1070.38 ns	21.82 ns	215 792

Table B.1: *Parameters of the Gaussian Fit to the peaks of Fig. 8.6.*

The data was analysed with Root [45]. From the Gaussian fit to the two peaks, one obtains the mean values t_1 and t_2 and the root mean square (RMS) $\sigma(t_1)$ and $\sigma(t_2)$. The error of the mean is calculated as follows:

$$\sigma(\bar{t}_n) = \frac{\sigma(t_n)}{\sqrt{N_n}}, \tag{B.1}$$

where N_n is the number of events in peak n. For the two peaks in figure 8.6, one obtains:

$$\sigma(\bar{t}_1) = \frac{21.64\,\text{ns}}{\sqrt{400\,329}} = 0.0336\,\text{ns} \tag{B.2}$$

$$\sigma(\bar{t}_2) = \frac{21.89\,\text{ns}}{\sqrt{215\,792}} = 0.0470\,\text{ns} \tag{B.3}$$

The drift time between both peaks is:

$$\Delta t = t_2 - t_1 = 755.30\,\text{ns} \tag{B.4}$$

$$\sigma(\Delta t) = \sqrt{\sigma^2(\bar{t}_2) + \sigma^2(\bar{t}_1)} = 0.06\,\text{ns} \tag{B.5}$$

And finally the drift velocity, with the drift distance $\Delta x = 4.2\,\text{cm}$:

$$v_d = \frac{\Delta x}{\Delta t} = 55.607\,\frac{\mu\text{m}}{\text{ns}} \tag{B.6}$$

$$\sigma(v_d) = \sigma\left(\frac{\Delta x}{\Delta t}\right) = \Delta x \cdot \sigma\left(\frac{1}{\Delta t}\right) = \frac{\Delta x}{(\Delta t)^2} \cdot \sigma(\Delta t) = 0.004\,\frac{\mu\text{m}}{ns} \tag{B.7}$$

This is the **statistical error** that is relevant for the detection of fluctuations in the drift velocity. For determining the **absolute error**, the systematic errors like the error of Δx or runtime differences of the signals must be taken into account.

B.2 Estimate on the Needed Measuring Time at CMS

An important question is, how long the VdC has to take data reach a resolution of $\sigma(v_d)/v_d = 0.1\,\%$. This value is mainly dependent on the number of events in the two peaks. Assuming an identical pulse width $\sigma(t_n) = \sigma(t_1) = \sigma(t_2)$ and identical numbers of entries $N = N_1 = N_2$ for both peaks, one obtains with equation (B.1) the same standard deviations of the mean $\sigma(\bar{t}_n) = \sigma(\bar{t}_1) = \sigma(\bar{t}_2)$ an thus:

$$\sigma(v_d) = \frac{\Delta x}{(\Delta t)^2} \cdot \sigma(\Delta t) \tag{B.8}$$

$$= \frac{\Delta x}{(\Delta t)^2} \sqrt{2(\sigma(\bar{t}))^2} \tag{B.9}$$

$$= \frac{\Delta x}{(\Delta t)^2} \cdot 2 \cdot \frac{\sigma(t)}{\sqrt{N}} \tag{B.10}$$

$$\Rightarrow \quad N = \frac{(\Delta x)^2}{(\Delta t)^4} \cdot 2 \cdot \left(\frac{\sigma(t))}{\sigma(v_d)} \right)^2 \tag{B.11}$$

Assuming for $\sigma(t)$ - that is given mainly by the width of the ionising β^- beams and is thus roughly constant - a value of 22 ns and for the other quantities calculated above, one obtains for the desired resultion $\sigma(v_d)/v_d = 0.1\,\%$:

$$N \approx 1670 \tag{B.12}$$

Thus, $N = 1670$ entries are needed in each of the two peaks which is $N_{ges} = 3340$ in total. With a signal rate of 20 Hz (as measured during the first tests of the VdC), this leads to a minimum measuring time of:

$$t_{meas} = \frac{3340}{20\,\mathrm{Hz}} = 167\,\mathrm{s} \approx 3\,\mathrm{min} \tag{B.13}$$

This value is only a rough benchmark, as one does not want to measure at the lower limit and on the other hand a higher signal rate will hopefully be reached with better scintillators. However, this value shows that the desired accuracy can be obtained in a reasonable time.

Appendix C

Proposal for a VdC Gas System at CMS

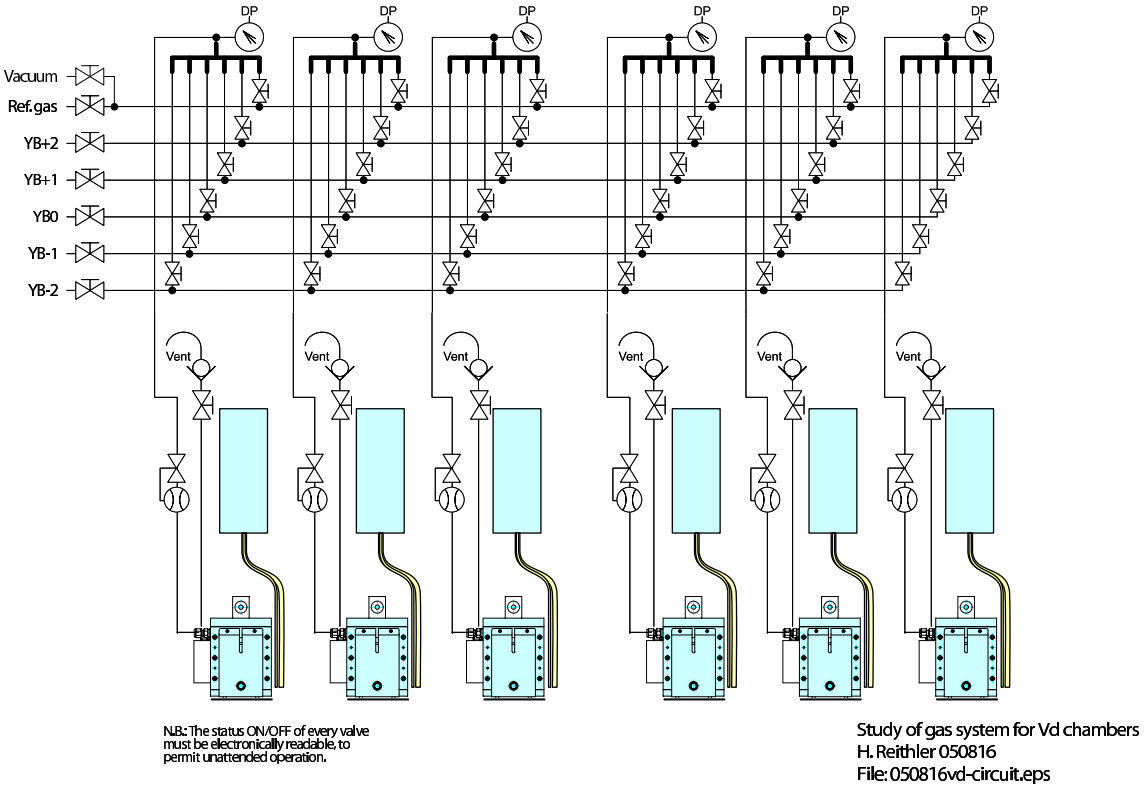

Figure C.1: *Planned gas system for the VdC*

For CMS, 6 VdCs will operate simultaneously: one for each wheel plus one spare chamber. The gas system shown in figure C.1 is designed in a way that it is possible to let the gas flow from every wheel flow through every VdC, so that the results of the chambers can be cross-checked. The status of the valves is planned to be read out electronically to be able to check it remotely at any time, as needed for a continuous and unattended operation.

Bibliography

[1] T. Hebbeker. Lecture "Elementarteilchenphysik I", RWTH Aachen, 2004.

[2] The Particle Data Group. Review of Particle Physics. *Physics Letters B*, 592:1+, 2004.

[3] ETH Institute for Particle Physics, 2005. htp://www.ipp.phys.ethz.ch.

[4] The Super-Kamiokande Collaboration: Y. Ashie. Evidence for an Oscillatory Signature in Atmospheric Neutrino Oscillation. *Physical Review Letters*, 93:101801, 2004.

[5] H. Weyl. Eine neue Erweiterung der Relativitätstheorie. *Ann. Phys.*, 59:101, 1919.

[6] ALEPH, DELPHI, L3 and OPAL Collaborations, The LEP Working Group for Higgs Boson Searches. Search for the Standard Model Higgs Boson at LEP. *Physics Letters B*, 565:61–75, 2003.

[7] CMS Collaboration. *The Tracker System Project - Technical Design Report.* CERN/LHCC 94-38, December 1994.

[8] CMS pixel detector. http://cms.web.psi.ch/cms.html.

[9] CMS Collaboration. *Addendum to the CMS Tracker TDR.* CERN/LHCC 2000-016, February 2000.

[10] http://cmsinfo.cern.ch/Welcome.html/CMSdetectorInfo/CMSecal.html. 2005.

[11] CMS Collaboration. *The Electromagnetic Calorimeter Project - Technical Design Report.* CERN/LHCC 97-33, December 1997.

[12] http://cmsinfo.cern.ch/Welcome.html/CMSdetectorInfo/CMShcal.html. 2005.

[13] CMS Collaboration. *The Hadron Calorimeter Project - Technical Design Report.* CERN/LHCC 97-31, June 1997.

[14] I.Belotev and N. Neumeister. Performance of the CMS offline reconstruction software. *CMS AN 2005/010*, 2005.

[15] S.H. Ahn et al. *Nucl. Instr. and Meth. A*, 469:323, 2001.

[16] CMS Collaboration. *The Level-1 Trigger - Technical Design Report*, volume I. CERN/LHCC 2000-038, December 2000.

[17] CMS Collaboration. *The Trigger and Data Acquisition Project - Technical Design Report*, volume II. CERN/LHCC 2002-026, December 2002.

[18] R.S. Gilmore. *Single Particle Detection and Measurement.* Taylor & Francis, London - Washington DC, 1992.

[19] W. Greiner, L. Neise, and H. Stöcker. *Theoretische Physik - Band 9 - Thermodynamik und statistische Mechanik.* Verlag Harri Deutsch, 1987.

[20] W. Blum and L. Rolandi. *Particle Detection with Drift Chambers.* Springer Verlag, 1994.

[21] F. Sauli. *Principles of Operation of Multiwire Proportional and Drift Chambers.* CERN 77-09, 1977.

[22] Richard C. Fernow. *Introduction to Experimental Particle Physics.* Cambridge University Press, 1986.

[23] V. Palladino and B.Sadoulet. Application of classical theory of electrons in gases to drift proportional chambers. *NIM*, 128:323–335, 1975.

[24] G. Schultz and J. Gresser. A Study of Transport Coefficients of Electrons in Some Gases in Proportional and Drift Chambers. *NIM*, 151:413–431, 1978.

[25] CMS Collaboration. *The Muon Project - Technical Design Report.* CERN/LHCC 97-32, December 1997.

[26] Hubert Schwarthoff. *Simulationen in Konzeption und Bau der zentralen Myondriftkammern am CMS-Detektor.* PhD thesis, III. Phys. Inst. A, RWTH Aachen, June 1997.

[27] Hans Reithler, 2005. III. Physikalisches Institut A, RWTH Aachen, private communications.

[28] Manfred Sassowsky. Überwachung von Driftkammergasen mit einer Testkammer, September 1990. Diploma Thesis, III. Phys. Inst. A, RWTH Aachen.

[29] Andrea Tavenrath. Bau einer Driftkammer zur Überwachung der Gasqualität in der L3-Vertexkammer, April 1989. Diploma Thesis, III. Phys. Inst. A, RWTH Aachen.

[30] W.R. Leo. *Techniques for Nuclear and Particle Physics Experiments.* Springer Verlag, 1994.

[31] R. Veenhof. Garfield, recent developments. *Nucl. Instr. and Meth. A*, 419:726–730, 1998. http://consult.cern.ch/writeup/garfield/.

[32] Maxwell3d. http://www.ansoft.com/products/em/max3d/.

[33] Opera-3d tosca. http://www.vectorfields.co.uk/.

[34] Quickfield. http://www.quickfield.com/.

[35] Comsol multiphysics. http://www.comsol.com.

[36] S.F. Biagi. Accurate solution of the boltzmann transport equation. *Nucl. Instr. and Meth. A*, 273:533, 1988. http://consult.cern.ch/writeup/magboltz/.

[37] I.B. Smirnov. Modeling of Ionization Produced by Fast Charged Particles in Gases. *Nucl. Instr. and Meth. A*, 554:474, 2005. http://consult.cern.ch/writeup/heed/.

[38] Rob Veenhof, 2005. private communications.

[39] Barthel Philipps, 2005. III. Physikalisches Institut A, RWTH Aachen, private communications.

[40] W. Nolting. *Grundkurs: Theoretische Physik 4. Spezielle Relativitätstheorie/Thermodynamik.* Verlag Zimmermann-Neufang, 1993.

[41] Günter Hilgers, 2006. III. Physikalisches Institut A, RWTH Aachen, private communications.

[42] *Benutzerhandbuch - Tektronix - Digitalisierungsoszilloskope TDS 500B, 600B und TDS 700A*, 1996. http://www.tektronix.com.

[43] *Technical Information Manual - MOD. V767*, 2003. http://www.caen.it.

[44] G. Zilisi and A. Kapusi, 2006. private communications.

[45] R. Brun and F. Rademakers. Root - An object oriented data analysis framework. *Nucl. Instr. and Meth. A*, 389:81–86, 1997.

List of Figures

List of Tables

Acknowledgements

First I want to thank the two persons who will still have to work on this thesis when I have finished:

Prof. Dr. T. Hebbeker, for making it possible for me to work on this interesting topic and to be part of the huge CMS collaboration with members from all over the world.and Prof. Dr. M. Erdmann for agreeing to be my second referee.

Then I want to thank Dr. Hans Reithler for being a brilliant supervisor, trying to teach me as much as possible about driftchambers and answering my questions very precisely even late in the afternoon.

Special thanks goes to the colleagues from the electronical and mechanical workshop: Günter Hilgers, Josef Grooten, Barthel Philipps, Franz Adamczyk and Henry Szczesny for trying to make everything I asked them for possible. Without them I would now have only my simulations and no drift chamber.

Another great help came from Debrecen, from Gyula Zilisi and Anita Kapusi who are writing the software for the measurements with the chamber. Without them, I would have simulations and a beautiful drift chamber but no data.

I'm very gratefull to Michael Bontenackels and Carsen Hof for proofreading every single word again and again and for all the helpful discussions on my thesis especially in the last 24 hours! Without you, I might have had simulations, a drift chamber, data,..... but no thesis.....

Not to forget the other proofreaders Kerstin Hoepfner, Prof. Hebbeker and Hans Reithler.

Furthermore I'd like to thank the colleagues from my office, Michael Sowa, Emanuel Jacobi, Pim Ruetten and all the others for the great time I have had during the last year.

A very special thanks goes to my parents, that supported me in every possible way!!!

And last, I want to say THANK YOU to the most important person of my life: Thank you, Fritzi, that you stayed with me all the time. I know that the last weeks were very hard for you, but you allways tried to understand me.